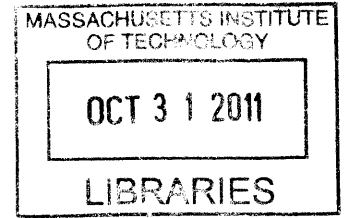# Strongly Coupled Plasmas and the QCD Critical Point

by

Christiana Athanasiou

Submitted to the Department of Physics
in partial fulfillment of the requirements for the degree of

Doctor of Philosophy in Physics

at the

MASSACHUSETTS INSTITUTE OF TECHNOLOGY

June 2011

Author . . . .
Department of Physics
May 20, 2011

Certified by . . . .
Krishna Rajagopal
Professor
Thesis Supervisor

Certified by . . . .
Hong Liu
Professor
Thesis Supervisor

Accepted by . . . .
Krishna Rajagopal
Associate Department Head for Education

Strongly Coupled Plasmas and the QCD Critical Point

by

Christiana Athanasiou

Submitted to the Department of Physics
on May 20, 2011, in partial fulfillment of the
requirements for the degree of
Doctor of Philosophy in Physics

Abstract

In this thesis, we begin by studying selected fluctuation observables in order to locate the QCD critical point in heavy-ion collision experiments. In particular, we look at the non-monotonic behavior as a function of the collision energy of higher, non-Gaussian, moments of the event-by-event distributions of pion, proton and net proton multiplicities, as well as estimates of various measures of pion-proton correlations. We show how to use parameter independent ratios among these fluctuation observables to discover the critical point, if it is located in an experimentally accessible region.

We then begin our investigation of the properties of quarks and baryons which live in the strongly coupled plasma of certain gauge theories which are similar to QCD using the AdS/CFT correspondence. We first study the velocity dependence of the screening length, L_s, of N_c quarks arranged in a circle (a "baryon") immersed in the hot plasma of strongly coupled $\mathcal{N} = 4$ super Yang-Mills theory moving with velocity v. We find that in the $v \to 1$ limit, $L_s \propto (1 - v^2)^{1/4}/T$, which provides evidence for the robustness of the analogous behavior of the screening length defined by the static quark-antiquark pair.

Finally, we compute the energy density and angular distribution of the power radiated by a quark undergoing circular motion in the vacuum of any conformal field theory that has a dual classical gravity description and many colors. In both the strong and weak coupling regimes, the angular distribution of the radiated power is in fact similar to that of synchrotron radiation produced by an electron in circular motion in classical electrodynamics: the quark emits radiation in a narrow beam along its velocity vector with a characteristic opening angle $\alpha \sim 1/\gamma$. This jet-like beam of gluons opens a new way of modeling jet quenching in heavy-ion collisions.

Thesis Supervisor: Krishna Rajagopal
Title: Professor

Thesis Supervisor: Hong Liu
Title: Professor

Dedication

To my parents, Mary and Andreas, for their unconditional love and support.

Acknowledgments

parents, Andreas and Mary. I do not know how to thank them enough for helping me be who I am and for supporting me at every step of my life. I would not have gone far without their encouragement and unconditional love.

Contents

List of Figures

13

14

List of Tables

Chapter 1

Introduction

In this Chapter we will present an introduction to the Quantum Chromodynamics (QCD) phases of matter that current heavy-ion collision experiments are exploring, namely the hadron gas and the quark-gluon plasma (QGP). We will discuss the phase transition between the two phases and the existence of a second-order critical point - the QCD critical point. We will then discuss the experimental evidence for the QGP production and a probe used to learn more about its properties. We will introduce the gauge/gravity duality as a tool to help us understand the properties of strongly interacting theories, such as QCD.

1.1 QCD and Heavy-Ion Phenomenology

QCD, the theory of strong interactions, is a very remarkable theory. It becomes weakly coupled at high energies (asymptotic freedom), which allows us to write down the Lagrangian of QCD in terms of its perturbative degrees of freedom, the quarks and gluons. This fundamental definition is very simple, yet QCD describes a very broad range of phenomena such as jet quenching and color superconductivity, while its phase diagram (when you turn on finite temperature and baryon chemical potential) is not fully understood. The main reason is that QCD is strongly coupled at low energies which results in quarks and gluons becoming confined within hadrons, like protons and neutrons. Some regions of the phase diagram can be explored experimentally
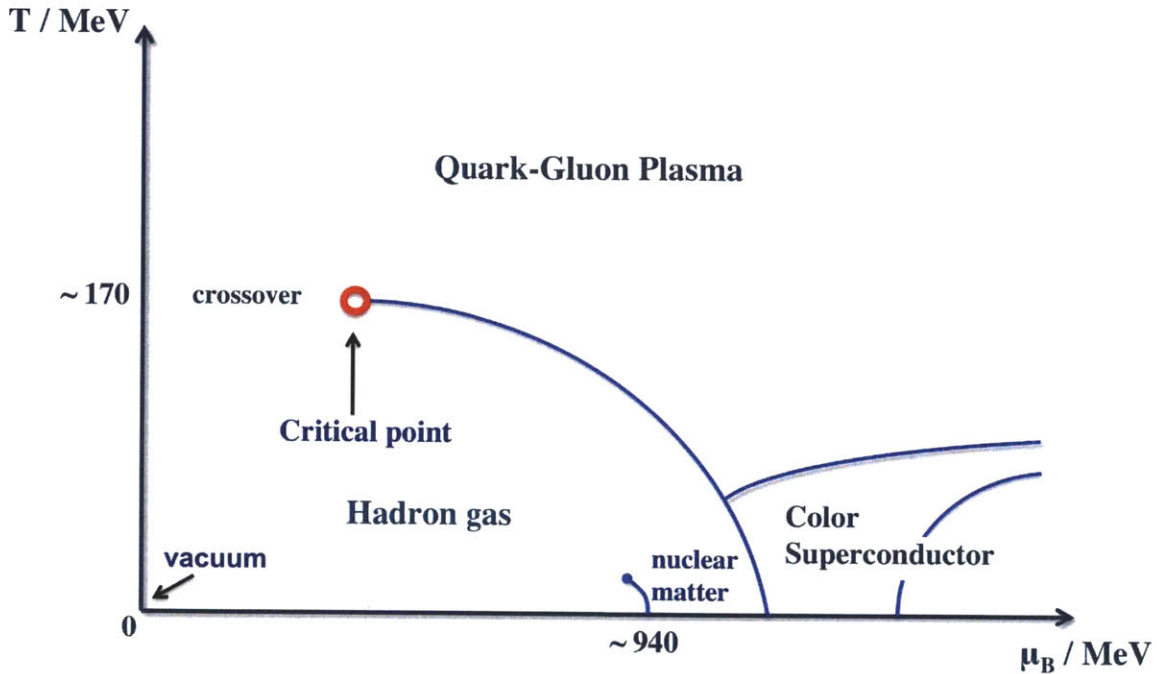
Figure 1-1: A sketch of the QCD phase diagram. See text for discussion.

using heavy-ion collision experiments and the study of the interior of neutron stars. In this thesis we will focus on understanding aspects of the phase diagram region where the baryon chemical potential is not too high, namely the quark-gluon plasma and its phase transition to a hadron gas. But first, what is the QCD phase diagram and what do we know about it?

1.1.1 QCD Phase Diagram

Figure 1-1 shows a sketch of the QCD phase diagram. The horizontal axis is the baryon number chemical potential, μ_B, and the vertical axis is the temperature of the system, T. In the regime of small temperatures and high densities quarks form Cooper pairs and condense. This results in the formation of superconducting phases [1, 2, 3, 4, 5, 6] which may arise in the core of neutron stars.

At small temperatures and low densities, QCD is in the hadron gas state, which is what we see around us. In this state, chiral symmetry is broken and quarks and gluons are confined within hadrons. As you increase the temperature, there is a phase transition where quarks become deconfined and exist in a strongly coupled soup - the

strongly coupled quark-gluon plasma (sQGP). As you increase the temperature even further, the QGP becomes weakly coupled where the quarks and gluons move almost freely in the plasma. Heavy-ion collisions at the Relativistic Heavy Ion Collider (RHIC) [7, 8, 9, 10] produced this strongly coupled QGP at the early stages of the collisions (roughly 1 fm, [11], see Section 1.1.3 for more details). Theoretical studies of the properties of this matter are very difficult due to the strong interactions involved. Chapters 3 and 4 will focus on selected properties of moving matter in strongly coupled plasmas of theories similar to QCD, using a tool called the gauge/gravity duality, which will be introduced in Section 1.2.

At zero densities, finite T lattice calculations indicate that the phase transition between the hadron gas and sQGP phase is a smooth crossover [12] at temperature of around 170 MeV, whereas model approaches indicate that for zero temperatures, the μ_B-driven transition is first order [13]. This means that the first order line ends before reaching the $\mu_B = 0$ axis, and the point where this first order line ends is called the QCD critical point. Its location is not known theoretically even within a factor of two on the μ_B axis. The use of lattice calculations to locate the critical point is limited due to the notorious sign problem which arises for non-zero μ_B. Reviews on the lattice limitations and model approaches on the location of the critical point can be found in References [14, 15, 16, 17, 18, 19, 20, 21, 22]. Therefore, our best bet is to locate it experimentally, using heavy-ion collision experiments. So far, data has been published from the STAR collaboration on net proton cumulants [23] in high energy RHIC collisions which exclude the critical point for $\mu_B < 200$ MeV. Subsequent RHIC runs at lower energies will explore the phase diagram up to $\mu_B \approx 420$ MeV, which will shed more light on where the critical point is or is not. Chapter 2 is dedicated to describing how to experimentally locate the critical point using fluctuation observables, if it is located in an experimentally accessible region, together with a more detailed discussion of the STAR results.

1.1.2 Heavy-Ion Collision Experiments

In heavy-ion collision experiments, heavy nuclei, such as gold at RHIC and lead at the Super Proton Synchrotron (SPS) and at the Large Hadron Collider (LHC), are collided at very high center-of-mass energies $\sqrt{s}$. At RHIC, the maximum $\sqrt{s}$ per nucleon reached is 200 GeV and at the LHC the maximum $\sqrt{s}$ per nucleon reached will be 5.5 TeV. The reason that high collision energies are necessary is so that matter with high energy densities is created. In order to see this consider a simple argument: in the center-of-mass frame, the nuclei move at relativistic speeds and hence their spherical shape becomes Lorentz contracted into a "pancake" shape. The higher the collision energy is, the more squeezed the pancakes become and hence when the nuclei collide (for simplicity head-on), their energy is concentrated at a smaller volume, which results to a higher energy per unit volume (energy density). Colliding large nuclei is also useful in creating larger volumes of high energy density matter which makes it easier to study the properties of such strongly interacting matter in bulk.

By varying the center-of-mass energy $\sqrt{s}$ of the colliding nuclei, one can change the temperature and chemical potential of the produced matter at the initial stages after the collision, thus scanning the phase diagram. As you increase $\sqrt{s}$, the temperature of the produced matter increases but the baryon chemical potential decreases. The $\sqrt{s}$ dependence of T is intuitive but perhaps the dependence of μ_B on $\sqrt{s}$ is less clear so let us give a simple argument: for higher $\sqrt{s}$, more entropy is produced but the baryon number is conserved; the net baryon number per collision is always equal to the total number of baryons arising from the initial nuclei, namely $197 + 197$. Therefore, as we increase $\sqrt{s}$, these baryons are diluted among many more hadrons, making the baryon chemical potential smaller.

As we mentioned above, a strongly coupled QGP is produced at the early stages of the heavy-ion collisions. As this QGP expands and cools, it follows paths such that the ratio of the baryon number density to the entropy density, n_B/s, is constant. This arises because the baryon number is a conserved quantity and assuming the expansion
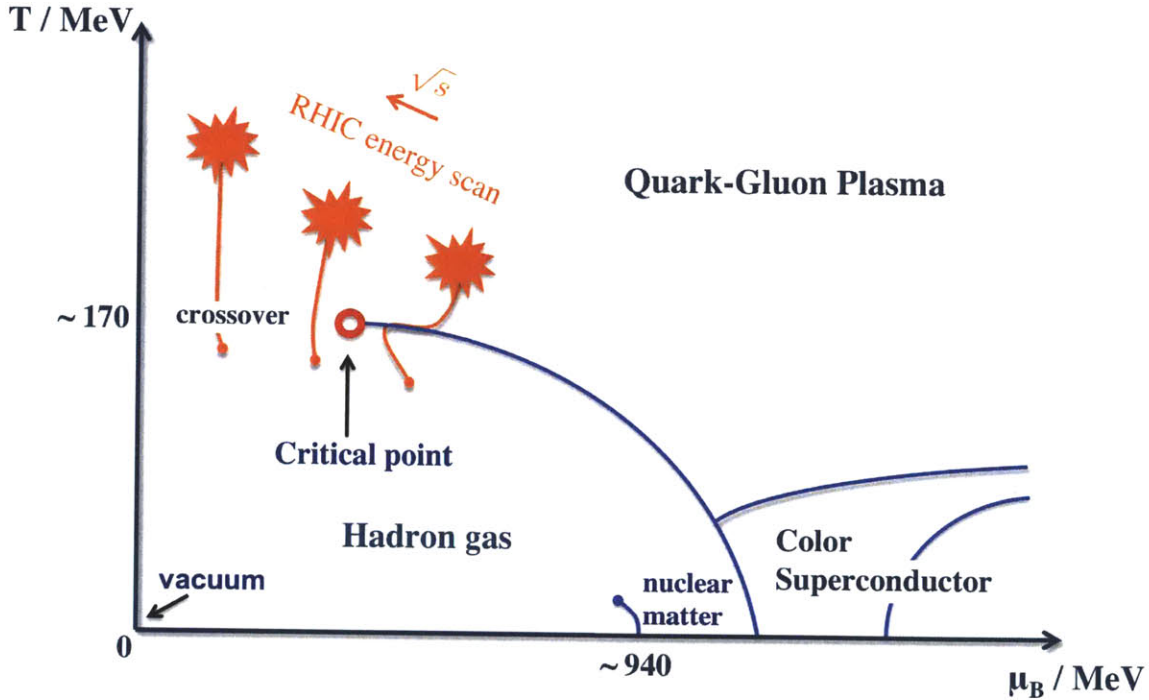
Figure 1-2: The orange lines indicate paths that matter after heavy-ion collisions follow with the ratio of baryon number density to entropy density, n_B/s constant. Different paths shown are for different center-of-mass energies $\sqrt{s}$.

happens adiabatically, the entropy is also conserved. Hence, the ratio of the densities is conserved. Such paths are sketched in Figure 1-2.[1] At some point the temperature of the system drops such that the system crosses the phase transition region and the QGP hadronizes. As the system expands even further, there is a point where the mean free path of the particles becomes equal to the system size and there are no more inelastic interactions. At that point, the particle numbers stop changing and we have chemical freeze-out. In Figure 1-2, the chemical freeze-out points are denoted by small circles. After that, the particles move towards the detector without changing into other particles, thus the detector 'sees' roughly the particle multiplicities from the chemical freeze-out conditions.

Experimentalists can measure the particle multiplicities of many hadron species, and the ratios among these multiplicities turn out to obey the distributions arising

---

[1]Note that there is a discontinuity in the trajectories when the system goes though the first order line. This occurs because as you move from the QGP phase to the hadron gas phase, there is a sudden drop in the number of degrees of freedom and hence in the entropy. Therefore, in order for the n_B/s ratio to remain constant, the temperature has to increase.

from fitting a grand canonical ensemble with temperature T and baryon number chemical potential μ_B. The temperature extracted from the fit is the chemical freeze-out temperature and for RHIC at its highest energies, this temperature is around 155-180 MeV [24, 25]. This means that the system is in thermal equilibrium near the freeze-out point. The $\sqrt{s}$ dependence of T and μ_B described above also translates to the freeze-out conditions. Empirical parametrization of the μ_B dependence of the freeze-out temperature has been obtained from heavy ion collision data. An example coming from [26] is:

$$T(\mu_B) = a - b\mu_B^2 - c\mu_B^4, \tag{1.1}$$

with $a = 0.166$ GeV, $b = 0.139$ GeV^{-1} and $c = 0.053$ GeV^{-3}, which will be used in Chapter 2.

As we mentioned above, the detector 'sees' the particle multiplicities from the chemical freeze-out point. Therefore, in order to see the effects of the critical point on observables, one should find observables that are sensitive to the proximity of the critical point and try to get the freeze-out point as close to the critical point as possible by varying the collision center of mass energy, $\sqrt{s}$.

The critical mode, the σ-field, is the order parameter of the phase transition between the hadron gas and the QGP. The relation between its mass, m_σ, and the correlation length, ξ, is given by:

$$m_\sigma \equiv \xi^{-1}. \tag{1.2}$$

At the critical point, the critical mode becomes massless (ξ diverges) and develops long-wavelength correlations. This is true only in the case of an infinite system that lives for an infinite amount of time. But the QGP created in heavy-ion collisions has a finite size and lives for only a short period of time, which limits ξ at the critical point to a maximum value of roughly $1.5 - 3$ fm [27, 28, 29], which is still long compared to the natural ~ 0.5 fm away from the critical point. It turns out that the finite time is a more stringent limitation on the growth of the correlation length [30, 27] than the system size finiteness. The critical mode couples to particles observed in the

detectors, for example pions and protons, in the following way:

$$\mathcal{L}_{\sigma\pi\pi,\sigma pp} = 2\,G\,\sigma\,\pi^+\pi^- + g_p\,\sigma\,\bar{p}\,p, \qquad (1.3)$$

where G is the coupling constant between the critical mode and pions and g_p is the coupling constant between the protons and the critical mode. Due to this type of interactions, the increase in the critical mode fluctuations near the critical point results in an increase in the fluctuations of particle multiplicities, transverse momentum distributions, etc. of particles that interact with the critical mode. As we change the center of mass energy of the collisions, if the freeze-out point approaches the critical point, we would see an increase in the fluctuations in the number of these particles. These fluctuations would then decrease as we move away from the critical point. (This is true for any observables which are sensitive to the proximity of the critical point to the point where freeze-out occurs.) Hence, a characteristic signature of the critical point is the non-monotonic behavior of such variables, as a function of $\sqrt{s}$ [31, 30]. Higher moments depend on higher powers of ξ and thus increase more near the critical point, hence making them more favorable in searching for the critical point [32]. This non-monotonic behavior of higher moments of pion, proton and net proton multiplicities near the critical point is the main signature that RHIC is currently searching for in order to locate the critical point. In Chapter 2, we present a detailed analysis of such higher moment observables and also show how to use nontrivial but parameter independent ratios among these more than a dozen fluctuation observables to discover the critical point.

1.1.3 Quark-Gluon Plasma Production

Experiments at RHIC have found that the resulting fireball of quarks and gluons seems to behave collectively like an almost perfect liquid - a liquid which is well described by hydrodynamics [33, 34, 35]. The conclusion of collective behavior comes from examining the asymmetry of a collision around the collision axis. Suppose the two nuclei do not collide centrally but collide with an impact parameter comparable
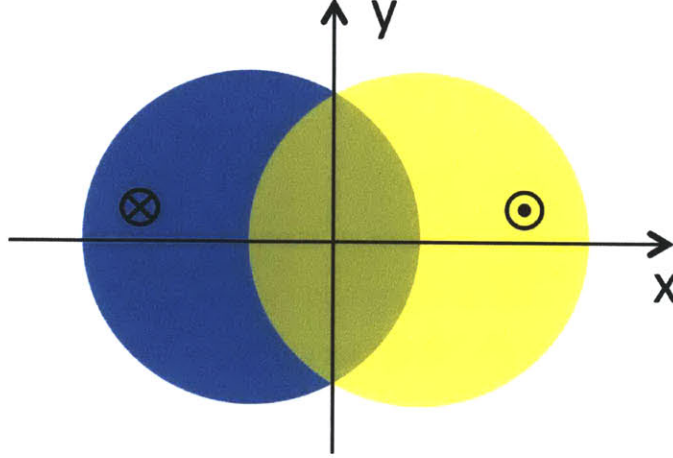
Figure 1-3: A sketch of the collision of two nuclei, moving in and out of the plane of the page. The collision region is limited to the green "almond-shaped" region in the middle and the nucleons outside that region (spectator nucleons) do not participate in the collision.

to the nuclear radius. Then, the two nuclei collide in an "almond-shaped" region as shown in Figure 1-3. If the resulting matter was weakly interacting like a free gas, then the momentum distribution of the particles observed would have been uniform around the almond shape. If, on the other hand, the matter produced is strongly interacting and has reached local equilibrium, thus producing some form of a fluid, then the pressure gradient along the short side of the almond (the x-axis in figure 1-3), is much larger than the pressure gradient along the long side, thus producing particles with higher transverse momenta in the direction of the short side of the almond. This is what has been observed at RHIC: hadrons move with summed transverse momenta that can be as much as twice as large in the short direction of the almond as they are in the long direction. This is called elliptic flow and it is characterized by the elliptic flow parameter v_2, where v_2 is the second moment of the momentum distribution in the collision around the collision axis.

Since the QGP is very well described by ideal hydrodynamics, that means it is strongly coupled. The viscosity, η, is a measure of the ability of the medium to transfer momentum over distances. The stronger the interactions between particles, the harder it is for momentum to transfer across distances that are long compared to $\sim s^{-1/3}$, where s is the entropy density, since the particles will be colliding more, and

hence the smaller η/s. For example, for weakly interacting $\lambda\phi^4$ theory, $\eta/s \sim \lambda^{-2}$ [36]. Therefore, large coupling means low η/s ratio. In the case of the QGP produced at RHIC, this ratio is found to be between 0 and 0.2 [35], implying that the QGP produced is strongly interacting. As we cannot use perturbation theory for strongly coupled systems, we need to find alternative methods in dealing with such cases. The gauge/gravity duality (AdS/CFT correspondence) which will be described below in Section 1.2, is one such approach. It is used to calculate, among other things, some properties of strongly coupled plasmas although not exactly the QGP of QCD. These plasmas have been found to have an η/s ratio equal to $1/4\pi \sim 0.1$, [37] which is very similar to the ratio measured for the QGP produced at RHIC. The ratio η/s is one of the universal properties that are similar in all strongly coupled theories with a dual gravitational description and many colors.

1.1.4 Probing the Quark-Gluon Plasma - J/Ψ suppression and jet quenching

As we learned in the previous Section, heavy-ion collisions produce a strongly coupled QGP. Now let us see some experimental observables that can be used to learn more about the properties of this plasma, which will also be the focus of later Chapters. As the attraction between electrons is screened when placed in an ordinary plasma compared to vacuum, it is reasonable to think that the attraction between quarks will be screened when placed in the QGP. Due to the presence of the medium, the interactions between the quarks inside mesons or baryons become weaker and there is a point where these composite particles dissociate into their constituents. One can define the screening length, L_s, which is roughly the size of the largest hadrons which remain bound at a given T. But are there any hadrons that survive above the deconfinement temperature T_c? Hadrons made out of light quarks all have the same size (roughly 1 fm) and they all dissociate at the deconfinement transition temperature. On the other hand, hadrons made out of heavy quarks, for example charm and bottom quarks, have much smaller sizes and thus survive as bound states

even at higher temperatures, above the deconfinement transition. Examples of such hadrons are the J/Ψ ($c\bar{c}$) and Υ ($b\bar{b}$). Lattice calculations of the $q\bar{q}$-potential indicate that the ground state of the J/Ψ dissociates at a temperature $\sim 2\,T_c$ [38, 39]. This is the reason the J/Ψ suppression has been suggested to be an ideal probe for the QGP properties itself [40]. Data from SPS and RHIC do indeed demonstrate the existence of such suppression [41] and will be further studied at the LHC.

One significant difficulty in explaining the data is that in lattice calculations, the quark-antiquark pair is treated in the rest frame of the QGP but in collision experiments, the $c\bar{c}$-pair is created with some velocity. The AdS/CFT correspondence has been used in order to calculate the screening length of a heavy $q\bar{q}$-pair (a meson) moving though a strongly coupled plasma obtaining [42]:

$$L_s^{\mathrm{meson}}(v,T) \simeq L_s^{\mathrm{meson}}(0,T)(1-v^2)^{1/4} \propto \frac{1}{T}(1-v^2)^{1/4} \, , \qquad (1.4)$$

for large velocities. Expression (1.4) implies that the faster a mesons moves, the smaller its screening length is. Chapter 3 will be focused on the screening length calculation for a heavy baryon also using the AdS/CFT correspondence. It turns out that the baryon screening length also scales with velocity as expression (1.4) for large velocities, thus verifying the robustness of this scaling behavior. Note that these mesons and baryons studied using the AdS/CFT correspondence are not the same in all respects as the mesons and baryons found in QCD. These are external heavy quarks moving in plasma of $\mathcal{N} = 4$ Supersymmetric Yang-Mills (SYM) theory, which will be discussed in the next Section.

When a very energetic parton is produced in nucleus-nucleus collisions, it must go through the hot strongly coupled plasma that is present in the early times after the collisions. Unless the parton is produced near the edge of this fire ball and heading outwards, it has to propagate roughly 5-10 fm in this medium. These high transverse momentum partons manifest themselves in the detector as jets. Experimental results exist for back-to-back jets which arise from high transverse momentum partons produced near the edge of the fire ball, with one parton going through the QGP

and the other exiting immediately [43] (compared to the jets arising in proton-proton collisions where there is no QGP produced). These results show that the away-side jet (defined as hadrons with transverse momentum $p_T > 2$ GeV) is missing which implies that the parton that propagated through the medium lost so much energy that it produced no hadrons with $p_T > 2$ GeV and instead its energy went into soft particles. This is what we call jet quenching: a class of experiments where energetic quarks or gluons produced in rare high transverse momentum elementary interactions in the initial stage of the collision move through the fluid. For a recent review on jet quenching see [44] and References within. As the parton moves through the strongly coupled plasma, it not only looses energy but as it gets kicked by gluons, it acquires a transverse momentum (transverse with respect to its original direction of motion) in what is called transverse momentum broadening. The AdS/CFT correspondence has been used in order to calculate the jet quenching parameter $\hat{q}$ by evaluating Wilson loops [45, 46, 47, 48, 49, 50, 51, 52, 53, 54, 55].

Jet quenching has so far been studied in the weakly coupled QCD regime and only using a holographic calculation for the calculation of the jet quenching parameter. This is valid only for high energy jets where there is a clear separation of scales, which is not the case in the jets currently produced at RHIC. As the AdS/CFT correspondence can be used to study strongly coupled field theories (in particular $\mathcal{N} = 4$ SYM theory, see next Section), we would like to use it in order to study the jet propagation and how it interacts with a strongly coupled plasma. In Reference [56], electrons and positrons are coupled to $\mathcal{N} = 4$ SYM and they studied their scattering through a virtual photon. It was found that energy flowed outwards in a spherically symmetric manner with no jets. Similar results of isotropization of radiation at strong coupling have been found in References [57, 58]. These results seemed to rule out the use of $\mathcal{N} = 4$ SYM theory to model jets. In Chapter 4 we will be discussing a set up where a quark is moving in a circle in the vacuum of $\mathcal{N} = 4$ SYM theory, which results in a beam of gluons that is tightly collimated in angle and that propagates outwards forever in the $\mathcal{N} = 4$ SYM theory vacuum without spreading in angle - something that looks like a jet. Even though this is not literally a QCD jet (as it is not produced

through the fragmentation of an initially far off-shell parton), it opens a new way of modeling jet quenching in heavy-ion collisions. The pattern of radiation that we find is very similar to that of synchrotron radiation produced by an electron in circular motion in classical electrodynamics. If we were to add a nonzero temperature to our calculation, we could watch the tightly collimated beam of synchrotron radiation interact with the strongly coupled plasma that would then be present. The beam of radiation should be slowed down from the speed of light to the speed of sound and should ultimately thermalize, and it would be possible to study how the length- and time-scales for these processes depend on the wavelength and frequency of the beam.

1.2 The Gauge/Gravity Duality

1.2.1 Motivation

It has long been known that black holes carry entropy that is proportional to the area of their horizon. This is very strange because we are used to working with local field theories where the degrees of freedom scale with the volume of the system, not its area. This suggests that gravity has the same number of degrees of freedom as some local quantum field theory (QFT) in one less dimension. This statement is made formal by the holographic principle [59, 60] which says that a theory of quantum gravity in a region of space (of dimension $d + 1$) is described by a non-gravitional theory (for example a QFT) living on the boundary of that region (of dimension d).

How can we interpret this extra dimension from the view of the QFT? In QFT, we usually regard observables as a function of the length scale we observe them. For example, we integrate out the short-distance degrees of freedom and reduce the theory to an effective theory living in a longer length scale. This is what is called the renormalization group (RG) flow. We can think of a QFT as many copies of the theory living at each length scale, where degrees of freedom smaller than that length scale are integrated out. We can turn this length scale dependence of a QFT into an extra spatial dimension and interpret the extra dimension of the quantum gravity as

the length scale (or energy scale) of the field theory living at the boundary.

But what type of gravity theory could it be? It turns out that the perturbative expansion of a non-abelian gauge theory in $1/N_c$ (in QCD, $N_c = 3$, which is the number of colors), when taking N_c to be large, looks very similar to the perturbative expansion in the string coupling constant, g_s, of a closed string theory. This makes it tempting to identify $g_s \sim 1/N_c$ and conjecture that the dual theory to the QFT is some type of a closed string theory.

We would like the gravity theory living in the $d + 1$ dimensions to have the symmetries of the d-dimensional field theory. One such symmetry is the d-dimensional Poincare symmetry (the group of isometries of Minkowski spacetime in d dimensions). If we also require the theory to be conformal (which includes scale invariance), then the $d + 1$-dimensional spacetime is uniquely determined to be the $(d + 1)$-dimensional Anti-de Sitter spacetime, AdS_{d+1}. This is a maximally symmetric spacetime with a constant negative curvature. Hence, a conformal field theory (CFT) should have a string theory description in AdS spacetime - the AdS/CFT correspondence!

1.2.2   The Duality

In the last Section we briefly motivated the duality between a conformal field theory and a string theory in AdS spacetime. The most well studied form of the correspondence is between $\mathcal{N} = 4$ $SU(N_c)$ Supersymmetric Yang-Mills (SYM) theory and type IIB string theory on $AdS_5 \times S_5$ spacetime [61, 62, 63, 64]. $\mathcal{N} = 4$ SYM theory is a conformal nonabelian gauge theory which has a massless spin 1 gluon, four massless spin 1/2 gluinos and six massless spin 0 scalars, all in the adjoint representation linked by the $\mathcal{N} = 4$ supersymmetry. The theory is specified by two parameters: the number of colors N_c and the 't Hooft coupling λ which is defined as

$$\lambda \equiv g_{YM}^2 N_c, \tag{1.5}$$

where g^2_{YM} is the gauge coupling. These parameters imprint themselves in the string theory via the string coupling, g_s and the curvature scale of AdS, R_{AdS},

$$4\pi g_s = \lambda/N_c, \quad \frac{R^4_{AdS}}{l^4_s} = \lambda, \tag{1.6}$$

where l_s is a fundamental length scale, called the string length. In the large N_c limit, with λ kept constant, the string coupling becomes small and quantum effects can be neglected. When λ is then taken to be large (a strongly coupled field theory), the AdS curvature becomes very large compared to the string length. Since the string length is the typical size of a fundamental string, this limit implies that we can ignore the size of the strings and treat them as point particles. This is the same as omitting the contribution of all the massive string states in low-energy processes and only keeping the massless modes, i.e. the supergravity modes. Therefore, upon taking both of these limits, gauge theory problems can be solved using classical gravity in $AdS_5 \times S_5$ geometry. In this thesis we will only work in these two limits which implies that we are ignoring the stringy and quantum nature of the strings.

So what are these 10 dimensions? The five dimensions wrapped in the S_5 will play no role in the computations done in this thesis. The S_5 can be replaced by any compact five-dimensional space X_5 and our strong coupling results will be valid for all conformal quantum field theories with a dual classical gravity description — since conformality of the quantum theory maps onto the presence of an AdS_5 spacetime in the gravitational description.[2] The field theory lives in the four dimensions of the boundary of the AdS_5 spacetime (the bulk). The AdS_5 metric is given below, where we denote the fifth dimension by u (which is the inverse of the AdS_5 radial coordinate):

$$ds^2 = \frac{R^2_{AdS}}{u^2}(\eta_{\mu\nu}dx_\mu dx_\nu + du^2). \tag{1.7}$$

---

[2]Results will be valid for all strongly coupled conformal quantum field theories with a dual classical gravity description as long as we express our results in terms of the 't Hooft coupling λ in each of the conformal field theories. The relations between this parameter, N_c, and the parameters that specify the gravitational physics in the AdS_5 space — namely the string coupling and the dimensionless ratio of the AdS curvature and the string length — will be different in different conformal field theories, since these relations do depend on the geometry of X_5.

As $u \to 0$, we approach the boundary of the AdS_5 where the field theory lives. Note that due to the prefactor in front of the Minkowski metric, smaller values of the radial coordinate, i.e. larger values of u, (deeper in the bulk) correspond to larger length scales in the (3+1)-dimensional field theory. This is the IR/UV relationship that characterizes the AdS/CFT correspondence [65].

Suppose that we would like to turn on a finite temperature in the field theory on the boundary. We can modify the AdS space by adding a black hole and identifying the Hawking temperature arising from the black hole with the field theory temperature [61, 66]. The metric of AdS_5 with a black hole horizon at u_h is given by:

$$ds^2 = \frac{R_{AdS}^2}{u^2} \left[-f\, dt^2 + d\boldsymbol{x}^2 + \frac{du^2}{f} \right], \tag{1.8}$$

where

$$f = 1 - \frac{u^4}{u_h^4} \tag{1.9}$$

with Hawking temperature $T = 1/(\pi u_h)$ which is also the temperature of the field theory state.

One of the important maps between the two theories is the correspondence between gauge invariant local operators $\mathcal{O}(x)$ and fields in the bulk gravity theory $\phi(x, u)$. The correlators of such operators can be evaluated using the GKPW formula [67, 68], which assumes that the Euclidean partition functions of the two theories agree with certain boundary conditions. The GKPW formula relates the generating functional of the field theory in Euclidean time to the renormalized on-shell classical supergravity action:

$$\left\langle \exp \left(\int d^4x\, \phi_0(x)\, \mathcal{O}(x) \right) \right\rangle_{\text{CFT}} \sim \exp\left(S_{\text{grav}}[\phi(x, u)] \right), \tag{1.10}$$

where we have absorbed the minus signs in the exponents using the Euclidean time. On the left hand side, we are calculating an expectation value with some source ϕ_0, where ϕ_0 is the field in AdS dual to the operator $\mathcal{O}$ of the field theory. On the right hand side, we are calculating the partition function of the gravitational

theory evaluated at ϕ which solves the appropriate field equation in the bulk with the constraint that ϕ has a boundary value ϕ_0 (i.e. as $u \to 0$). Using the formula (1.10), we can calculate connected correlation functions of the gauge theory by taking derivatives of the on-shell classical supergravity action:

$$\langle \mathcal{O}(x_1)\, \mathcal{O}(x_2) \, ... \, \mathcal{O}(x_n) \rangle = \left. \frac{\delta^n S_{\text{grav}}[\phi(x,u)]}{\delta\phi_0(x_1)\, \delta\phi_0(x_2) \, ... \, \delta\phi_0(x_n)} \right|_{\phi_0=0}. \qquad (1.11)$$

One important application of the above formula is obtaining the gauge theory stress-energy tensor $T_{MN}(x)$. The source field in this case is the boundary value of the AdS metric $G_{MN}(x,u)$, which we will denote as $g_{\mu\nu}$. We obtain:

$$\langle T_{MN}(x) \rangle = \lim_{u \to 0} \frac{2}{\sqrt{-g(x,u)}} \frac{\delta S[g]}{\delta g_{\mu\nu}(x,u)}, \qquad (1.12)$$

where we have divided by the square root of the metric determinant in order to construct the stress-energy tensor (instead of the tensor density). Expression (1.12) will become useful in Chapter 4, where we will calculate the radiation coming from a quark moving in a circle.

As we have mentioned before, all the degrees of freedom in $\mathcal{N} = 4$ SYM are in the adjoint representation. But the quarks in QCD are in the fundamental representation, hence we should find a way to add them to the $\mathcal{N} = 4$ SYM theory. A way to do this is to add a probe D3-brane. A Dp-brane is a "defect", where closed strings can break and open strings can end, that occupies a p-dimensional (spatial) subspace. The probe D3-brane is extended along the x_1, x_2, x_3-directions (the spatial dimensions of the gauge field theory) at some $u = \Lambda \ll u_h$. The external quarks are open strings that end on the probe brane and hang down in the bulk. The quark mass, m_q, is related to the probe brane location, Λ, by $m_q = R^2_{AdS}/(2\pi l_s^2 \Lambda)$. We can then take the infinite quark mass limit, $\Lambda \to 0$, where the probe brane sits at the boundary in order to simplify our calculations. A meson in this picture is a string connecting the two string endpoints at the boundary (the quark and antiquark) which hangs down into the fifth dimension. Figure 1-4 shows a sketch of these configurations.
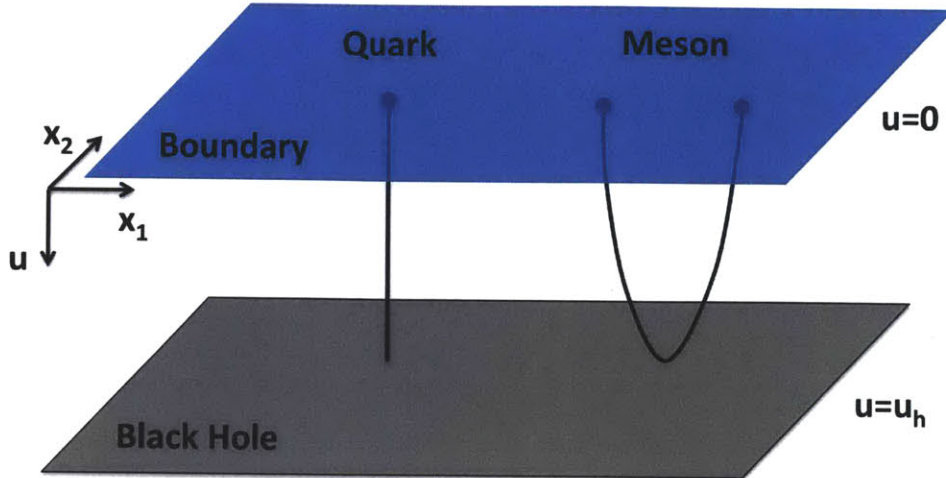
Figure 1-4: Schematic picture of AdS_5 black hole indicating the presence of an external quark and an external meson. We only show two of the four boundary dimensions (x_1, x_2) and the (inverse) radial coordinate u.

Note that the quarks added in this way are external quarks and are not fundamental degrees of freedom added to the $\mathcal{N} = 4$ SYM theory. The way to add N_f $\mathcal{N} = 2$ hypermultiplets in the fundamental representation of the gauge group (where N_f is the number of flavors and $N_f \ll N_c$), is to add N_f D7-branes in the black hole geometry (1.8) [69, 70, 71]. In this thesis we will only add external quarks to $\mathcal{N} = 4$ SYM theory.

Now let us outline the main steps we will follow in subsequent Chapters in obtaining properties of the field theory from a given gravity configuration. Suppose we have an external quark moving in the finite temperature $\mathcal{N} = 4$ SYM plasma. Let us denote the string worldsheet coordinates by (τ, σ). Then:

1. Write down the string profile which is determined by a set of embedding functions $X^M(\tau, \sigma)$ that specify where in the spacetime described by the metric G^{MN} the point (τ, σ) on the string worldsheet is located. The index M runs over the five AdS_5 coordinates (as the S_5 will not play any role in our calculations).

2. Calculate the induced world sheet metric which is given in terms of these embedding functions by

$$g_{ab} = G_{MN} \, \partial_a X^M \partial_b X^N, \tag{1.13}$$

37

where a and b each run over (τ, σ) and G_{MN} is the AdS_5 metric given in (1.8).

3. Calculate the Nambu-Goto action which governs the dynamics of classical strings

$$S_{\mathrm{NG}} = -T_0 \int d\tau \, d\sigma \sqrt{-g}, \qquad (1.14)$$

where $T_0 = \sqrt{\lambda}/2\pi R_{AdS}^2 = 1/2\pi\alpha'$ is the string tension and $g = \det g_{ab}$.

4. Calculate and solve the classical equations of motion using the Euler-Lagrange equations, with appropriate boundary conditions, in order to find the embedding functions $X^M(\tau, \sigma)$.

5. Using the embedding functions we can calculate properties of the plasma and of matter moving through it. For example, the energy of the quark can be calculated by plugging X^M back to the Lagrangian. The energy and flux through some area of the QGP caused by the motion of a quark can be calculated using the operator/field correspondence (1.12).

1.2.3 Universality and Applications

In the previous Sections we sketched how to use classical supergravity calculations in order to understand properties of strongly coupled $\mathcal{N} = 4$ $SU(N_c)$ SYM theory. But given that we do not have a dual gravity theory to QCD, how reasonable is it to apply the AdS/CFT correspondence as an attempt to understand QCD?

At the microscopic level, $\mathcal{N} = 4$ SYM is very different from QCD: the theory is conformal, supersymmetric and it contains an additional global symmetry. It has no dynamic quarks but has additional scalar and fermionic fields in the adjoint representation. Its coupling does not run, there is no confinement, no chiral symmetry and hence no chiral symmetry breaking. These features make the vacua of the two theories very different, but the differences become less important when we look at temperatures above the deconfinement transition of QCD, i.e. above T_c. We know that supersymmetry is broken for finite temperatures and, above T_c in QCD, there is no confinement and no chiral condensate. Since $\mathcal{N} = 4$ SYM is conformal and QCD

38

is not, we cannot use it to describe QCD at or below T_c. However, lattice calculations indicate that QCD thermodynamics is reasonably well approximated as conformal when the temperature is increased above about $(1.5 - 2)\, T_c$ [72, 73, 74]. A difference that still remains is the number of degrees of freedom. We can scale out this difference by taking ratios. An example of this is the ratio of the energy density of the plasma (which scales with the number of degrees of freedom) to the energy density at zero coupling. The calculation in $\mathcal{N} = 4$ SYM can be done at strong coupling using gravity and the result is 0.75 [75]. Lattice calculations with two and three flavors suggest that for temperatures above $T \sim 1.2\, T_c$, this ratio takes a value of around 0.8 [76, 77, 78].

The question now becomes whether there are any universal quantities we can calculate that have qualitative or semiquantitative similarities among many different strongly coupled plasmas and hopefully also with QCD. One such example is the ratio of viscosity to entropy density, η/s, which is equal to $1/4\pi$ for all theories with string theory duals in the large-N_c and strong coupling limits [37, 79, 80, 81, 82]. As we have mentioned in Section 1.1.3, this ratio for the QGP created at RHIC is between 0 and 0.2. This result makes us hope that QCD is in the same group of theories as other calculable strongly coupled plasmas and we will try to make predictions based on this. In this thesis we will discuss some other quantities and argue that they apply to a large number of strongly coupled plasmas and hopefully also to QCD.

As we have mentioned in Section 1.1.4, one application of the AdS/CFT correspondence is the calculation of the velocity dependence of the meson screening length. A very nice picture arises from the string theory side for non-zero temperatures. For meson sizes smaller than the screening length, L_s, the energetically favorable string configuration is a string hanging down in the bulk connecting the two end-points (the quark and antiquark) on the boundary. On the other hand, due to the presence of the black hole, for meson sizes larger than L_s, the energetically favorable configuration is simply two strings hanging down into the black hole unaware of each other. This indicates a complete loss of interaction between the quarks and the meson has been completely screened. Figure 1-5 shows a sketch of these string configurations. In
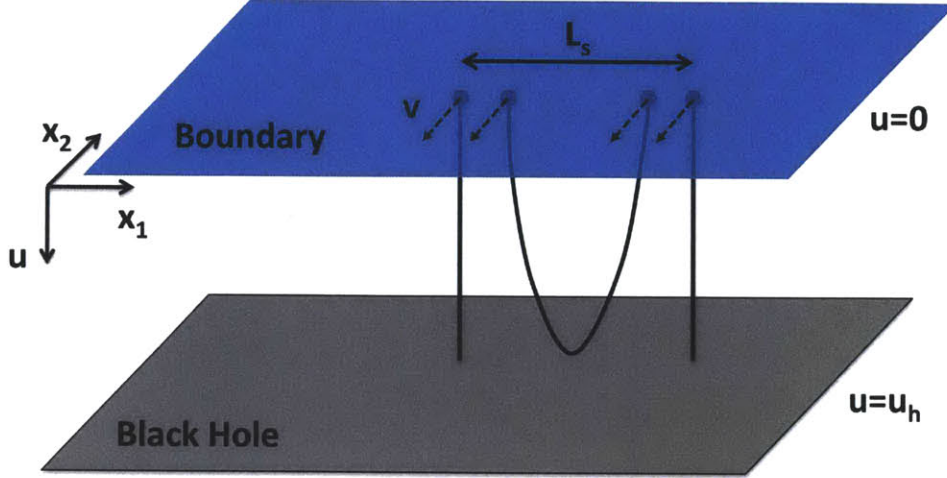
Figure 1-5: Schematic picture of AdS_5 black hole and the computation of the meson screening length between a quark and antiquark moving with velocity v, from hanging semiclassical strings. The preferred configuration beyond a certain separation L_s (screening length) consists of two independent strings.

Chapter 3 we will do a similar calculation but with N_c quarks arranged in a circle, which represents a baryon in the $\mathcal{N} = 4$ SYM theory.

Another application of the AdS/CFT correspondence is the calculation of properties of a quark moving through a strongly coupled plasma. The calculation of the drag force felt by a quark moving through a sQGP has been done in $\mathcal{N} = 4$ SYM theory [83, 84] and in many other gauge theories with dual gravitational descriptions [85, 86, 87, 88, 89, 90, 91, 92, 93]. The calculation of the drag on heavy quarks involves the calculation of the momentum flux flowing down from the boundary, along the string world sheet and towards the horizon, which determines the amount of momentum lost by the quark in its propagation through the plasma.

In Section 1.1.4, we mentioned that a quark rotating in a circle results to a beam of gluons that is tightly collimated in angle and that propagates outwards forever in the $\mathcal{N} = 4$ SYM theory vacuum without spreading in angle (synchrotron radiation), which opens a new way of modeling jet quenching in heavy-ion collisions. Details of the calculations for the energy disturbance caused by the quark are presented in Chapter 4, but here we will briefly discuss the picture that arises from the gravitational side. In AdS_5, the string hangs down into the bulk and coils around on itself as it extends

in the AdS_5 radial direction due to the motion of the quark at the boundary (see Figure 4-1 in Chapter 4). The presence of the string in turn perturbs the geometry and the near-boundary perturbation in the geometry induces a $4d$ stress tensor on the boundary. The induced stress has the interpretation as the expectation value of the stress tensor in the dual quantum field theory. Using this interpretation we obtain the energy density and angular distribution of the power radiated by the quark in the field theory side. Reference [94] gives a nice geometric description of our results where this geometry perturbation from the string is reproduced by a superposition of gravitational shock waves emitted perpendicular to the motion of the string and towards the boundary.

The remainder of this thesis is organized as follows: In Chapter 2, we present a detailed analysis of higher moments of pion, proton, net proton and mixed particle multiplicities in the search for the QCD critical point. We also show how to use nontrivial but parameter independent ratios among these more than a dozen fluctuation observables to discover the critical point, if it is located in an experimentally accessible region. In Chapter 3 we will use the AdS/CFT correspondence in order to calculate the velocity dependence of the screening length of a baryon (N_c quarks arranged in a circle) moving though a strongly coupled $\mathcal{N} = 4$ SYM plasma. We will then, in Chapter 4, use the AdS/CFT correspondence to compute the energy density and angular distribution of the power radiated by a quark undergoing circular motion in a strongly coupled plasma of any conformal field theory that has a dual classical gravity description, which results to a radiation pattern that is very similar to synchrotron radiation produced by an electron in circular motion in classical electrodynamics. Chapters 2, 3 and 4 are based upon Refs. [95], [96] and [97], respectively.

Chapter 2

Locating the QCD Critical Point Using Fluctuations

2.1 Introduction and Illustrative Results

The second-order critical point at which the first-order transition between hadron matter and QGP ends is one of the distinctive features of the QCD phase diagram. Since we currently do not have a systematic way of locating this point from first principles as model and lattice calculations face many challenges and much work still needs to be done in order to overcome them (for reviews, see Refs. [14, 15, 16, 17, 18, 19, 20, 21, 22]), our best bet is to locate it experimentally. Experiments with this goal are underway and planned at the Relativistic Heavy-Ion Collider (RHIC) at the Brookhaven National Laboratory (BNL) and at the Super Proton Synchrotron (SPS) at CERN in Geneva [98, 99, 100, 101]. These experiments involve colliding heavy nuclei (gold nuclei at RHIC and lead nuclei at SPS) at high energies and observing the resulting particle distributions. It is therefore important to define, evaluate the utility of, and select experimental observables that will allow us to locate the critical point, if it is located in an experimentally accessible region.

As we discussed in Chapter 1, in heavy-ion collision experiments, the center of mass energy $\sqrt{s}$ is varied, thus changing the temperature and chemical potential of the produced matter and in this way scanning the phase diagram. The observed

collective flow of the produced matter at RHIC strongly suggests the production of a strongly-coupled quark-gluon plasma [7, 102]. As the QGP expands and cools, it follows a path on the phase diagram that is characterized by approximately constant entropy density to baryon number density ratio until freeze-out, after when there are no further interactions that change the multiplicities of hadron species. When these particles are then detected, they give us information about the state of the matter at the freeze-out point. Therefore, in order to see the effects of the critical point on observables, one should try to get the freeze-out point as close to the critical point as possible by varying the collision center of mass energy, $\sqrt{s}$. Decreasing $\sqrt{s}$ decreases the entropy to baryon number ratio, and therefore corresponds to increasing the baryon number chemical potential, μ_B, at freeze-out.

Present lattice calculations evade the fermion sign problem in different ways that all rely upon the smallness of $\mu_B/(3T)$. Although each is currently limited by systematic effects, and they do not give consistent guidance as to the location of the critical point, all present lattice calculations agree that it is not found at $\mu_B < T$, where the calculations are most reliable [103, 104, 105, 106]. For this reason, experimental searches focus on collisions which freezeout with $\mu_B > 150$ MeV. The upper extent of the experimentally accessible region of the phase diagram is determined by the largest freezeout μ_B at which collisions still have a high enough $\sqrt{s}$ that the matter they produce reaches temperatures in the transition region.

Upon scanning in $\sqrt{s}$ and thus in μ_B, one should then be able to locate (or rule out the presence of) the critical point by using observables that are sensitive to the proximity of the freeze-out point to the critical point [31, 30]. For example, for particles like pions and protons that interact with the critical mode, the fluctuations in the number of particles in a given acceptance window will increase near the critical point as the critical mode becomes massless and develops large long-wavelength correlations. As we vary $\sqrt{s}$, therefore, if the freeze-out point approaches the critical point, we would see an increase in the fluctuations in the number of those particles which interact with the critical mode. These fluctuations would then decrease as we move away from the critical point. (This is true for any observables which are sensitive

44

to the proximity of the critical point to the point where freeze-out occurs.) Hence, a characteristic signature of the critical point is the non-monotonic behavior of such variables, as a function of $\sqrt{s}$ [31, 30]. Another way to change the freeze-out point is by changing the size of the system by varying the centrality of the collisions, since larger systems freeze-out later and hence at somewhat smaller temperatures.

In this Chapter we describe how to use the increase in fluctuations of particle numbers near the critical point as a probe to determine its location. The way one characterizes the fluctuations of an observable is by measuring it in each event in an ensemble of many events, and then measuring the variance and higher, non-Gaussian, moments of the event-by-event distribution of the observable. The contribution of the critical fluctuations to these moments is proportional to some positive power of ξ, the correlation length which, in the idealized thermodynamic limit, diverges at the critical point. In reality, ξ reaches a maximum value at the critical point but does not diverge because as it cools the system spends only a finite time in the vicinity of the critical point. The system also has only a finite size, but it turns out that the finite time is a more stringent limitation on the growth of the correlation length [30, 27]. Estimates of the rate of growth of ξ as the collision cools past the critical point (which take into account the phenomenon of critical slowing down) suggest that the maximal value of ξ that can be reached is around $1.5 - 3$ fm [27, 28, 29], compared to the natural ~ 0.5 fm away from the critical point. Higher moments depend on higher powers of ξ, making them more favorable in searching for the critical point [32]. In this Chapter we consider the second, third and fourth cumulants of particle multiplicity distributions for pions and protons. We also consider mixed pion-proton cumulants, again up to fourth order.

Our goal in this Section is to provide an illustrative example of one possible experimental outcome. In Section 2.1.1 we define the observables that must be measured at each $\sqrt{s}$. In Section 2.1.2 we suppose that the critical point is located at $\mu_B = 400$ MeV and then guess how the correlation length ξ at freezeout will vary with the chemical potential μ_B, and hence with $\sqrt{s}$, in a heavy-ion collision program in which the beam energy is scanned. In Section 2.1.3 we plot results for how seven

of the observables that we define will vary with μ_B, if the guess for $\xi(\mu_B)$ that we have made for illustrative purposes were to prove correct. In Section 2.2 we provide the calculation of all the observables that we define, as a function of ξ, the proton and pion number densities, and four nonuniversal parameters that must ultimately be obtained from data. In Section 2.3 we construct ratios of observables that allow us to measure four combinations of ξ and the four parameters. And, we construct five ratios of observables which receive a contribution from critical fluctuations that is independent of ξ and independent of all four currently poorly known parameters. This means that we make robust predictions for these five ratios, predictions that could be used to provide a stringent check on whether enhanced fluctuations discovered in some experimental data set are or are not due to critical fluctuations. We close in Section 2.4 with a discussion of remaining open questions.

We shall find that critical fluctuations can easily make contributions to the higher moments of the proton multiplicity distribution that are larger than those in a Poisson distribution by more than a factor of 100. In Appendix A we convince ourselves that we can construct a reasonable looking, but somewhat *ad hoc*, distribution whose higher moments are this large. What we are able to calculate in Section 2.2 is moments of the distribution, not the distribution itself. In Appendix A we construct a toy model distribution that has moments comparable to those we calculate. We also use this toy model to obtain a crude gauge of how our results would be modified by any effects that serve to limit the maximum proton multiplicity in a single event.

In Appendix B we apply our calculation to determine the contribution of critical fluctuations to the third and fourth cumulants of the event-by-event distribution of the mean transverse momentum of the pions in an event. We find that the critical contribution to these non-Gaussian cumulants are quite small, smaller even than the contributions of Bose-Einstein statistics. For this reason, throughout the main text of this Chapter we focus entirely on number fluctuations, rather than transverse momentum fluctuations.

2.1.1 Moments and cumulants of fluctuations

We expect to see a peak in the Gaussian and non-Gaussian cumulants of particle multiplicity distributions near the critical point as we change $\sqrt{s}$. In this subsection, we describe how to calculate these higher cumulants from experimental data.

Consider an ensemble of events in each of which we have measured the number of particles of two species, which we shall denote x and y. The possibilities for x and y that we consider later include the number of pions N_π, the number of protons N_p, and the number of protons minus antiprotons $N_{p-\bar{p}} \equiv N_p - N_{\bar{p}}$. In each case, the number that is tallied should be the number of particles of the desired species near mid-rapidity in a specified window of rapidity. This window in rapidity should be at least about one unit wide, in order for our results to apply without significant acceptance corrections [107]. Furthermore, the longitudinal expansion of the matter produced in the collision reduces correlations among particles separated by much more than one unit in rapidity [107], making larger windows unnecessary.

We denote the average value of x and y over the whole ensemble of events by $\langle x \rangle$ and $\langle y \rangle$. Throughout this Chapter, we use single angle brackets to indicate the ensemble average of a quantity whose event-by-event distribution has been measured. And, we shall denote the deviation of x and y from their mean in a single event by

$$
\begin{aligned}
\delta x &\equiv x - \langle x \rangle \\
\delta y &\equiv y - \langle y \rangle
\end{aligned}
\tag{2.1}
$$

We now define the cumulants of the event-by-event distribution of a single observable, say x. The second and third cumulants are given by

$$
\kappa_{2x} \equiv \langle\langle x^2 \rangle\rangle \equiv \langle (\delta x)^2 \rangle
\tag{2.2}
$$

$$
\kappa_{3x} \equiv \langle\langle x^3 \rangle\rangle \equiv \langle (\delta x)^3 \rangle \, ,
\tag{2.3}
$$

where we have introduced two equivalent notations for the cumulants. The second cumulant κ_{2x} is the variance of the distribution, while the skewness of the distribution

is given by $\kappa_{3x}/\kappa_{2x}^{3/2}$. The fourth cumulant is different from the corresponding fourth moment:

$$\kappa_{4x} \equiv \langle\langle x^4 \rangle\rangle \equiv \langle (\delta x)^4 \rangle - 3 \langle (\delta x)^2 \rangle^2 \ . \tag{2.4}$$

The kurtosis of the distribution is given by $\kappa_{4x}/\kappa_{2x}^2$.

The defining property of the cumulants is their additivity for independent variables. For example, if a and b are two independent random variables, then $\kappa_{i(a+b)} = \kappa_{ia} + \kappa_{ib}$. This property is easily seen from the cumulant generating function

$$g(\mu) = \log\langle e^{\mu\,\delta x} \rangle \ , \tag{2.5}$$

which is manifestly additive. The n'th cumulant of the x-distribution is given by

$$\kappa_{nx} = \left. \frac{\partial^n g(\mu)}{\partial \mu^n} \right|_{\mu=0} \ . \tag{2.6}$$

Using the double bracket notation introduced above, $g(\mu) = \langle\langle e^{\mu x} \rangle\rangle$. As a result of their additivity, cumulants of *extensive* variables, such as N_p or N_π, are all themselves extensive, meaning that they are proportional to the volume of the system V in the thermodynamic limit.

We shall also consider mixed cumulants, which generalize the more familiar Gaussian measures of correlations to non-Gaussian measures. These are generated by

$$g(\mu, \nu) \equiv \sum_{n,m} \frac{\kappa_{nxmy}\, \mu^n \nu^m}{m!\, n!} = \log\langle e^{\mu\,\delta x + \nu\,\delta y} \rangle \ , \tag{2.7}$$

and, for example, are given by

$$\kappa_{1x1y} \equiv \langle\langle xy \rangle\rangle = \langle \delta x\, \delta y \rangle \ , \tag{2.8}$$

$$\kappa_{1x2y} \equiv \langle\langle xy^2 \rangle\rangle = \langle \delta x\, (\delta y)^2 \rangle \ , \tag{2.9}$$

$$\kappa_{2x2y} \equiv \langle\langle x^2 y^2 \rangle\rangle = \langle (\delta x)^2 (\delta y)^2 \rangle - 2\langle \delta x\, \delta y \rangle^2 - \langle (\delta x)^2 \rangle \langle (\delta y)^2 \rangle \ , \tag{2.10}$$

$$\kappa_{1x3y} \equiv \langle\langle xy^3 \rangle\rangle = \langle \delta x\, (\delta y)^3 \rangle - 3 \langle \delta x\, \delta y \rangle \langle (\delta y)^2 \rangle \ . \tag{2.11}$$

48

For two extensive variables x and y such mixed cumulants are also extensive, proportional to V.

We have described how to obtain the cumulants κ_{ix}, κ_{jy} and κ_{ixjy} from a data set consisting of an ensemble of events in each of which x and y have been measured. We can now define the *intensive* normalized cumulants that we shall analyze:

$$\omega_{i\pi} \equiv \frac{\kappa_{i\pi}}{\langle N_\pi \rangle} \, , \tag{2.12}$$

$$\omega_{ip} \equiv \frac{\kappa_{ip}}{\langle N_p \rangle} \, , \tag{2.13}$$

$$\omega_{i(p-\bar{p})} \equiv \frac{\kappa_{i(p-\bar{p})}}{\langle N_p + N_{\bar{p}} \rangle} \, , \tag{2.14}$$

$$\omega_{ipj\pi} \equiv \frac{\kappa_{ipj\pi}}{\langle N_p \rangle^{i/r} \langle N_\pi \rangle^{j/r}} \, , \tag{2.15}$$

$$\omega_{i(p-\bar{p})j\pi} \equiv \frac{\kappa_{i(p-\bar{p})j\pi}}{\langle N_p + N_{\bar{p}} \rangle^{i/r} \langle N_\pi \rangle^{j/r}} \, , \tag{2.16}$$

where $r \equiv i + j$.

If N_π, N_p and $N_{\bar{p}}$ are statistically independent and Gaussian distributed, then the ω_2's in (2.12), (2.13) and (2.14) are nonzero and all the other ω's vanish.

If N_π, N_p and $N_{\bar{p}}$ are statistically independent and Poisson distributed, then all the ω_i's in (2.12), (2.13) and (2.14) with $i \geq 2$ are equal to 1, and all the mixed cumulants vanish and therefore so do the ω's in (2.15) and (2.16).

In this Chapter we shall calculate the contributions of critical fluctuations to the normalized cumulants (2.12), (2.13) and (2.14) for $i = 2$, 3 and 4 and the normalized mixed cumulants (2.15) and (2.16) for i's and j's such that $r = 2$, 3 and 4.

2.1.2 Dependence of ξ on μ_B

We shall close this Introduction (in Section 2.1.3) by illustrating *possible* experimental outcomes of measurements of the cumulants defined in Section 2.1.1, assuming that the matter produced at the freezeout point of the fireball evolution for some collision energy $\sqrt{s}$ is near the critical point. In Section 2.1.3 we shall present only results, while the calculations involved are presented in Section 2.2. What we shall calculate

49

in Section 2.2 is the contribution of critical fluctuations to the observables defined in Section 2.1.1 in terms of the correlation length ξ. In order to give an example of possible experimental outcomes, we need to make an illustrative choice of how the correlation length ξ that is achieved in a heavy-ion collision depends on μ_B.

To start, let us assume that the critical point occurs at $\mu_B^c = 400$ MeV. Let us also assume that because the fireball only spends a finite time in the vicinity of the critical point the correlation length reaches a maximum value of $\xi_{\max} = 2$ fm in the collisions in which the freeze-out point is closest to the critical point during an energy scan. We stress that our choices of μ_B^c and $\xi_{\max}$ are arbitrary, made for illustrative purposes only, and are in no way predictions.

How does the correlation length achieved in a heavy-ion collision depend on the μ_B at which the matter produced in the collision freezes-out? Close to the critical point, the equilibrium correlation length ξ_{eq} is very long and there is not sufficient time for the actual correlation length ξ achieved in a collision to reach ξ_{eq} [27]. Lets suppose that ξ reaches ξ_{eq} for $|\mu_B - \mu_B^c| \gtrsim W$, for some W, while for $|\mu_B - \mu_B^c| \lesssim W$ finite time effects limit ξ such that it peaks at $\xi_{\max}$. In principle, $\xi_{eq}(\mu_B)$ could one day be determined from lattice QCD calculations, but these calculations are challenging at $\mu \neq 0$ because of the notorious fermion sign problem, so this day remains in the future. At present, all we can do is require that the static correlation length ξ_{eq} satisfy the constraints imposed by the universality of critical behavior at long wavelengths. The universal behavior is really only attained in the limit in which $W \rightarrow 0$ and $\xi_{\max} \rightarrow \infty$, so our use of it in the present context is illustrative but not quantitative. As a function of $\mu_B - \mu_B^c$, in the universal regime ξ_{eq} must scale as $\xi \rightarrow f_\pm |\mu_B - \mu_B^c|^{-\nu}$, where ν is the relevant critical exponent[1] and f_+ and f_- are the amplitudes of the

---

[1] For our illustrative model of the $\xi(\mu_B)$ dependence along the freezeout curve we are assuming that where the freezeout curve passes the critical point it is approximately parallel to the transition line (crossover and first-order lines). The region of the QCD phase diagram in the (μ_B, T) plane near the critical point can be mapped onto the Ising model phase diagram, whose reduced temperature and magnetic field axes are conventionally denoted by t and h, respectively. Upon approaching the Ising critical point along the t-direction, i.e., along the transition line, $\xi_{eq} \sim t^{-\nu} \sim t^{-2/3}$, while along the h-direction, $\xi_{eq} \sim h^{-\nu/\beta\delta} \sim h^{-2/5}$. As long as $h \ll t^{\beta\delta}$ on the freezeout curve, the t-like scaling dominates and, since $|\mu_B - \mu_B^c| \sim t$, we obtain $\xi_{eq} \sim |\mu_B - \mu_B^c|^{-\nu}$. The condition $h \ll t^{\beta\delta}$ is violated at points on the freezeout curve that are very close to the critical point, $t \approx 0$, where the h-like scaling sets in. For simplicity we assume that this small-t segment of the freezeout curve in

singularity on the crossover and first-order side of the transition respectively. The precise value of the critical exponent is $\nu = (2 - \alpha)/3 \approx 0.63$, with the numerical value being that for a critical point in the Ising universality class [108]. But, in our calculation in Section 2.2 we shall be neglecting the small anomalous dimensions associated with nonvanishing values of the exponents $\eta \approx 0.04$ and $\alpha \approx 0.1$. So, to be consistent, here too we shall simply use $\nu = 2/3$. The ratio of the amplitudes f_+/f_- is also a universal quantity. In the Ising universality class, $f_+/f_- \approx 1.9$ [109]. Since $f_+/f_- > 1$, the correlation length falls off more slowly on the crossover side $\mu < \mu_B^c$.

The simplest ansatz for $\xi(\mu_B)$ that we have found that incorporates the physics that we have just described is

$$\xi(\mu_B) = \frac{\xi_{\max}}{\left[1 + \frac{(\mu_B - \mu_B^c)^2}{W(\mu_B)^2}\right]^{1/3}} , \qquad (2.17)$$

with

$$W(\mu_B) = W + \delta W \tanh\left(\frac{\mu_B - \mu_B^c}{w}\right) \qquad (2.18)$$

where W and w are nonuniversal parameters to be chosen and δW is specified by requiring that

$$\frac{W + \delta W}{W - \delta W} = \left(\frac{f_+}{f_-}\right)^{3/2} = 1.9^{3/2} . \qquad (2.19)$$

We have constructed (2.17) such that ξ has the universal behavior of ξ_{eq} when $|\mu_B - \mu_B^c| \gg W(\mu_B)$, but has a peak that is cut off at $\xi = \xi_{\max}$ where $\mu_B = \mu_B^c$. We have chosen the shape of ξ in the vicinity of the peak arbitrarily, for illustrative purposes, not via analysis of the rate of growth of ξ during the finite duration in time of a heavy-ion collision. In Fig. 2-1 we show two instances of our ansatz for $\xi(\mu_B)$. They differ in their choice of the width of the peak. We shall define the width Δ as the distance in μ_B between the two points at which $\xi(\mu_B)$ crosses 1 fm, i.e. the width in μ_B within which $\xi > 1$ fm. The three curves in the figure have Δ=50, 100 and 200 MeV. In all three cases we have chosen $w = 0.1\Delta$. (With this choice, $W = 0.189\Delta$

---

the QCD phase diagram lies in a region where the equilibrium correlation length ξ_{eq} already exceeds $\xi_{\max} = 2$ fm, and thus $\xi \approx \xi_{\max}$ in this segment.
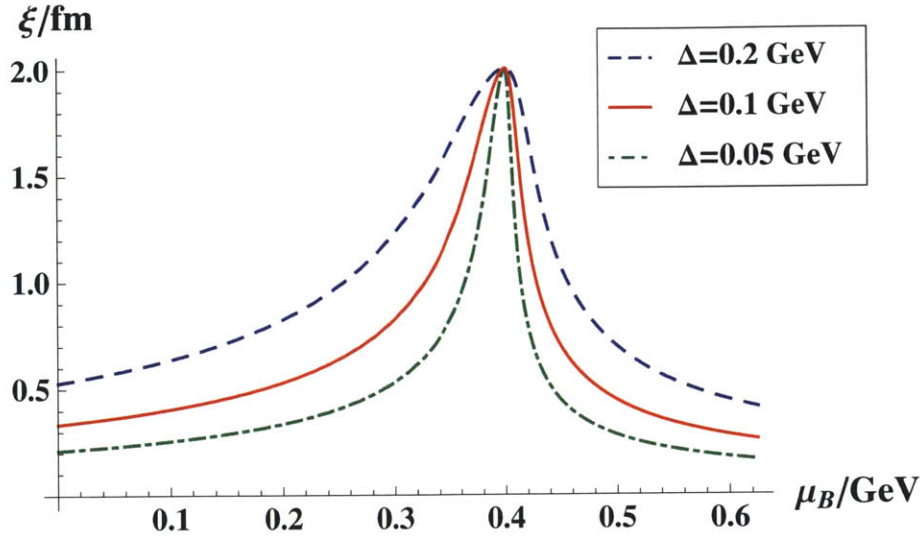
Figure 2-1: The correlation length $\xi(\mu_B)$ achieved in a heavy-ion collision that freezes out with a chemical potential μ_B, according to the ansatz described in the text. We have assumed that the collisions that freeze out closest to the critical point are those that freeze-out at $\mu_B^c = 400$ MeV. We have assumed that the finite duration of the collision limits ξ to $\xi < \xi_{\max} = 2$ fm. We show $\xi(\mu_B)$ for three choices of the width parameter Δ, defined in the text. The choices of parameters that have gone into this ansatz are arbitrary, made for illustrative purposes only. They are not predictions.

and $\delta W = 0.084\Delta$.) There is no reason to expect that Δ should be small and, indeed, in model calculations it seems to be larger than 100 MeV [110]. Ultimately Δ should be determined by lattice calculations; one first attempt to do so indicates $\Delta \sim 100$ MeV [105, 111].

2.1.3 Cumulants near the critical point

We shall concentrate our analysis on observables characterizing the fluctuations of pions and protons. Pions are the most abundant species produced in relativistic heavy-ion collisions. Protons are important, among other reasons, because their fluctuations are proxy to the fluctuations of the conserved baryon number [112] and because their coupling to the critical mode σ is relatively large.

We have defined the normalized cumulants of the proton and pion distributions in (2.13) and (2.12) and the normalized mixed cumulants in (2.15). Fig. 2-2 shows how
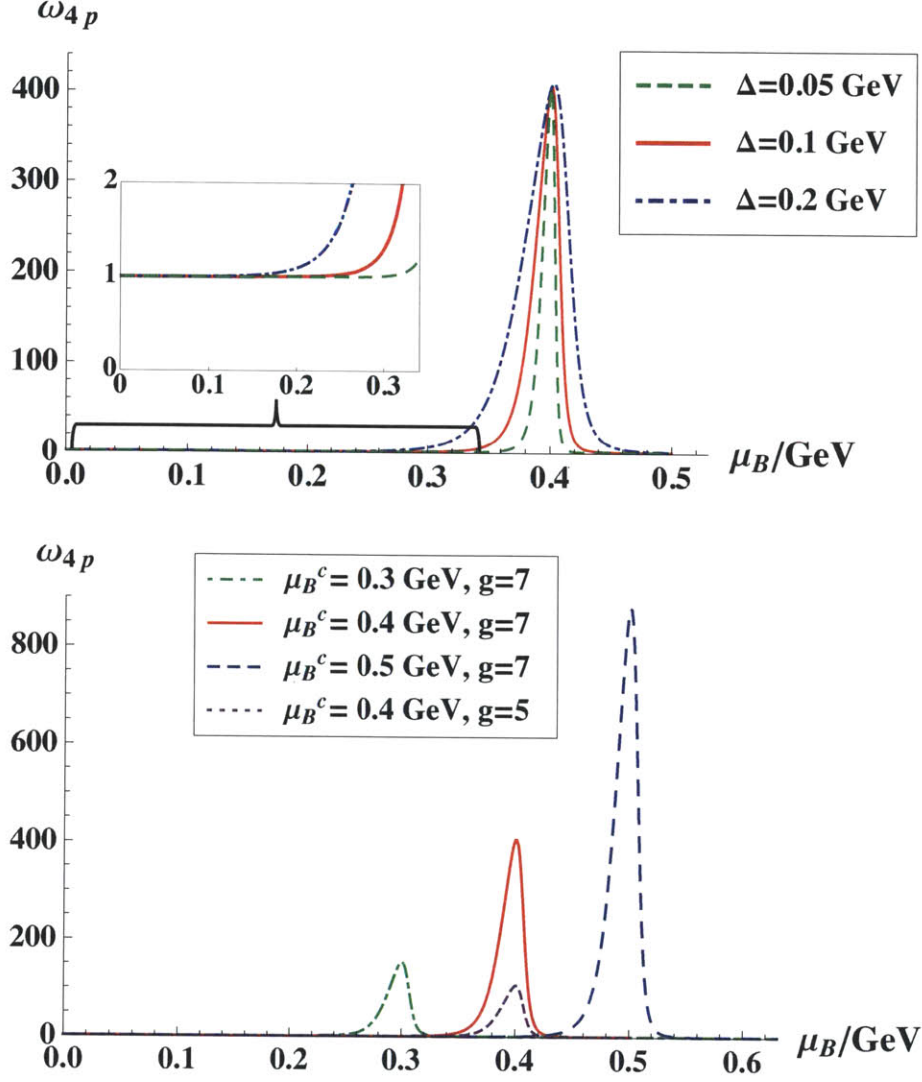
Figure 2-2: The μ_B-dependence of ω_{4p}, the normalized 4th cumulant of the proton number distribution defined in (2.13), with a μ_B-dependent ξ given by (2.17). We only include the Poisson and critical contributions to the cumulant. In the top panel we choose $\mu_B^c = 400$ MeV and illustrate how ω_{4p} is affected if we vary the width Δ of the peak in ξ from 50 to 100 to 200 MeV, as in Fig. 2-1. The inset panel zooms in to show how ω_{4p} is dominated by the Poisson contribution well below μ_B^c. In the lower panel, we take $\Delta = 100$ MeV and illustrate the effects of changing μ_B^c and of reducing the sigma-proton coupling g_p from our benchmark $g_p = 7$ to $g_p = 5$.
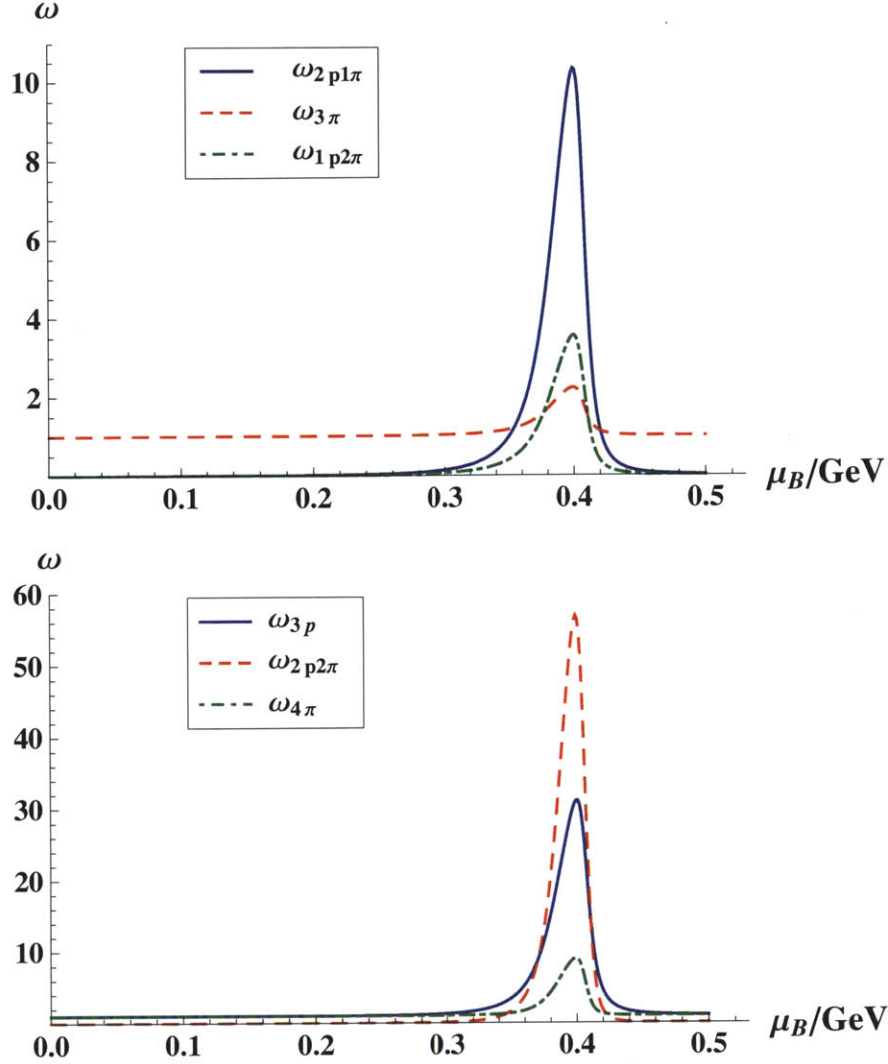
Figure 2-3: The μ_B-dependence of selected normalized cumulants, defined in (2.12), (2.13) and (2.15), with a μ_B-dependent ξ given by (2.17) as in Fig. 2-1. We only include the Poisson and critical contributions to the cumulants. We have set all parameters to their benchmark values, described in the text, and we have chosen the width of the peak in ξ to be $\Delta = 100$ MeV. Note the different vertical scales in these figures and in Fig. 2-2; The magnitude of the effect of critical fluctuations on different normalized cumulants differs considerably, as we shall discuss in Sections 2.2 and 2.3. As we shall also discuss in those Sections, ratios of the magnitudes of these different observables depend on (and can be used to constrain) the correlation length ξ, the proton number density n_p, and four non-universal parameters. We shall also see in Section 2.3 that there are ratios among these observables that are independent of all of these variables, meaning that we can predict them reliably. For example, we shall see that critical fluctuations must yield $\omega_{2p2\pi}^2 = (\omega_{4p} - 1)(\omega_{4\pi} - 1)$ and $\omega_{2p1\pi}^3 = (\omega_{3p} - 1)^2(\omega_{3\pi} - 1)$ and $\omega_{1p2\pi}^3 = (\omega_{3p} - 1)(\omega_{3\pi} - 1)^2$. (The subtractions of 1 are intended to remove the Poisson background; in an analysis of experimental data these subtractions could be done by subtracting the ω_{ip} or $\omega_{j\pi}$ determined from a sample of mixed events, as this would also subtract various other small background effects.) 54

ω_{4p} might look like, with $\xi(\mu_B)$ given by Eq. (2.17). We illustrate how ω_{4p} changes if we vary the location of the critical point μ_B^c and the width Δ of the peak in Fig. 2-1, as well as the sigma-proton coupling g_p. As we shall see in Section 2.2.1, there are four nonuniversal parameters that (for a given ξ_{max}) govern the height of the peaks of the normalized cumulants. These include g_p and the sigma-pion coupling G, as well as two parameters $\tilde{\lambda}_3$ and $\tilde{\lambda}_4$ that we shall define in Section 2.2.1. We have used as our benchmark values $G = 300$ MeV, $g = 7$, $\tilde{\lambda}_3 = 4$ and $\tilde{\lambda}_4 = 12$. As we shall discover in Section 2.2 and discuss at length in Section 2.3, the heights of the peaks of different normalized cumulants are affected differently by variations in these four parameters. Fig. 2-3 shows how six more different normalized cumulants vary with μ_B. In this Figure we keep all parameters set at their benchmark values, deferring a discussion of how these peaks change with parameters to Section 2.3.

In the case of free particles in the classical Boltzmann regime, with no critical fluctuations, the fluctuations of any particle number obey Poisson statistics. The Poisson contribution to ω_{ip} and $\omega_{i\pi}$ is 1, and in the Figures we have added this Poisson contribution to the contribution from critical flucuations that we calculate in Section 2.2. There is no Poisson contribution to the mixed cumulants $\omega_{ipj\pi}$. In reality, in the absence of any critical fluctuations the 1 of Poisson statistics gets few percent contributions from Bose-Einstein statistics, from initial state correlations that are incompletely washed out, and from interactions other than those with the fluctuations that are enhanced near the critical point. System size fluctuations are also a potential non-critical contribution to the fluctuation measures. We do not attempt to estimate this effect (see, e.g., Refs. [30], [113]), and assume that sufficiently tight centrality binning suppresses it. We are ignoring all of these non-critical corrections to the Poissonian 1 and in the plots shown here we only include the Poisson and critical contributions to the cumulants. Existing data on $\kappa_{4(p-\bar{p})}/\kappa_{2(p-\bar{p})}$ at $\sqrt{s} = 19.6$, 62.4 and 200 GeV [23] confirm that the non-critical corrections to the Poissonian 1 are indeed small, and confirm that it is possible to measure 4th order cumulants with an error bar that is much smaller than 1. At the time of writing this thesis, ratios of proton and pion cumulants are being analyzed by the STAR collaboration for energies

$\sqrt{s} = 7.7$, 11.5 GeV, but no results have been published yet.

We can clearly see the peak in all the normalized cumulants near the critical point. In many cases, the peak due to critical fluctuations is larger than the Poisson contribution by more than an order of magnitude.[2] The results indicate that the more protons are involved in the observation measure, the easier it is to identify the critical contribution. The reader who would like to see an example of a probability distribution that has ω_4 as large as ω_{4p} gets in Fig. 2-2 should consult Appendix A. A more comprehensive discussion of the results is given in Sections 2.3 and 2.4, but it is readily apparent that the measurement of these observables in heavy-ion collisions at a series of collision energies is very well suited to ruling out (or discovering) the presence of the QCD critical point in the vicinity of the freeze-out points of the collisions in such an energy scan.

2.2   Calculating Critical Correlators and Cumulants

In this Section, we show how to calculate the critical point contribution to the cumulants of the particle multiplicity distribution of pions, protons and net protons. We essentially show how to obtain the normalized cumulants in Figs. 2-2 and 2-3 as the location of the critical point, μ_B^c, changes. We begin in Section 2.2.1 by calculating the correlators that describe the critical contributions to the fluctuations of the occupation number of pions and protons with specified momenta. We use these correlators to calculate the normalized cumulants in Section 2.2.2.

2.2.1   Critical point contribution to correlators

Fluctuations of observables, such as particle multiplicities, are sensitive to the proximity of the critical point if the particles under consideration interact with the critical field σ — the field whose equilibrium correlation length diverges at the critical point. In this Section, we shall treat the σ correlation length ξ as a parameter, in this way

---

[2]Although it is a small effect, note that the peaks of any of the cumulants involving protons do not occur exactly at the μ_B^c at which $\xi(\mu_B)$ from Fig. 2-1 peaks, because the cumulants themselves depend directly on the proton number density and hence on μ_B, as we shall see in Section 2.2.

avoiding any consequences of our lack of knowledge of the dynamics of how the long wavelength correlations in the σ field grow. In order to use the results of this Section to make the plots in Section 2.1.3, in Section 2.1.2 we had to make an ansatz for $\xi(\mu_B)$. But, the results of this Section, expressed in terms of ξ, are independent of the uncertainties in that ansatz.

We can describe the fluctuations of the σ-field by a probability distribution of the form

$$P(\sigma) \sim \exp(-\Omega(\sigma)/T), \tag{2.20}$$

where Ω is the effective action functional for σ. It can be expanded in gradients and powers of σ as

$$\Omega(\sigma) = \int d^3x \left[\frac{1}{2}(\nabla\sigma)^2 + \frac{m_\sigma^2}{2}\sigma^2 + \frac{\lambda_3}{3}\sigma^3 + \frac{\lambda_4}{4}\sigma^4 + ... \right]. \tag{2.21}$$

In this expression the sigma-field screening mass is

$$m_\sigma \equiv \xi^{-1} \tag{2.22}$$

and, near the critical point, the σ^3 and σ^4 interaction couplings are given by

$$\lambda_3 = \widetilde{\lambda}_3 \, T \, (T\,\xi)^{-3/2}, \quad \text{and} \quad \lambda_4 = \widetilde{\lambda}_4 \, (T\,\xi)^{-1}, \tag{2.23}$$

where the dimensionless couplings $\widetilde{\lambda}_3$ and $\widetilde{\lambda}_4$ do not depend on ξ, but do depend on the *direction* of approach to the critical point, as described in Ref. [32]. These couplings (and their dependence on direction) are universal and they have been determined for the Ising universality class [114]. Throughout this Chapter we shall use $\widetilde{\lambda}_3 = 4$ and $\widetilde{\lambda}_4 = 12$ as benchmark values, because these are the midpoints of the ranges of values known for these constants [114, 32]. In fact, both $\widetilde{\lambda}_3$ and $\widetilde{\lambda}_4$ will vary with μ_B, as the location of the freeze-out point moves in the phase diagram, relative to the critical point. We shall not attempt to parametrize the μ_B-dependence of these parameters, however, because the dominant source of μ_B-dependence in our results is

the variation of ξ with μ_B, and our knowledge of $\xi(\mu_B)$ is sufficiently uncertain (as we saw in Section 2.1.2) that this uncertainty would dominate any increase in precision that would be obtained by modelling the μ_B-dependence of $\tilde{\lambda}_3$ and $\tilde{\lambda}_4$.

The correlation functions and fluctuation moments and cumulants of the critical field σ itself can be calculated directly using the probability distribution given in (2.20), but these quantities are not directly observable. The long wavelength fluctuations in the σ-field manifest themselves in observable quantities in so far as they affect the fluctuations of the occupation numbers of particles that couple to the σ-field. This coupling to the fluctuating field σ contributes to the moments of particle fluctuations the terms proportional to the corresponding moments of σ itself [32]. Both protons and pions couple to the σ field. We shall define the strengths of the corresponding couplings g_p and G through the respective terms of the effective Lagrangian (following the notations of [30, 112]):

$$\mathcal{L}_{\sigma\pi\pi,\sigma pp} = 2\,G\,\sigma\,\pi^+\pi^- + g_p\,\sigma\,\bar{p}\,p. \tag{2.24}$$

where $\pi^\pm$ is the (charged) pion field and p is the Dirac fermion field of the protons. The coupling that we denote g_p is often just called g. We shall make the discussion that follows similar for protons and pions by defining a dimensionless measure of the sigma-pion coupling

$$g_\pi \equiv G/m_\pi, \tag{2.25}$$

and using the notation g when we intend an equation to be valid for either pions, with $g \to g_\pi$, or protons, with $g \to g_p$. Throughout this Chapter we will use $G = 300$ MeV (see Ref. [30] for a discussion of how to estimate G) and $g_p = 7$ (see, e.g., [115]) as benchmark values. It is important to bear in mind that both these parameters and $\tilde{\lambda}_3$ and $\tilde{\lambda}_4$ are all uncertain at the factor of 2 level. These parameters enter into our calculations of the various normalized multiplicity cumulants, making absolute predictions of these observables in terms of ξ difficult. The advantage that we have, however, is that we will be able to calculate many different normalized cumulants that depend differently on these parameters. In Section 2.3 we shall discuss how

to use deliberately chosen ratios of cumulants to measure and even overconstrain various combinations of these parameters. And, we shall find five ratios of cumulants that are independent of the values of all of these parameters, allowing us to make parameter-free predictions of these ratios.

The critical contribution to the proton or pion correlators arises from virtual σ-exchanges which introduce powers of the correlation length $\xi = m_\sigma^{-1}$, where m_σ is the σ-field screening mass. As the correlation length grows in the vicinity of the critical point, the contribution to the particle correlators due to a σ-exchange dominates over other non-critical contributions. The effect of such an interaction on the two-point particle correlators was studied in Refs. [30, 107] and on higher-point correlators in Ref. [32]. In this Subsection we will only look at the particle correlators and in the subsequent Sections we will show how to calculate cumulants of particle multiplicity distributions from the correlators.

The contribution of critical fluctuations to the 2-, 3- and 4- particle correlators due to σ-exchanges can be calculated using the diagrammatic method developed in Ref. [107] (see also Refs. [30] and [32]). We shall write the correlators using a notation that applies to either protons or pions. They describe the correlation between the δn_k's at different momenta, where $\delta n_k \equiv n_k - \langle n_k \rangle$ is the difference between the occupation number of the k'th pion or proton mode in momentum space in a particular event and its mean value. The correlators are given by

$$\langle \delta n_{k_1} \delta n_{k_2} \rangle_\sigma = \frac{d^2}{m_\sigma^2 V} \frac{g^2}{T} \frac{v_{k_1}^2}{\gamma_{k_1}} \frac{v_{k_2}^2}{\gamma_{k_2}} = \frac{d^2}{VT} g^2 \xi^2 \frac{v_{k_1}^2}{\gamma_{k_1}} \frac{v_{k_2}^2}{\gamma_{k_2}} , \tag{2.26}$$

$$\langle \delta n_{k_1} \delta n_{k_2} \delta n_{k_3} \rangle_\sigma = \frac{2d^3 \lambda_3}{V^2 T} \left(\frac{g}{m_\sigma^2} \right)^3 \frac{v_{k_1}^2}{\gamma_{k_1}} \frac{v_{k_2}^2}{\gamma_{k_2}} \frac{v_{k_3}^2}{\gamma_{k_3}} = \frac{2d^3 \tilde{\lambda}_3}{V^2 T^{3/2}} g^3 \xi^{9/2} \frac{v_{k_1}^2}{\gamma_{k_1}} \frac{v_{k_2}^2}{\gamma_{k_2}} \frac{v_{k_3}^2}{\gamma_{k_3}}, \tag{2.27}$$

$$\begin{aligned} \langle \langle \delta n_{k_1} \delta n_{k_2} \delta n_{k_3} \delta n_{k_4} \rangle \rangle_\sigma &= \frac{6d^4}{V^3 T} \left(2 \left(\frac{\lambda_3}{m_\sigma} \right)^2 - \lambda_4 \right) \left(\frac{g}{m_\sigma^2} \right)^4 \frac{v_{k_1}^2}{\gamma_{k_1}} \frac{v_{k_2}^2}{\gamma_{k_2}} \frac{v_{k_3}^2}{\gamma_{k_3}} \frac{v_{k_4}^2}{\gamma_{k_4}} \\ &= \frac{6d^4}{V^3 T^2} \left(2\tilde{\lambda}_3^2 - \tilde{\lambda}_4 \right) g^4 \xi^7 \frac{v_{k_1}^2}{\gamma_{k_1}} \frac{v_{k_2}^2}{\gamma_{k_2}} \frac{v_{k_3}^2}{\gamma_{k_3}} \frac{v_{k_4}^2}{\gamma_{k_4}} , \tag{2.28} \end{aligned}$$

where we have used (2.22) and (2.23) and where we must now explain many aspects of our notation. The subscript σ indicates that we have only calculated the contribution of the critical fluctuations to the correlators. The double brackets around the quartic correlator indicate that what is evaluated is the cumulant, as in (2.4). The equations (2.26), (2.27), (2.28) apply to both protons (with $g = g_p$) and pions (with $g = g_\pi = G/m_\pi$). The degeneracy factor d is 2 for both protons and pions. (For protons, $d = d_p = 2$ counts the number of spin states. For pions, $d = d_\pi = 2$ counts the number of charge states — π^+ and π^-. These degeneracy factors appear because the coupling to the σ-field is both spin and charge "blind".) The variance of the fluctuating occupation number distribution is denoted by $v_{\boldsymbol{k}}^2$ and is given by

$$v_{\boldsymbol{k}}^2 = \langle n_{\boldsymbol{k}} \rangle \left(1 \pm \langle n_{\boldsymbol{k}} \rangle \right), \tag{2.29}$$

where, as usual,

$$\langle n_{\boldsymbol{k}} \rangle = \frac{1}{\exp\left[(\gamma_{\boldsymbol{k}} m - \mu)/T \right] \mp 1} \tag{2.30}$$

with $m = m_\pi$, $\mu = 0$ and the upper sign for pions and $m = m_p$, $\mu = \mu_B$ and the lower sign for protons. And, finally,

$$\gamma_{\boldsymbol{k}} \equiv \frac{\sqrt{\boldsymbol{k}^2 + m^2}}{m} \tag{2.31}$$

is the relativistic gamma-factor of the particle with mass m with a given momentum $\boldsymbol{k}$.[3] We see from Eqs. (2.26)-(2.28) that these correlators, and hence the cumulants that we will obtain from them, are proportional to powers of the correlation length ξ and so peak at the critical point.

Now let us turn to mixed pion-proton correlators. The 2 pion - 2 proton correlator

---

[3]A note on subscript/superscript notation: we denote momentum subscripts with a bold letter $\boldsymbol{k}$. Subscripts/superscripts denoting particle type, e.g. p for protons, will be in normal typeface.

is given by

$$\langle\langle \delta n_{k_1}^\pi \delta n_{k_2}^\pi \delta n_{k_3}^p \delta n_{k_4}^p \rangle\rangle_\sigma = \frac{6 d_\pi^2 d_p^2}{V^3 T} \left(2 \left(\frac{\lambda_3}{m_\sigma} \right)^2 - \lambda_4 \right) \left(\frac{g_\pi\, g_p}{m_\sigma^4} \right)^2 \frac{v_{k_1}^{\pi\,2}\, v_{k_2}^{\pi\,2}\, v_{k_3}^{p\,2}\, v_{k_4}^{p\,2}}{\gamma_{k_1}^\pi\, \gamma_{k_2}^\pi\, \gamma_{k_3}^p\, \gamma_{k_4}^p}$$

$$= \frac{6 d_\pi^2 d_p^2}{V^3 T^2} \left(2\tilde{\lambda}_3^2 - \tilde{\lambda}_4 \right) g_\pi^2 g_p^2 \xi^7 \frac{v_{k_1}^{\pi\,2}\, v_{k_2}^{\pi\,2}\, v_{k_3}^{p\,2}\, v_{k_4}^{p\,2}}{\gamma_{k_1}^\pi\, \gamma_{k_2}^\pi\, \gamma_{k_3}^p\, \gamma_{k_4}^p}. \tag{2.32}$$

The prescription for obtaining other mixed correlators from the correlators (2.26 - 2.28) should be clear: each particle brings its own corresponding factor $d\, g\, v_k^2/\gamma_k$ to the expression in, e.g., Eq. (2.28). In this way, the 1 pion - 3 proton and 3 pion - 1 proton mixed correlators can be obtained from Eq. (2.28), the 1 pion - 2 proton and 2 pion - 1 proton mixed correlators can be obtained from Eq. (2.27), and the 1 pion - 1 proton can be obtained from Eq. (2.26).

Another useful fluctuating quantity to consider is the *net* proton number correlators (the net proton number is defined as the number of protons minus the number of anti-protons: $N_{p-\bar{p}} = N_p - N_{\bar{p}}$). In order to obtain the corresponding correlators one can begin with the similar correlators for the protons and replace $v_k^{p\,2}$ with $(v_k^{p\,2} - v_k^{\bar{p}\,2})$, where $v_k^{\bar{p}\,2}$ is the occupation number variance for anti-protons. (See, e.g., Ref. [112]).

In the next Section we will use these correlators to evaluate cumulants of particle multiplicity distributions for pions, protons and net protons and see how they can be used to locate the critical point.

2.2.2 Energy dependence of pion, proton, net proton, and mixed pion/proton multiplicity cumulants

In this Section we will concentrate on cumulants of the particle multiplicity distributions and how they vary as we change the location of the critical point and change the value of parameters. Another application of the correlators given in the previous Section is the calculation of the critical point effect on higher moments of the fluctuation of mean transverse momentum p_T. We find that the critical contribution to p_T fluctuations is rather small (e.g., smaller than the enhancement due to Bose statistics) and thus not as useful in the search of the critical point. Details can be

found in Appendix B.

Now let us focus on how one can obtain higher cumulants of the particle multiplicity distributions using the correlators found in the previous Section. As an example, let us evaluate the critical contribution to the normalized fourth cumulant of the proton multiplicity distribution, ω_{4p} defined in (2.13). The total multiplicity N_p is just the sum of all occupation numbers n_k, thus (see ref. [32])

$$\kappa_{4p,\sigma} = \langle\langle(\delta N_p)^4\rangle\rangle_\sigma = V^4 \int_{k_1}\int_{k_2}\int_{k_3}\int_{k_4} \langle\langle\delta n^p_{k_1}\delta n^p_{k_2}\delta n^p_{k_3}\delta n^p_{k_4}\rangle\rangle_\sigma \ , \tag{2.33}$$

where

$$\int_k \equiv \int \frac{d^3k}{(2\pi)^3}. \tag{2.34}$$

As we discussed in Section 2.1.1, see (2.13), we normalize the cumulant by dividing by the total proton multiplicity N_p. To simplify notation below, it is convenient to introduce the proton and pion number densities

$$n_p \equiv \frac{\langle N_p\rangle}{V} \; = \; d_p \int_k \langle n^p_k\rangle = \frac{1}{\pi^2}\int_{m_p}^\infty \frac{dE\, E\sqrt{E^2 - m_p^2}}{e^{(E-\mu_B)/T} + 1} \tag{2.35}$$

$$n_\pi \equiv \frac{\langle N_\pi\rangle}{V} \; = \; d_\pi \int_k \langle n^\pi_k\rangle = \frac{1}{\pi^2}\int_{m_\pi}^\infty \frac{dE\, E\sqrt{E^2 - m_\pi^2}}{e^{E/T} - 1} \ . \tag{2.36}$$

The result we find for the normalized cumulant can then be written as

$$\omega_{4p,\,\sigma} = \frac{6\,(2\tilde\lambda_3^2 - \tilde\lambda_4)}{T^2 n_p}\, \xi^7 \left(d_p\, g_p \int_k \frac{v_k^{p\,2}}{\gamma_k^p}\right)^4 \ . \tag{2.37}$$

We can see from expressions (2.26) - (2.28) that higher cumulants are proportional to higher powers of ξ and thus increase by a larger factor near the critical point where ξ becomes large. For example, the third and fourth cumulants are proportional to $\xi^{9/2}$ and ξ^7, respectively. If the correlation length ξ increases from ~ 0.5 fm to $\xi_{\text{max}} = 2$ fm as in Section 2.1.2, these cumulants are substantially enhanced — as we have seen in the plots in Section 2.1.3.

With an explicit expression for $\omega_{4p,\sigma}$ in hand, we can now write our general result for $\omega_{ipj\pi,\sigma}$ in (2.15). We can also include $\omega_{ip,\sigma}$ and $\omega_{j\pi,\sigma}$ defined as in (2.13) and (2.12)

in the notation via setting $j = 0$ or $i = 0$ in $\omega_{ipj\pi,\sigma}$. We obtain

$$
\begin{aligned}
\omega_{ipj\pi} &= \delta_{i,0} + \delta_{j,0} + \frac{\tilde{\lambda}'_r (r-1)!}{T^{r/2}} \frac{\alpha_p^i}{n_p^{i/r}} \frac{\alpha_\pi^j}{n_\pi^{j/r}} \xi^{\frac{5}{2}r-3} \\
&= \delta_{i,0} + \delta_{j,0} + \omega_{ipj\pi}^{\text{prefactor}} \left(\frac{n_p}{n_0}\right)^{i-\frac{i}{r}} \left(\frac{\xi}{\xi_{\max}}\right)^{\frac{5}{2}r-3} ,
\end{aligned}
\tag{2.38}
$$

where we have defined

$$
\omega_{ipj\pi}^{\text{prefactor}} \equiv \frac{\tilde{\lambda}'_r (r-1)! \, \xi_{\max}^{\frac{5}{2}r-3}}{T^{r/2}} \frac{\alpha_p^i}{n_p^{i/r}} \frac{\alpha_\pi^j}{n_\pi^{j/r}} \left(\frac{n_0}{n_p}\right)^{i-\frac{i}{r}}
\tag{2.39}
$$

and

$$
\alpha_\pi \equiv d_\pi \, g_\pi \int_{\boldsymbol{k}} \frac{v_{\boldsymbol{k}}^{\pi\,2}}{\gamma_{\boldsymbol{k}}^\pi}, \quad \alpha_p \equiv d_p \, g_p \int_{\boldsymbol{k}} \frac{v_{\boldsymbol{k}}^{p\,2}}{\gamma_{\boldsymbol{k}}^p},
\tag{2.40}
$$

$$
\tilde{\lambda}'_2 \equiv 1, \quad \tilde{\lambda}'_3 \equiv \tilde{\lambda}_3 \quad \text{and} \quad \tilde{\lambda}'_4 \equiv 2\tilde{\lambda}_3^2 - \tilde{\lambda}_4.
\tag{2.41}
$$

In the second line of (2.38) we have factored out the two main sources of μ_B dependence: the correlation length ξ depends on μ_B as we have discussed at length in Section 2.1.2 and, if the normalized cumulant involves the proton multiplicity it depends on n_p, which increases rapidly with increasing μ_B as shown in Fig. 2-4. We have denoted all of the remaining factors in our result for the contribution of critical fluctuations to the normalized cumulant by $\omega_{ipj\pi}^{\text{prefactor}}$, which depends only weakly on μ_B as we illustrate in Fig. 2-5. The number density n_0 is an arbitrary constant — note that it cancels when (2.39) is substituted into (2.38) — introduced in order to make $\omega_{ipj\pi}^{\text{prefactor}}$ dimensionless. We shall choose

$$
n_0 \equiv \frac{1}{(5\,\text{fm})^3} = 6.116 \times 10^{-5} \text{ GeV}^3 .
\tag{2.42}
$$

With this choice, $\langle n_p \rangle / n_0$ is of order 1 at the μ_B of interest to us — see Fig. 2-4 — and none of the different $\omega_{ipj\pi}^{\text{prefactor}}$s are orders of magnitude smaller or larger than 1, as illustrated in Fig. 2-5.

Let us now walk through the physics behind the different pieces of the expression
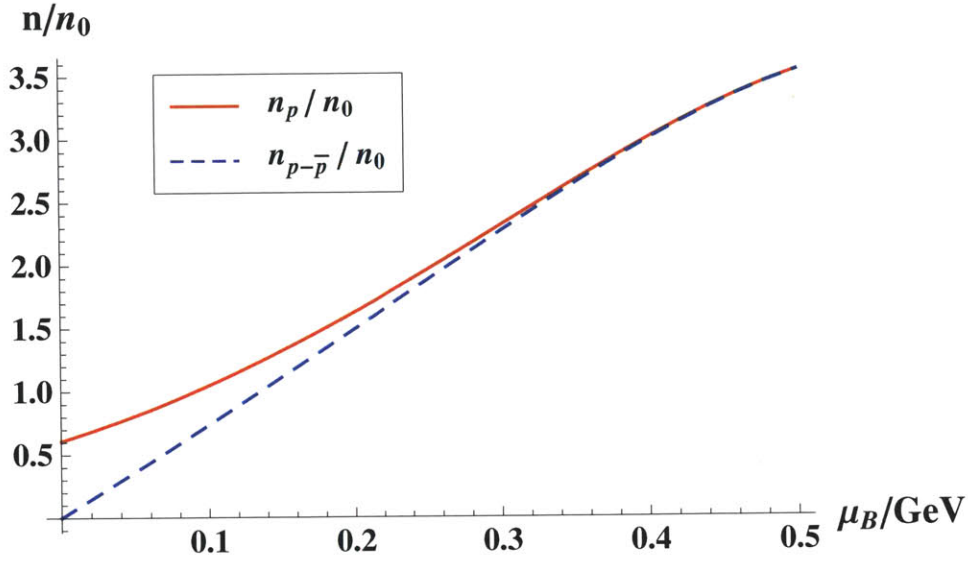
Figure 2-4: Proton number density n_p and net proton number density $n_{p-\bar{p}} \equiv n_p - n_{\bar{p}}$ at chemical freezeout as functions of μ_B. Both depend on T as well as μ_B; we have taken $T(\mu_B)$ as in (2.43). We have normalized both n_p and $n_{p-\bar{p}}$ using the constant n_0 of (2.42) introduced in (2.38) and (2.39).

(2.38). The Kronecker deltas describe Poisson fluctuations, which are of course ξ-independent. As we described in Section 2.1.1, they contribute 1 to the ω_{ip}'s and the $\omega_{j\pi}$'s and they make no contribution to the mixed cumulants in which i and j are both nonzero. More realistically, the 1 of Poisson statistics gets few percent contributions from Bose-Einstein statistics (which are calculable), from initial state correlations that are incompletely washed out, and from interactions other than those with the critical σ-mode. We are ignoring all of these noncritical corrections to the 1. In principle, with sufficiently precise data their magnitude could be measured far away from the critical point and this background could then be subtracted. If this background were significant, one could also try to study and calculate these corrections theoretically. Present data on $\kappa_{4(p-\bar{p})}/\kappa_{2(p-\bar{p})}$ at $\sqrt{s} = 19.6$, 62.4 and 200 GeV indicate that the corrections to the Poissonian 1 are quite small, but this should be investigated also for other cumulants.

The second, ξ-dependent, term in (2.38) is the contribution to $\omega_{ipj\pi}$ made by the critical fluctuations. It grows proportional to $\xi^{(5r-6)/2}$ near the critical point. We

64
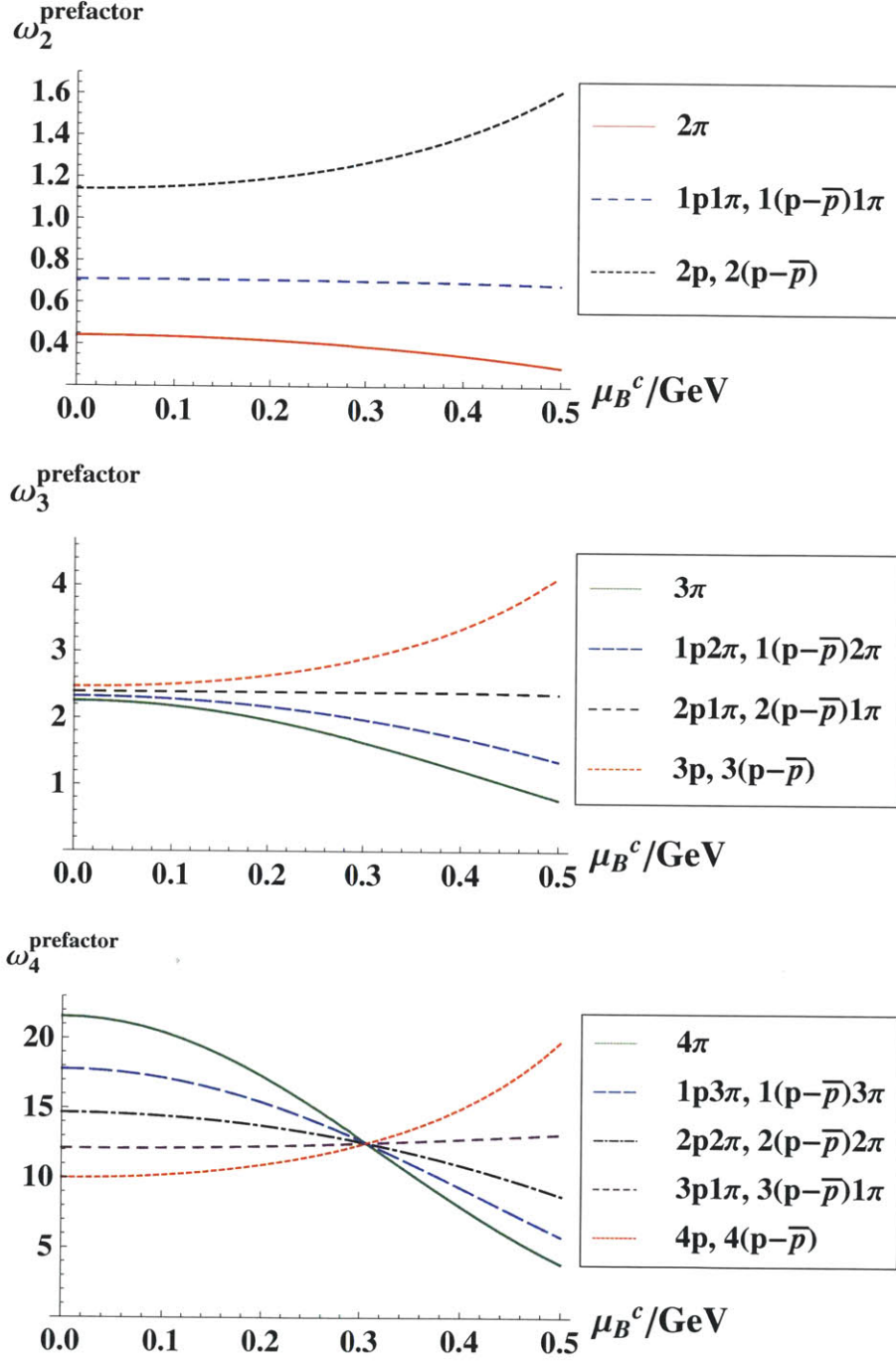
Figure 2-5: The μ_B-dependence of $\omega_{ipj\pi}^{\text{prefactor}}$ and $\omega_{i(p-\bar{p})j\pi}^{\text{prefactor}}$, defined in (2.38), (2.39) and (2.44). The three panels are for the normalized cumulants with $r \equiv i + j = 2, 3$ and 4, respectively. The curves can be used to determine how the height of the peak in the critical contribution to the normalized cumulants changes as we vary μ_B^c, the μ_B at which $\xi = \xi_{\max}$ and at which (to a very good approximation) the normalized cumulant has its peak. The height of the peak in $\omega_{ipj\pi}$ [or $\omega_{i(p-\bar{p})j\pi}$] is proportional to $(n_p/n_0)^{i-i/r}$ [or $(n_{p-\bar{p}}/n_0)^{i-i/r}$] multiplied by the prefactor plotted in this Figure. We have taken $T(\mu_B)$ as in (2.43) and have used the benchmark parameters $G = 300$ MeV, $g_p = 7$, $\tilde{\lambda}_3 = 4$ and $\tilde{\lambda}_4 = 12$.

see evidence of this in the heights of the peaks in different ω's in Fig. 2-3, but it is also clear from this Figure that the r-dependent difference in the power of ξ is not the only important source of μ-dependence. Indeed, we see in (2.39) that $\omega_{ipj\pi}^{\mathrm{prefact}}$ is proportional to $n_p^{-i/r}$ and to α_p^i and, it turns out, α_p/n_p is close to constant. This means that the dominant μ_B-dependence of the critical contribution to $\omega_{ipj\pi}$ at a given ξ is $n_p^{i-i/r}$, which we have factored out in (2.38) making the μ_B-dependence in $\omega_{ipj\pi}^{\mathrm{prefact}}$ rather mild. We can see the $n_p^{i-i/r} = n_p^3$ dependence of the height of the peak in ω_{4p} in the lower panel of Fig. 2-2: in this Figure ξ_{max} is the same for all the curves so the μ_B-dependence of the height of the peaks in ω_{4p} comes from its n_p-dependence.

For $i = 0$, meaning for a cumulant involving pions only, there is no large n_p-dependence in $\omega_{j\pi}$ and the height of the peak in a figure like Fig. 2-3 is proportional to $\omega_{j\pi}^{\mathrm{prefactor}}$, and the dominant μ_B-dependence of $\omega_{j\pi}$ itself comes from its ξ^{j-1} dependence. For observables involving protons ($i > 0$), the dominant contribution to the μ_B^c dependence of the height of the peak in ω comes from the factor $n_p^{i-i/r}$, and the slowly varying prefactor in Fig. 2-5 adds relatively little to that strong dependence.

In plotting the curves in Fig. 2-4 and Fig. 2-5, we have allowed for the fact that the chemical freeze-out temperature T decreases somewhat with increasing μ_B. We have described this dependence using an empirical parametrization of heavy-ion collision data from Ref. [26]:

$$T(\mu_B) = a - b\mu_B^2 - c\mu_B^4, \tag{2.43}$$

with $a = 0.166$ GeV, $b = 0.139$ GeV^{-1} and $c = 0.053$ GeV^{-3}. Almost all of the μ_B-dependence of the $\omega_{ipj\pi}^{\mathrm{prefactor}}$s plotted in Fig. 2-5 actually comes from the μ_B-dependence of the chemical freeze-out temperature T. In plotting Fig. 2-5, we have used our benchmark values of the four nonuniversal parameters that determine the $\omega_{ipj\pi}$ for a given ξ, namely $g_\pi = G/m_\pi = 2.1$, $g_p = 7$, $\widetilde{\lambda}_3 = 4$ and $\widetilde{\lambda}_4 = 12$.

Finally, completing our discussion of the proton-pion cumulants and Fig. 2-5, we note that in the lower panel in this figure there is a point where all five $\omega_{ipj\pi}^{\mathrm{prefactor}}$s with $r = 4$ cross. This occurs if at some value of μ_B it so happens that $\alpha_\pi(n_0/n_\pi)^{1/r}$ and $\alpha_p n_0/n_p$ coincide.

We now turn to the net proton multiplicity distribution, where by net protons we mean $N_{p-\bar{p}} \equiv N_p - N_{\bar{p}}$. The calculation of the normalized cumulants involving the net proton multiplicity and the pion multiplicity, namely (2.16), is analogous to the calculation we have described above. As we discussed in Section 2.2.1, the only change in the correlator from which the cumulants are obtained is the replacement of $v_k^{p\,2}$ with $v_k^{p\,2} - v_k^{\bar{p}\,2}$. We find

$$\omega_{i(p-\bar{p})j\pi} = \delta_{i,0} + \delta_{j,0} + \omega_{i(p-\bar{p})j\pi}^{\text{prefactor}} \left(\frac{n_{p-\bar{p}}}{n_0}\right)^{i-\frac{i}{r}} \left(\frac{n_{p-\bar{p}}}{n_p + n_{\bar{p}}}\right)^{\frac{i}{r}} \left(\frac{\xi}{\xi_{\max}}\right)^{\frac{5}{2}r-3}, \quad (2.44)$$

where $n_{p-\bar{p}} = n_p - n_{\bar{p}}$ is the net proton number density. In comparison with Eq. (2.38), we have pulled out another factor, $\left(\frac{n_{p-\bar{p}}}{n_p+n_{\bar{p}}}\right)^{\frac{i}{r}}$, which describes the vanishing of the critical contribution to net proton cumulants at $\mu_B = 0$, see Fig. 2-4. It then turns out that the prefactor $\omega_{i(p-\bar{p})j\pi}^{\text{prefactor}}$ (defined as in (2.39), but multiplied by $\left(\frac{n_p+n_{\bar{p}}}{n_{p-\bar{p}}}\right)^{\frac{i}{r}}$ and with $v_k^{p\,2}$ replaced by $v_k^{p\,2} - v_k^{\bar{p}\,2}$) differs from $\omega_{ipj\pi}^{\text{prefactor}}$ by less than half of one percent, which is less than the thickness of the curves in Fig. 2-5. Hence, these curves also depict $\omega_{i(p-\bar{p})j\pi}^{\text{prefactor}}$.

In order to evaluate either (2.38) [or (2.44)] and compare to data, we need the proton number density n_p [net proton number density $n_{p-\bar{p}}$] at each collision energy $\sqrt{s}$. These can be extracted from data via the conventional statistical model fits done at each $\sqrt{s}$ that give μ_B and T at chemical freeze-out at each $\sqrt{s}$. The value of n_p at chemical freeze-out is specified in terms of μ_B and T by (2.35) and the value of $n_{\bar{p}}$ is given by the same expression with μ_B replaced by $-\mu_B$, so these number densities can also be obtained from data. So, at each collision energy, one should take the μ_B and T from the statistical model fit, evaluate n_p and $n_{p-\bar{p}}$, and then plug these into (2.38) and (2.44) and see what conclusions can be drawn about ξ and the constants g_p, g_π, $\tilde{\lambda}_3$ and $\tilde{\lambda}_4$ using data on as many of the normalized cumulants $\omega_{ipj\pi}$ and $\omega_{i(p-\bar{p})j\pi}$ as possible. We shall provide tuned strategies for this analysis in Section 2.3. We close this Section with two straightforward observations.

First, the proton/pion normalized cumulant $\omega_{ipj\pi}$ is more sensitive to critical fluctuations than the net-proton/pion normalized cumulant $\omega_{i(p-\bar{p})j\pi}$, for any $i \neq 0$ and

for any j. As an example let us consider ω_{4p} and $\omega_{4(p-\bar{p})}$. We can estimate $\mu_B(\sqrt{s})$ using the parametrization of statistical model fits to data in Ref. [26]:

$$\mu_B(\sqrt{s}) = \frac{d}{1 + e\sqrt{s}}, \tag{2.45}$$

with $d = 1.308$ GeV and $e = 0.273$ GeV^{-1}. The proton number density $n_p(\mu_B)$ is then shown in Fig. 2-4. Then, at any fixed value of the correlation length ξ the n_p-dependence that enters the expressions (2.38) and (2.44) for ω_{4p} and $\omega_{4(p-\bar{p})}$ is

$$\left(\frac{n_p}{n_0}\right)^3 = 0.34, \ 0.77, \ 4.9, \ 31 \tag{2.46}$$

and

$$\left(\frac{n_{p-\bar{p}}}{n_0}\right)^3 \left(\frac{n_{p-\bar{p}}}{n_p + n_{\bar{p}}}\right) = 0.00072, \ 0.064, \ 3.4, \ 30, \tag{2.47}$$

respectively, when evaluated at $\sqrt{s} = 200, 62, 19$ and 7.7 GeV. Since $n_{p-\bar{p}}$ is less than n_p (and consequently less than $n_p + n_{\bar{p}}$) at all μ_B — see Fig. 2-4 — the critical contribution to ω_{4p} is greater than the critical contribution to $\omega_{4(p-\bar{p})}$ at all μ_B. The analogous argument applies in comparing any $\omega_{i(p-\bar{p})j\pi}$ to the corresponding $\omega_{ipj\pi}$. In all cases the suppression of the critical contribution to $\omega_{i(p-\bar{p})}$ is most accute at small μ_B, meaning at large $\sqrt{s}$. We shall ignore $\omega_{i(p-\bar{p})j\pi}$ in Section 2.3.

Second, we can ask which observable is most sensitive to critical fluctuations. For a given ξ, the critical contribution to $\omega_{ipj\pi}$ is largest when r is largest, since as we see from (2.38) this gives ω the strongest ξ-dependence. The experimental measurements reported in Ref. [23] demonstrate that $\kappa_{4(p-\bar{p})}/\kappa_{2(p-\bar{p})}$ can be measured with error bars that are much smaller than 1, and we expect that ω_{4p} and $\omega_{4\pi}$ can be measured with comparably small error bars. The error bars on measurements of cumulants with $r > 4$ will be larger, so until experimentalists demonstrate that they can be measured we have focussed on cumulants with $r \leq 4$. For a given ξ and r, the critical contribution to $\omega_{ipj\pi}$ is largest for $i = r$ if $\alpha_p^r/n_p > \alpha_\pi^r/n_\pi$ or for $i = 0$ if $\alpha_p^r/n_p < \alpha_\pi^r/n_\pi$.

It is apparent from Figs. 2-2 and 2-3 that $\omega_{4p} \gg \omega_{4\pi}$ at $\mu_B^c = 400$ MeV with our

benchmark values of g_p and g_π, meaning that ω_{4p} is the normalized cumulant with $r = 4$ that is most sensitive to critical fluctuations. And, it is sensitive indeed: we see from the plots in Fig. 2-2 that if ξ reaches 2 fm, the critical contribution to ω_{4p} will be dramatic. Correspondingly, if for example experimental measurements were to show that $\omega_{4p} - 1 < 1$ at some μ_B around 400 MeV, then $\xi < 1$ fm at that μ_B. However, if μ_B^c is much less than 400 MeV and/or if g_p/g_π is much smaller than with our benchmark values, then α_p^r/n_p could become less than α_π^r/n_π, making $\omega_{4\pi}$ the best observable with which to find evidence for the presence of critical fluctuations. (With g_p and g_π set to their benchmark values, $\alpha_p^4/n_p = \alpha_\pi^4/n_\pi$ at $\mu_B \simeq 135$ MeV.) Both ω_{4p} and $\omega_{4\pi}$ should be measured, and we shall see in Section 2.3 that if critical fluctuations are discovered it will be very important to have data on as many of the $\omega_{ipj\pi}$ as possible.

2.3 Ratios of cumulants

In the previous Section, we presented numerical results for the contribution made by critical fluctuations to various cumulants of particle multiplicity distributions. In order to locate the critical point, experimental results on multiplicity cumulants will need to be compared to the theoretical predictions of the critical contribution to these cumulants. But, recall that we had to choose benchmark values for four parameters: g_p, g_π, $\widetilde{\lambda}_3$ and $\widetilde{\lambda}_4$. These parameters are not known reliably or accurately enough to permit a quantitative prediction for the effect of the critical point on any one of the cumulants we have described. The normalized cumulants depend on ξ, of course, but their dependence on the four poorly known parameters would make it difficult to determine ξ from data on any one of the cumulants, in isolation. In this Section, we suppose that at some $\sqrt{s}$ there is experimental data showing several of the cumulants significantly exceeding their Poisson values. We ask how ratios of cumulants can be used to extract information on ξ and the values of the four parameters. And, we construct ratios of cumulants that are independent of ξ and all the parameters, allowing us to make robust predictions for the contribution of critical fluctuations to

69

these ratios.

The contributions of critical fluctuations to different correlators depend on different combinations of ξ and the four parameters. For example,

$$
\begin{aligned}
\kappa_{2p,\sigma} &\sim V n_p^2 g_p^2 \xi^2, \\
\kappa_{3p,\sigma} &\sim V n_p^3 g_p^3 \tilde{\lambda}_3 \xi^{9/2}, \\
\kappa_{4p,\sigma} &\sim V n_p^4 g_p^4 \tilde{\lambda}_4' \xi^7,
\end{aligned}
\tag{2.48}
$$

where $\tilde{\lambda}_4' \equiv 2\tilde{\lambda}_3^2 - \tilde{\lambda}_4$. For the most general pion-proton cumulant,

$$
\kappa_{ipj\pi,\sigma} \sim V n_p^i g_p^i g_\pi^j \tilde{\lambda}_r' \xi^{\frac{5}{2}r-3} ,
\tag{2.49}
$$

with $r = i + j$ and with $\tilde{\lambda}_r'$ as defined in (2.41). We have kept the n_p-dependence since it introduces significant μ_B-dependence, but we have suppressed the T- and n_π-dependence. In Table 2.1 we present the parameter dependence of various cumulant ratios. Except for the first 3 entries, N_π, N_p and $\kappa_{ipj\pi}$, the quantities we consider are all V-independent (i.e. intensive) by construction. (In constructing intensive ratios, we can always remove V-dependence by dividing by N_π to the appropriate power.) Note that although we have not written the σ subscripts in the Table, the Table only describes the parameter-dependence of the contributions from critical fluctuations. When the ratios in the Table are constructed from data, the Poisson contribution must be subtracted from each measured κ separately, before taking a ratio. This means that this Table will only be useful in the analysis of data at values of $\sqrt{s}$ at which several κ's are different from their Poisson values by amounts large compared to the experimental statistical and systematic error bars.

Looking at Table 2.1, one can see how to use cumulant ratios in order to constrain ξ and the four parameters. The correlation length ξ and the four nonuniversal parameters always appear in certain combinations in the multiplicity cumulants and it turns out that we can only constrain four independent combinations. We have constructed the Table to highlight ratios that can be used to constrain one example of four such

70

Table 2.1: Parameter dependence of the contribution of critical fluctuations to various particle multiplicity cumulant ratios. We have subtracted the Poisson contribution from each cumulant before taking the ratio. The Table shows the power at which the parameters enter in each case. We only considered cases with $r \equiv i+j = 2,\,3,\,4$. We defined $2\tilde\lambda_3^2 - \tilde\lambda_4 \equiv \tilde\lambda'_4$.

ratio	V	$n_p(\mu_B)$	g_p	g_π	$\tilde\lambda_3$	$\tilde\lambda'_4$	ξ
N_π	1	-	-	-	-	-	-
N_p	1	1	-	-	-	-	-
$\kappa_{ipj\pi}$	1	i	i	j	$\delta_{r,3}$	$\delta_{r,4}$	$\frac{5}{2}r - 3$
$\omega_{ipj\pi}$	-	$i - \frac{i}{r}$	i	j	$\delta_{r,3}$	$\delta_{r,4}$	$\frac{5}{2}r - 3$
$\kappa_{ipj\pi}N_\pi^{i-1}/N_p^i$	-	-	i	j	$\delta_{r,3}$	$\delta_{r,4}$	$\frac{5}{2}r - 3$
$\kappa_{2p2\pi}N_\pi/\kappa_{4\pi}\kappa_{2p}$	-	-	-	-2	-	-	-2
$\kappa_{4p}N_\pi^2/\kappa_{4\pi}\kappa_{2p}^2$	-	-	-	-4	-	-	-4
$\kappa_{2p2\pi}N_p^2/\kappa_{4p}N_\pi^2$	-	-	-2	2	-	-	-
$\kappa_{3p1\pi}N_p/\kappa_{4p}N_\pi$	-	-	-1	1	-	-	-
$\kappa_{3p}N_p^{3/2}/\kappa_{2p}^{9/4}N_\pi^{1/4}$	-	-	$-3/2$	-	1	-	-
$\kappa_{2p}\kappa_{4p}/\kappa_{3p}^2$	-	-	-	-	-2	1	-
$\kappa_{3p}\kappa_{2\pi}^{3/2}/\kappa_{3\pi}\kappa_{2p}^{3/2}$	-	-	-	-	-	-	-
$\kappa_{4p}\kappa_{2\pi}^2/\kappa_{4\pi}\kappa_{2p}^2$	-	-	-	-	-	-	-
$\kappa_{4p}^3\kappa_{3\pi}^4/\kappa_{4\pi}^3\kappa_{3p}^4$	-	-	-	-	-	-	-
$\kappa_{2p2\pi}^2/\kappa_{4\pi}\kappa_{4p}$	-	-	-	-	-	-	-
$\kappa_{2p1\pi}^3/\kappa_{3p}^2\kappa_{3\pi}$	-	-	-	-	-	-	-

combinations, with each block delineated by double horizontal lines corresponding to constraining

1. $g_\pi \xi$ — using, e.g., $\kappa_{2p2\pi} N_\pi / \kappa_{4\pi} \kappa_{2p}$ or $\kappa_{4p} N_\pi^2 / \kappa_{4\pi} \kappa_{2p}^2$.[4]

2. g_π / g_p — using, e.g., $\kappa_{2p2\pi} N_p^2 / \kappa_{4p} N_\pi^2$ or $\kappa_{3p1\pi} N_p / \kappa_{4p} N_\pi$.

3. $\tilde{\lambda}_3^2 / g_p^3$ — using, e.g., $\kappa_{3p} N_p^{3/2} / \kappa_{2p}^{9/4} N_\pi^{1/4}$.

4. $\tilde{\lambda}_4' / \tilde{\lambda}_3^2$ — using, e.g., $\kappa_{2p} \kappa_{4p} / \kappa_{3p}^2$.

Since four independent combinations of ξ and the four parameters can be constrained by data on these ratios, we could, for example, use data to express ξ and three of the parameters in terms of the fourth, say g_p.

We can see from Table 2.1 that there are also some combinations (e.g., the last five entries in the Table) that are parameter-independent. The first two of these are in fact the ratios of the skewness and kurtosis of protons to pions, where skewness and kurtosis are defined as usual as

$$\text{skewness} = \frac{\kappa_3}{\kappa_2^{3/2}}, \quad \text{kurtosis} = \frac{\kappa_4}{\kappa_2^2}. \tag{2.50}$$

The next row in the Table is the ratio of the two rows above it, giving a combination that has the virtue that it only involves 3rd and 4th cumulants, which is advantageous since the contribution of the critical fluctuations is larger at larger r. The last two ratios in the Table are quite different, as they involve mixed cumulants, but they too are parameter-independent. So, the last five ratios in the Table have no ξ-dependence, no dependence on the four poorly known parameters, and no n_p-dependence. This means that, after we subtract the Poisson contribution to each of the cumulants involved, we can make a robust prediction for the ratios of the contributions of critical fluctuations. We find that these five ratios are all precisely 1.

---

[4]The ratio $\omega_{2\pi} = \kappa_{2\pi} / N_\pi$ could also be used here. However, we have seen that the critical contribution to this quantity is small and, given the multitude of alternative choices, we can afford not to use this quadratic moment.

Now let us see how we can use these five ratios in order to locate the critical point. Suppose that as you change the center of mass energy $\sqrt{s}$ of the collisions there is a point where many cumulants exceed their Poisson values by statistically significant amounts. As we see from Figs. 2-2 and 2-3, the qualitative signature of the critical point is peaks in the multiplicity cumulants as a function of $\sqrt{s}$. Suppose experimental evidence for such peaks begins to emerge. The specific ratios of the heights of the peaks in Figs. 2-2 and 2-3 depended on the benchmark choices for parameters that we made in those Figures. So, how do you check in a parameter-independent fashion whether the behavior seen in experimental data is consistent with the hypothesis that it is due to critical fluctuations? You first subtract the Poisson contributions,[5] and then construct the last five ratios in Table 2.1. If the fluctuations seen in this hypothetical data are in fact due to the proximity of the critical point, all five of these ratios will be equal to 1, with no theoretical uncertainties arising from uncertainty in the values of the parameters. This would be strong evidence indeed for the discovery of the QCD critical point.

2.4   Discussion

We have explored the effects of the long wavelength fluctuations that arise in heavy-ion collisions that freezeout near the QCD critical point on higher cumulants of particle multiplicities. The characteristic signature is the non-monotonic behavior of such observables as a function of the collision energy, as the freezeout point approaches and then passes the critical point in the QCD phase diagram. In Section 2.1 we illustrated one possibility for how seven different cumulants (third and fourth cumulants of protons and pions plus three mixed cumulants) might behave as a function of μ_B, the chemical potential at freeze-out which is the quantity that a beam energy

---

[5]This can be done by subtracting the values of the cumulants in a sample of "mixed events," i.e. events constructed artificially from tracks drawn at random from many different events in order to remove all correlations. In this way, in addition to subtracting Poisson fluctuations one will also subtract spurious experimental effects. The mixed event technique is widely used in the study of quadratic moments and it could be used here too, even though present data indicate that spurious experimental effects are quite small [23].

scan scans. In Section 2.2, after calculating 21 different cumulants as a function of parameters and as a function of the correlation length ξ at freezeout, we determined that either ω_{4p} or $\omega_{4\pi}$ is the most sensitive to critical fluctuations, depending on the values of parameters and depending on the location of the critical point. However, if critical fluctuations are discovered it will be important to have measured as many of the cumulant observables as possible. In Section 2.3 we constructed ratios of observables that will allow an overconstrained experimental determination of currently poorly known parameters. And, we constructed other ratios of observables that, if the measured cumulants are indeed dominated by critical fluctuations, are independent of all the parameters in our calculation and are independent of the value of the correlation length. We are therefore able to make parameter-independent predictions for these ratios, predictions that we hope will some day make it possible to determine with confidence that observed fluctuations do indeed indicate proximity to the critical point.

There are several effects that require further investigation:

- In our treatment of the pions we have assumed that all pions seen in the detector reflect the physics at the time of freezeout, but it is thought that roughly half of the detected pions come from the later decay of resonances [30]. Let us look at how this affects our results. Consider the peaks in Figs. 2-2 and 2-3, in the vicinity of μ_B^c where freeze-out occurs closest to the critical point. Because the cumulants (for example $\kappa_{4\pi}$) are extensive, our calculation of the normalized cumulants (for example $\omega_{4\pi} = \kappa_{4\pi}/\langle N_\pi \rangle$) would be correct if the experimentalists measuring $\omega_{4\pi}$ divide by the number of pions present at freezeout. By dividing instead by the number of pions seen in the detector, the experimentalists will obtain a smaller $\omega_{4\pi}$ than in our calculation. This is an effect that can be corrected for.

- There are physical effects that can limit the upward fluctuation of N_p. For example, if the proton number density becomes too large, it will not be a good approximation to treat the protons at the time of chemical freezeout as noninter-

acting. In Appendix A we make a crude attempt to estimate the consequences of including such effects on the normalized cumulants. It will be much easier to model the consequences of this effect with data that show evidence for critical fluctuations in hand, since such data itself will indicate whether upward fluctuations in N_p are cutoff, and if so at what N_p.

- The fact that net baryon number is conserved will also limit the fluctuation in N_p. The magnitude of this effect depends on the size of the acceptance window, and for noncritical (and Gaussian) fluctuations has been studied in Refs. [116, 117, 118, 119, 17]). It also depends on the features of baryon number fluctuations *outside* the acceptance window. It may translate into a sharp cutoff on the upward fluctuation of N_p (as, e.g., proposed in a model study in Ref. [120]) or the reduction in flucutations may be more smoothly distributed over a range of N_p. We defer investigation of this effect to future work. Experimentalists will also be able to learn more about this and other effects by studying the dependence of the normalized proton cumulants on the width of the rapidity acceptance window, once there is data showing evidence of critical fluctuations.

- We have focussed on fourth and lower order cumulants. Our results show, though, that higher order cumulants depend on even higher powers of the correlation length ξ, making them even more sensitive to the proximity of the critical point. However, the measurement of higher order cumulants involve the subtraction of more and more terms, making it important to determine the precision with which they can be measured. We have stopped at fourth order because current analyses show that these cumulants can be measured with small error bars. If cumulants beyond fourth order are measured, it will be possible to construct further ratios of observables that overconstrain parameters or are independent of parameters.

Chapter 3

Strongly Coupled Plasmas - Baryon Screening

3.1 Introduction and Summary

In the previous Chapter we discussed experimental signatures of the critical point of the hadron to QGP phase transition. We now turn to study properties of quarks moving in strongly coupled plasmas using the AdS/CFT correspondence. In this Chapter we will look at the velocity dependence of the baryon screening length in $\mathcal{N} = 4$ SYM plasma and in Chapter 4, we will discuss the synchrotron radiation in the same theory at zero temperature.

In $\mathcal{N} = 4$ SYM theory at zero temperature, the static potential between a heavy external quark and antiquark separated by a distance L^{meson} is given in the large N_c and large λ limit by [122, 123]

$$V(L) = -\frac{4\pi^2}{\Gamma(\frac{1}{4})^4} \frac{\sqrt{\lambda}}{L^{\text{meson}}}, \tag{3.1}$$

where the $1/L^{\text{meson}}$ behavior is required by conformal invariance. This potential is obtained by computing the action of an extremal string world sheet, bounded at $z \to \infty$ (z being the fifth dimension of AdS$_5$ which is the inverse of u introduced in Chapter 1) by the world lines of the quark and antiquark and "hanging down"

77

from these world lines toward smaller z. At nonzero temperature, the potential becomes [124]

$$V(L^{\mathrm{meson}}, T) \approx \sqrt{\lambda} f(L^{\mathrm{meson}}) \qquad L^{\mathrm{meson}} < L_c^{\mathrm{meson}}$$
$$\approx \lambda^0 g(L^{\mathrm{meson}}) \qquad L^{\mathrm{meson}} > L_c^{\mathrm{meson}} \ . \qquad (3.2)$$

In (3.2), at $L_c^{\mathrm{meson}} = 0.24/T$ there is a change of dominance between different saddle points and the slope of the potential changes discontinuously. When $L^{\mathrm{meson}} < L_c^{\mathrm{meson}}$, the potential is determined as at zero temperature by the area of a string world sheet bounded by the worldlines of the quark and antiquark, but now the world sheet hangs down into a different five-dimensional spacetime: introducing nonzero temperature in the gauge theory is dual to introducing a black hole horizon in the five-dimensional spacetime. When $L^{\mathrm{meson}} \ll L_c^{\mathrm{meson}}$, $f(L^{\mathrm{meson}})$ reduces to its zero temperature behavior (3.1). When $L^{\mathrm{meson}} > L_c^{\mathrm{meson}}$, the potential arises from two disjoint strings, each separately extending downward from the quark or antiquark all the way to the black hole horizon. At $L^{\mathrm{meson}} \gg L_c^{\mathrm{meson}}$, $g(L^{\mathrm{meson}})$ is known and is determined by the exchange of the lightest supergravity mode between the two disjoint strings [125]. It is physically intuitive to interpret L_c as the screening length L_s of the plasma since at L_c the qualitative behavior of the potential changes. Similar criteria are used in the definition of screening length in QCD [126], although in QCD there is no sharply defined length scale at which screening sets in. Lattice calculations of the static potential between a heavy quark and antiquark in QCD indicate a screening length $L_s \sim 0.5/T$ in hot QCD with two flavors of light quarks [127] and $L_s \sim 0.7/T$ in hot QCD with no dynamical quarks [128]. The fact that there *is* a sharply defined L_c in (3.2) is an artifact of the limit in which we are working.

In Refs. [42, 129], the analysis of screening was extended to the case of a quark-antiquark pair moving through the plasma with velocity v. In that context, it proved convenient to define a slightly different screening length L_s^{meson}, which is the L^{meson} beyond which no connected extremal string world sheet hanging between the quark and antiquark can be found. At $v = 0$, $L_s^{\mathrm{meson}} = 0.28/T$ [124]. At nonzero v, up to

small corrections that have been computed [42, 129],

$$L_s^{\text{meson}}(v,T) \simeq L_s^{\text{meson}}(0,T)(1 - v^2)^{1/4} \propto \frac{1}{T}(1 - v^2)^{1/4} \,. \tag{3.3}$$

This result, also obtained in Ref. [130] and further explored in Refs. [131, 132, 133], has proved robust in the sense that it applies in various strongly coupled plasmas other than $\mathcal{N} = 4$ SYM [131, 132, 133]. The velocity dependence of the screening length (3.3) suggests that in a theory containing dynamical heavy quarks and meson bound states (which $\mathcal{N} = 4$ SYM does not) the dissociation temperature $T_{\text{diss}}(v)$, defined as the temperature above which mesons with a given velocity do not exist, should scale with velocity as [42]

$$T_{\text{diss}}(v) \simeq T_{\text{diss}}(v = 0)(1 - v^2)^{1/4} \,, \tag{3.4}$$

since $T_{\text{diss}}(v)$ should be the temperature at which the screening length $L_s^{\text{meson}}(v)$ is comparable to the size of the meson bound state. The scaling (3.4) indicates that slower mesons can exist up to higher temperatures than faster ones. This result has proved robust in a second sense, in that (3.4) has also been obtained by direct analysis of the dispersion relations of actual mesons in the plasma [134], introduced by adding heavy quarks described in the gravity dual by a D7-brane whose fluctuations are the mesons [135]. These mesons have a limiting velocity whose temperature dependence is equivalent to (3.4), up to few percent corrections that have been computed [134].

In the present Chapter, we shall return to the velocity-dependent screening length and test the robustness of (3.3) in yet a third sense, by analyzing the potential and screening length defined by a configuration consisting of N_c external quarks arranged in a circle of radius L.[1] In the gravity dual, there is a string hanging down from each of these quarks and at nonzero T and large enough L, the only extremal configuration of these string world sheets will be N_c disjoint strings. In order to obtain a baryon-

---

[1]The baryon static potential between three static quarks has been computed in QCD itself using lattice methods at zero temperature [136], and very recently the extension of these studies to nonzero temperatures and hence the study of baryon screening in QCD has been initiated [137].
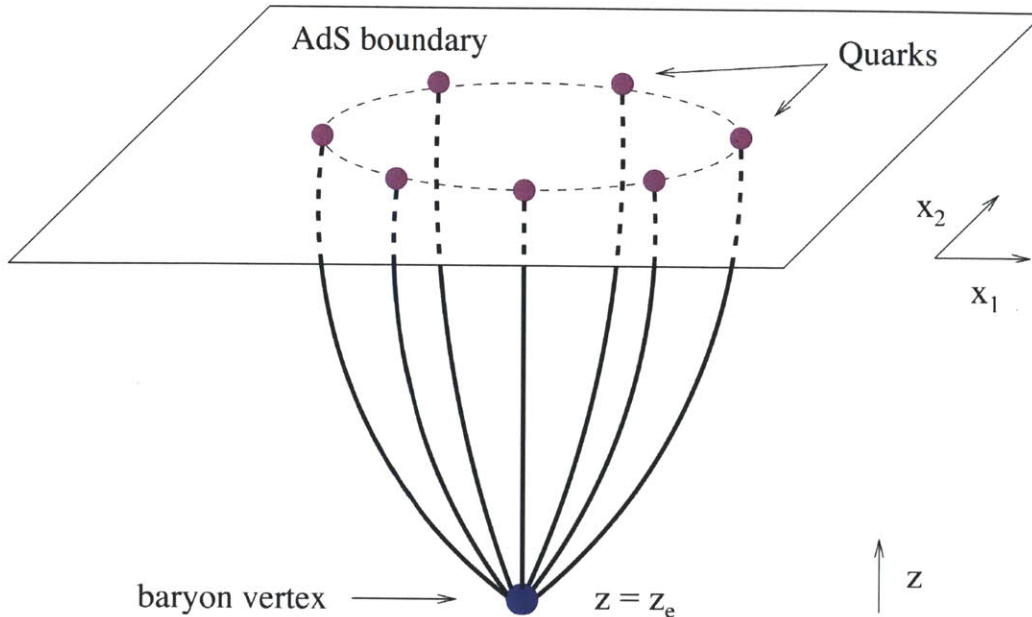
Figure 3-1: A sketch of a baryon configuration with N_c quarks arranged in a circle at the boundary of the AdS space, each connected to a D5-brane located at $z = z_e$ by a string.

like configuration, we introduce a D5-brane into the gravity dual theory which fills the 5 spatial dimensions of the S_5 and sits at a point in AdS$_5$, and on which N_c strings can end [138, 139, 140].[2] This now means that for L less than some L_s we can find configurations as in Fig. 3-1, in which the N_c strings hanging down from the quarks at the boundary of AdS$_5$ end on the D5-brane. Following Ref. [140], we have made the arbitrary choice of placing the N_c quarks in a circle; pursuing our

---

[2]We shall only consider the case where all N_c strings are located at the same point in the S_5; it would be interesting to generalize our analysis to the case where there are different species of quarks corresponding to strings located at different points in the S_5 which could then end at different points on the D5-brane. We are also neglecting the interactions between the Nc string endpoints on the D5-brane. Such interactions can be described via the Born-Infeld action for the D5-brane, and have been analyzed in Refs. [141] for the case where the baryons are BPS objects and the analysis can be pushed through to completion. In our case, in which supersymmetry is broken by the nonzero temperature and in which the baryon configurations need not be BPS objects even at zero temperature, such an analysis certainly presents technical challenges and may even be made uncontrolled by potential higher derivative corrections to the D5-brane Born-Infeld action. We shall follow Refs. [138, 139, 140] in neglecting string-string interactions. We shall find that the velocity dependence of the screening length is controlled by the kinematics of the AdS black hole metric under boosts: the fact that we find (see below) the same velocity dependence for the screening length defined by a baryon configuration which includes a D5-brane as has been found previously for that defined by the quark-antiquark potential whose calculation involves no D5-brane suggests, but absent a calculation does not demonstrate, that the addition of string-string interactions on the D5-brane will not modify our conclusions.

analysis to the point of phenomenology would certainly require investigating more generalized configurations.[3] Our central purpose, however, is to test the robustness of (3.3) in a theoretical context in which the D5-brane introduces a qualitatively new element. Note that in comparing our results for baryon screening to (3.3), if we want to compare numerical prefactors we should compare L to $L^{meson}/2$, since we have defined L as the radius of the circle in Fig. 3-1 rather than its diameter.

The D5-brane plays a role somewhat analogous what has been called a "baryon-junction" in various phenomenological analyses of baryons in QCD [142]. Baryon junctions in phenomenological analyses have usually been envisioned as well localized in (3+1)-dimensions, but this may not be the appropriate way of thinking of the D5-brane. The IR/UV relationship that characterizes the AdS/CFT correspondence [65] tells us that smaller values of the fifth-dimension coordinate z correspond to larger length scales R_{AdS}^2/z in the (3+1)-dimensional field theory, where R_{AdS} is the curvature of the AdS space.[4] The D5-brane is located at $z = z_e$, the lowest point in z of any part of the baryon configuration in Fig. 3-1. It therefore represents the longest wavelength "disturbance" of the (3+1)-dimensional gluon field (and other $\mathcal{N} = 4$ SYM fields) caused by the presence of the N_c quarks. We shall see in Section 3.3 that in $\mathcal{N} = 4$ SYM this length scale R_{AdS}^2/z_e is comparable to $2L$, meaning that the baryon vertex describes a disturbance of the gluon fields comparable in size to the circle of external quarks, not a baryon junction that is localized in (3+1)-dimensions.

The results (3.3) and (3.4) have a simple physical interpretation which suggests that they could be applicable to a wide class of theories regardless of specific details. First, note that since $L_s(0) \sim \frac{1}{T}$, both (3.3) and (3.4) can be interpreted as if in their rest frame the quark-antiquark dipole experiences a higher effective temperature $T\sqrt{\gamma}$. Although this is not literally the case in a weakly coupled theory, in which the dipole will see a redshifted momentum distribution of quasiparticles coming at it from some directions and a blueshifted distribution from others [143], we give an

---

[3]Note that for $N_c = 3$, there is no loss of generality in choosing the N_c quarks to lie in a single plane, but there is still an infinite space of distinct possible configurations to consider. Many have been considered in lattice investigations [136, 137].

[4]Note that in the Chapter 1 we introduced the inverse of the fifth-dimension u, which is related to z by $u = R_{AdS}^2/z$.

argument below for how this interpretation can nevertheless be sensible. The result (3.3) can then be seen as validating the relevance of this interpretation in a strongly coupled plasma. The argument is based on the idea that quarkonium propagation and dissociation are mainly sensitive to the local energy density of the medium. Now, in the rest frame of the dipole, the energy density ε is blue shifted by a factor $\sim \gamma^2$ and since $\varepsilon \propto T^4$ in a conformal theory, the result (3.3) is as if quarks feel a higher effective temperature given by $T\sqrt{\gamma}$. Lattice calculations indicate that the quark-gluon plasma in QCD is nearly conformal over a range of temperatures $1.5T_c < T \lesssim 5T_c$, with an energy density $\varepsilon \approx bT^4$ where b is approximately constant, at about 80% of the free theory value [144]. So it does not seem far-fetched to imagine that (3.3) could apply to QCD. We should also note that AdS/CFT calculations in other strongly coupled gauge theories with a gravity description are consistent with the interpretation above [132, 134] and that for near conformal theories the deviation from conformal theory behavior appears to be small [132]. If a velocity scaling like (3.3) and (3.4) holds for QCD, it can potentially have important implications for quarkonium suppression in heavy ion collisions [42, 134], in particular suggesting that in a heavy ion collision at RHIC (or LHC) which does not achieve a high enough temperature to dissociate J/Ψ (or Υ) mesons at rest, the production of these quarkonium mesons with transverse momentum above some threshold may nevertheless be suppressed [42]. Our results indicate that if baryons containing three charm quarks are ever studied in heavy-ion collision experiments, the suppression of their production could be similarly dependent on transverse momentum.

In Section 3.2 we shall set up a general formalism for finding baryon configurations of heavy external quarks in supergravity, with the N_c quarks arranged arbitrarily. In Section 3.3 we shall apply this general formalism to the configuration depicted in Fig. 3-1, allowing us to define a screening length L_s. In Section 3.3.1 we evaluate $L_s(v, T)$ for the case where the baryon configuration is moving through the plasma in a direction perpendicular to the plane defined by the circle of quarks. (Equivalently, the "baryon" feels a plasma wind blowing in a direction perpendicular to its plane.) Static configurations are found by extremizing the total baryon action coming from

82

both the strings and the D5 brane. We find static configurations only for $L < L_s(v,T)$ with $L_s(0,T) = 0.094/T$ as in [140], comparable to $\frac{1}{2}L^{\text{meson}}(0,T)$ above, and with

$$L_s(v,T) = \frac{0.083}{T}(1 - v^2)^{1/4} \tag{3.5}$$

in the $v \to 1$ limit. In this limit, we obtain (3.5) analytically. We find numerically that $L_s(v,T)T/(1 - v^2)^{1/4}$ varies monotonically and smoothly from 0.094 at $v = 0$ to 0.083 at $v \to 1$, making

$$L_s(v,T) \simeq L_s(0,T)(1 - v^2)^{1/4} \tag{3.6}$$

a good approximation. In Section 3.3.2 we do a similar numerical calculation for the case where the wind velocity is parallel to the baryon's plane. At high velocities we find a result like (3.5) except that the proportionality constant is different for different quarks/strings, depending weakly on the angle between the wind velocity and the string. L_s is smallest for the quarks whose strings are oriented perpendicular to the wind, even though in the configuration that we analyze these quarks are also closest to the D5-brane. This indicates that as v increases the medium is most effective at screening the potential felt by these quarks.

3.2   General baryon configurations

We wish to analyze a baryon configuration of N_c heavy external quarks in the $\mathcal{N} = 4$ SYM plasma at nonzero temperature. The baryon construction in supergravity involves N_c fundamental strings with the same orientation, beginning at the heavy quarks on the AdS boundary and ending on the baryon vertex in the interior of AdS$_5$, which is a D5 brane wrapped on the S$_5$ [138]. In this Section, we shall allow the N_c quarks to be placed at arbitrary positions in the (x_1, x_2, x_3)-space at the boundary of AdS. Note that the $\mathcal{N} = 4$ SYM plasma contains no particles in the fundamental representation, so the quarks we study here are external.

The gravity theory dual to $\mathcal{N} = 4$ SYM theory at nonzero temperature is the AdS

black hole times a five-dimensional sphere, with the metric

$$ds^2 = -f(z)dt^2 + \frac{z^2}{R_{AdS}^2}d\vec{x}^2 + \frac{dz^2}{f(z)} + R_{AdS}^2 d\Omega_5^2, \qquad (3.7)$$

where

$$f(z) = \frac{z^2}{R_{AdS}^2}\left(1 - \frac{z_h^4}{z^4}\right). \qquad (3.8)$$

Here, $d\Omega_5^2$ is the metric for a unit S_5, R_{AdS} is the curvature radius of the AdS metric, z is the coordinate of the fifth dimension of AdS$_5$ and z_h is the position of the black hole horizon. Note that in Chapter 1 we introduced the inverse of the fifth-dimension u, which is related to z by $u = R_{AdS}^2/z$. The temperature of the gauge theory is given by the Hawking temperature of the black hole, $T = z_h/(\pi R_{AdS}^2)$. And, the gauge theory parameters N_c and λ are given by $\sqrt{\lambda} = R_{AdS}^2/\alpha'$ and $\lambda/N_c = g_{YM}^2 = 4\pi g_s$, where α' is related to the string length l_s by $\alpha' \equiv l_s^2$, $1/(2\pi\alpha')$ is the string tension and g_s is the string coupling constant. (So, large N_c and λ correspond to large string tension and weak string coupling and thus justify the classical gravity treatment.)

We shall always work in the rest frame of the baryon configuration. This means that in order to describe N_c quarks moving through the plasma with velocity v, say in the x_3-direction, we must boost the metric (3.7) such that it describes a $\mathcal{N} = 4$ SYM plasma moving with a wind velocity v in the negative x_3-direction. We obtain

$$ds^2 = -Adt^2 + 2B\,dt\,dx_3 + C\,dx_3^2 + \frac{z^2}{R_{AdS}^2}\left(dx_1^2 + dx_2^2\right) + \frac{1}{f(z)}dz^2 + R_{AdS}^2 d\Omega_5^2, \qquad (3.9)$$

where

$$A = \frac{z^2}{R_{AdS}^2}\left(1 - \frac{z_1^4}{z^4}\right), \qquad B = \frac{z_1^2 z_2^2}{z^2 R_{AdS}^2}, \qquad C = \frac{z^2}{R_{AdS}^2}\left(1 + \frac{z_2^4}{z^4}\right), \qquad (3.10)$$

with

$$z_1^4 = z_0^4 \cosh^2 \eta, \quad \text{and} \quad z_2^4 = z_0^4 \sinh^2 \eta. \qquad (3.11)$$

We have defined the wind rapidity η via $v = -\tanh\eta$. Although in Section 3.3 we shall specialize to circular baryon configurations as illustrated in Fig. 3-1, in this

84

Section we describe the construction of a baryon configuration with N_c heavy external quarks placed at arbitrary locations in the $z \to \infty$ region of the boosted AdS metric (3.9).

The construction in this Section can easily be generalized to baryon configurations a large class of gauge theories at nonzero temperature, including $\mathcal{N} = 4$ SYM as one example. Consider any gauge theory that is dual in the large N_c and strong coupling limit to Type IIB string theory in the supergravity approximation in a generic string frame metric that can be written in the form

$$ds^2 = \tilde{g}_{\mu\nu}(z)dx^\mu dx^\nu + \frac{dz^2}{f(z)} + e^{2\psi(z)}ds_5^2 \; , \qquad (3.12)$$

with the possibility of a nontrivial dilaton $\phi(r)$. As before, $x^\mu = (t, \vec{x}) = (t, x_1, x_2, x_3)$ describe the Yang-Mills theory coordinates (the boundary coordinates). Here, ds_5^2 is the metric of some five-dimensional compact manifold X_5 that may not be S_5. A specific choice of gauge theory will correspond to specific choices of $\phi(z)$ and the various metric functions appearing in (3.12). The metric (3.12) is not even the most general that we could analyze, since for example we have not allowed the metric functions in (3.12) to depend on the coordinates of the internal manifold X_5 and since we have chosen the z-dependence of the X_5-metric to be a common factor $\exp(2\psi(z))$, not some more complicated structure. Such complications do not add qualitatively new features to the analysis of baryon configurations in a metric of the form (3.12). Our construction of baryon configurations below starting from the metric (3.12) could be applied to gauge theories known to have dual gravity descriptions some of which are conformal and some not, without or with nonzero R-charge density, with $\mathcal{N} = 4$ supersymmetry or to certain theories with only $\mathcal{N} = 2$ or $\mathcal{N} = 1$ supersymmetry, at nonzero or zero temperature, with or without a wind velocity. In our explicit definition of and calculation of the screening length L_s in Section 3.3, we shall return to the special case (3.9) of hot $\mathcal{N} = 4$ SYM theory with a wind velocity.

A baryon configuration in the supergravity metric (3.12) involves N_c fundamental strings beginning at the external heavy quarks on the boundary (which we will take

to be at $z = \infty$) and ending on the baryon vertex in the interior, which is a D5 brane wrapped on the compact manifold X_5 [138]. We denote the positions in $\vec{x}$-space where we place the external quarks by $\vec{q}^{(a)}$, with $a = 1, \cdots N_c$, and we take all the quarks to sit at the same point in the compact manifold X_5. We shall describe how to determine the location of the D5-brane below. After so doing, we shall shift the origin of the $\vec{x}$ coordinates such that the D5-brane sits at the origin, at $\vec{x}_e = 0$. We denote its position in the fifth dimension by $z = z_e$. The total action of the system is then given by

$$S_{\text{total}} = \sum_{a=1}^{N_c} S_{\text{string}}^{(a)} + S_{\text{D5}} , \tag{3.13}$$

where $S_{\text{string}}^{(a)}$ denotes the action of the fundamental string connecting the a-th quark with the D5-brane. Denoting the string worldsheet coordinates (τ, σ), we can choose

$$\tau = t, \qquad \sigma = z, \qquad x_i = x_i(\sigma) , \tag{3.14}$$

meaning that the shape of the a'th string worldsheet is described by functions $x_i^{(a)}(z)$ that extend from $\vec{x}^{(a)}(z_e) = \vec{x}_e$ to $\vec{x}^{(a)}(\infty) = \vec{q}^{(a)}$. The Nambu-Goto action of one string can then be written as

$$S_{\text{string}} = \frac{\mathcal{T}}{2\pi\alpha'} \int_{z_e}^{\infty} dz \sqrt{-\frac{\tilde{g}_{00}}{f} + (\tilde{g}_{0i}\tilde{g}_{0j} - \tilde{g}_{00}\tilde{g}_{ij}) x_i' x_j'} \equiv \frac{\mathcal{T}}{2\pi\alpha'} \int dr \, \mathcal{L}_{\text{string}}, \tag{3.15}$$

where $\mathcal{T}$ is the total time and where $x_i' \equiv \partial_z x_i$. The action for the five-brane can be written as

$$S_{\text{D5}} = \frac{\mathcal{V}(z_e)\mathcal{T} V_5}{(2\pi)^5 \alpha'^3}, \qquad \mathcal{V}(z) = \sqrt{-\tilde{g}_{00}} e^{-\phi+5\psi}, \tag{3.16}$$

where V_5 is the volume of the compact manifold X_5 and $\mathcal{V}(z_e)$ can be considered to be the gravitational potential for the D5-brane located at $z = z_e$.

In order to find a static baryon configuration, we must extremize S_{total}, first with respect to the functions $x_i^{(a)}(z)$ that describe the trajectories of each of the N_c strings and second with respect to $\vec{x}_e$ and z_e, the location of the D5-brane. Because S_{total} does not depend on the $x_i^{(a)}(z)$ explicitly, the variation with respect to $x_i^{(a)}(z)$ leads

86

to Euler-Lagrange equations that have a first integral

$$\frac{\partial \mathcal{L}_{\text{string}}^{(a)}}{\partial x_i^{\prime(a)}} = \frac{\left(\tilde{g}_{0i}\tilde{g}_{0j} - \tilde{g}_{00}\tilde{g}_{ij}\right) x_j^{\prime(a)}}{\mathcal{L}_{\text{string}}^{(a)}} = \text{const.} \equiv K_i^{(a)} \;, \tag{3.17}$$

where we have denoted the integration constants by $K_i^{(a)}$. Next, we extremize the action with respect to variations in the position of the D5-brane, understanding that as we vary its position we adjust the string trajectories as required by their Euler-Lagrange equations. Extremizing the action with respect to the location of the D5-brane in $\vec{x}$-space yields equations which receive one contribution from the boundary term at the D5-brane at $z = z_e$ in the variation of each of the $x_i^{(a)}(z)$, equations which take the form

$$\sum_a K_i^{(a)} = 0 \;. \tag{3.18}$$

(What arises from the variation are the $K_i^{(a)}$ evaluated at $z = z_e$, but the $K_i^{(a)}$ are by construction z-independent.) The constraint (3.18) is a force balance condition, encoding the requirement that in a static baryon configuration the net force exerted by the N_c strings on the D5-brane in the x_i directions, with $i = 1$, 2 and 3, must vanish. Extremizing S_{total} with respect to z_e yields the z-direction force balance condition which we can write as

$$\sum_{a=1}^{N_c} H^{(a)} \bigg|_{z_e} = \Sigma, \tag{3.19}$$

where

$$H^{(a)} \equiv \mathcal{L}^{(a)} - x_i^{\prime(a)}\frac{\partial \mathcal{L}^{(a)}}{\partial x_i^{\prime(a)}} = \frac{-\tilde{g}_{00}}{f(z)\mathcal{L}_{\text{string}}^a} \tag{3.20}$$

is the "upward" (i.e. in the positive z-direction) force on the D5-brane from the a'th string, meaning that the left-hand side of (3.19) is the upward force due to all the strings, and where

$$\Sigma \equiv \frac{2\pi\alpha'}{\mathcal{T}}\frac{\partial S_{\text{D5}}}{\partial z_e} = \frac{V_5}{(2\pi)^4\alpha'^2}\frac{\partial \mathcal{V}(z_e)}{\partial z_e} \tag{3.21}$$

is the downward gravitational force on the D5-brane, given its placement at $z = z_e$

in the curved spacetime (3.12).

Eqs. (3.17), (3.18) and (3.19) determine the shape of the string trajectories and the location of the D5-brane, which is to say that they determine the baryon configuration for a given choice of the positions of the quarks $\vec{q}^{(a)}$. Used in this way, one would integrate the first order equations (3.17), using the boundary conditions $\vec{x}^{(a)}(\infty) = \vec{q}^{(a)}$ to determine the integration constants $\vec{K}^{(a)}(\vec{q}^{(a)}, \vec{x}_e, z_e)$ for a given choice of $\vec{x}_e$ and z_e. Eqs. (3.18) and (3.19) can then be used to determine $\vec{x}_e$ and z_e. Not all choices of $\vec{q}^{(a)}$ will yield a static baryon configuration. For a given quark distribution at the boundary, the question of whether equations (3.17), (3.18) and (3.19) have solutions is a dynamical question depending on the specific metric under consideration. We shall see specific examples of how this plays out in Section 3.3.

Alternatively, a baryon configuration can be specified by starting with a set of $\vec{K}^{(a)}$ satisfying (3.18), solving for z_e using (3.19), and integrating Eqs. (3.17) outward from $z = z_e$ to the boundary at $z = \infty$, only then learning the quark positions $\vec{q}^{(a)}$ in the gauge theory. Instead of specifying $\vec{K}^{(a)}$, one can equivalently specify $\vec{s}^{(a)} \equiv \partial_z \vec{x}^{(a)}(z)|_{z=z_e}$.

Whether we think of specifying conditions at $z = z_e$ and integrating inwards or specifying conditions at the D5-brane, since we are considering the $N_c \to \infty$ limit it is often more convenient to introduce the density of quarks and strings instead of discrete position variables. At the boundary, the quark configuration can be specified by a density of quarks $\rho(\vec{q})$, which can be normalized as

$$\int d^3\vec{q}\,\rho(\vec{q}) = 1 \,. \tag{3.22}$$

We can then rewrite (3.18) as

$$\int d^3\vec{q}\,\rho(\vec{q})\,\vec{K}(\vec{q}) = 0 \,. \tag{3.23}$$

However, (3.19) cannot immediately be written in terms of $\rho(\vec{q})$ because the quantities in (3.19) are evaluated at $z = z_e$, and unlike the K's occurring in (3.18) are not z-independent. So, we must use the string trajectories themselves to relate the density

of quarks at $z = \infty$ to a density of strings at $z = z_e$, as follows. For any given z_e and $\vec{x}_e$, a solution $\vec{x}(z)$ to Eqs. (3.17) describes a single string trajectory which connects a particular point $\vec{q}$ at $z = \infty$ to the D5-brane at $\vec{x}(z_e) = \vec{x}_e$. The string connects to the D5-brane with a particular value of the "angle" $\vec{s} = \partial_z \vec{x}(z)|_{z=z_e}$. So, the set of string trajectories $\vec{x}(z)$ with all possible choices of $\vec{q}$ determine a mapping from $\vec{q}$ onto $\vec{s}$, where the $\vec{q}$'s specify the location of quarks at infinity and the $\vec{s}$'s specify strings at the D5-brane. Since the mapping corresponds to Hamiltonian "time" evolution (with z playing the role of time) Liouville's theorem tells us that a given $\rho(\vec{q})$ maps onto a $\rho_V(\vec{s})$ that specifies the density of strings hitting the D5-brane as a function of angle given by

$$\rho_V(\vec{s}) = \rho(\vec{q}) \left| \frac{\partial \, (q_1, q_2, q_3)}{\partial \, (s_1, s_2, s_3)} \right| . \tag{3.24}$$

In evaluating the Jacobian determinant, the $\vec{q}$'s should be considered to be functions of the $\vec{s}$'s, with the function being the mapping defined by the string trajectories $\vec{x}(z)$. If the solutions $\vec{x}(z)$ are nontrivial curved trajectories, then the relation between $\rho(\vec{q})$ and $\rho_V(\vec{s})$ will be nontrivial. Eqs. (3.18) and (3.19) can now be recast in terms of $\rho_V(\vec{s})$, namely[5]

$$\int d^3\vec{s}\, \rho_V(\vec{s})\, \vec{K}(\vec{s}) = 0 \tag{3.25}$$

and

$$\int d^3\vec{s}\, \rho_V(\vec{s})\, H(\vec{s}) = \frac{\Sigma}{N_c} . \tag{3.26}$$

Note that $\vec{K}(\vec{s})$ is obtained by evaluating the left hand side of (3.17) at $z = z_e$, while $H(\vec{s})$ is obtained by evaluating equation (3.20) at $z = z_e$.

We close this Section with a description of one way in which the formalism that we have developed can be used. Suppose that we wish to describe a baryon configuration in which the quarks all lie on some closed two dimensional surface in $\vec{x}$-space. For a given z_e, we can then use (3.18) in the form (3.23) to determine the density of quarks

---

[5]Note that in the continuous limit,

$$\frac{1}{N} \sum_a (\cdots) \to \int d^3\vec{s}\, \rho_V(\vec{s})(\cdots) = \int d^3\vec{q}\, \rho(\vec{q})(\cdots) .$$

along the surface required for any choice of $\vec{x}_e$ located inside the surface. Or, if the density of quarks along the surface has been specified, we can use (3.18) to determine $\vec{x}_e$ for a given z_e. We then repeat this exercise for all values of z_e until we find an z_e that satisfies (3.19) in the form (3.26).

In next Section we apply (3.17), (3.18) and (3.19) to particular baryon configurations in a $\mathcal{N} = 4$ SYM plasma moving with a nonzero wind velocity.

3.3 Velocity dependence of baryon screening in $\mathcal{N} = 4$ SYM theory

We now refocus on baryon configurations at rest in the plasma of $\mathcal{N} = 4$ SYM theory with temperature T moving with a wind velocity $v = -\tanh\eta$ in the x_3 direction. The gravity dual of this hot plasma wind is described by the metric (3.9). Following Ref. [140], we shall analyze baryon configurations in which the N_c quarks all lie in a single plane. In Section 3.3.1 we take the quarks to be uniformly distributed along a circle in the (x_1, x_2)-plane, perpendicular to the direction of the wind. In Section 3.3.2 we analyze a configuration in which the quarks lie in the (x_1, x_3)-plane, parallel to the direction of the wind. We expect that the two configurations we shall study are sufficient to illustrate the generic aspects of the velocity dependence of baryon screening in $\mathcal{N} = 4$ SYM theory.

3.3.1 Wind perpendicular to the baryon configuration

In this Subsection we consider a baryon configuration lying in the (x_1, x_2)-plane (i.e. $x_3 = 0$) perpendicular to the wind direction. For simplicity, we arrange the N_c external quarks uniformly around a circle of radius L as in [140], see Fig. 3-1. This is a simple example within which we can illustrate many aspects of the general formalism of Section 3.2 for constructing baryon configurations, and define and study the velocity dependence of the screening length.

With the quarks arranged uniformly around a circle, it is clear by symmetry that

the D5-brane must sit at the center of the circle, which we shall take to be at the origin: $\vec{x}_e = 0$. Because of the rotational symmetry of the circular configuration and of the background geometry (3.9), each of the N_c strings in Fig. 3-1 is equivalent. They all sit at $x_3 = 0$, and each can be described by a single function $x(z)$, where $x \equiv \sqrt{x_1^2 + x_2^2}$ extends from $x = 0$ and $z = z_e$, at the D5-brane, to $x = L$, at the boundary of AdS$_5$. With the D5-brane at $\vec{x}_e = 0$ at the center of the circle, it is clear that the forces in the $\vec{x}$ directions exerted by the strings on the D5-brane cancel, meaning that Eqs. (3.18) are automatically satisfied. The D5-brane sits at some $z = z_e$, which we shall determine for a given L using (3.19). So, $x(z_e) = 0$ and $x(\infty) = L$. Applying equations (3.15) and (3.16) to (3.9), we find that in this case

$$\mathcal{L}_{\text{string}} = \sqrt{A\left(\frac{(x')^2\, z^2}{R_{AdS}^2} + \frac{1}{f(z)}\right)}, \tag{3.27}$$

and

$$S_{\text{D5}} = \frac{N_c \mathcal{T} R_{AdS} \sqrt{A(z_e)}}{8\pi\alpha'}, \tag{3.28}$$

where $f(z)$ and $A(z)$ were given in Eqs. (3.8), (3.10) and (3.11). The equation (3.17) that determines the shape of the string trajectory $x(z)$ becomes

$$\frac{A\, z^2 x'}{R_{AdS}^2 \mathcal{L}_{\text{string}}} = K, \tag{3.29}$$

where by symmetry there is only a single integration constant K for all the strings. The z-direction force balance condition (3.19), namely the condition that the upward force on the D5-brane exerted by the N_c strings balances the downward force of gravity, becomes

$$\left.\frac{A}{f\mathcal{L}_{\text{string}}}\right|_{z_e} = \frac{1 + \rho^4 \cosh^2\eta}{4\sqrt{1 - \rho^4 \cosh^2\eta}} \equiv \Sigma(\rho, \eta), \tag{3.30}$$

where we have defined

$$\rho \equiv \frac{z_h}{z_e} = \frac{\pi R_{AdS}^2 T}{z_e}. \tag{3.31}$$

We must solve (3.29) and (3.30) simultaneously, in so doing obtaining both the position of the D5-brane z_e and the shape of the strings $x(z)$ corresponding to a static

91

baryon configuration with size L.

The integration constant K must be the same at any z. Upon evaluating it at $z = z_e$ and after some algebraic manipulations, equations (3.29) and (3.30) can be written more explicitly as

$$x' = \frac{K}{\sqrt{\left(A\frac{z^2}{R_{AdS}^2} - K^2\right)\frac{z^2}{R_{AdS}^2}f(z)}}, \tag{3.32}$$

and

$$\frac{K^2 R_{AdS}^4}{z_e^4} = 1 - \rho^4 \cosh^2\eta - (1 - \rho^4)\Sigma^2, \tag{3.33}$$

from which we obtain an explicit expression for the baryon radius L in terms of ρ and the rapidity η:

$$L = \frac{\rho}{\pi T}\left(1 - \rho^4\cosh^2\eta - (1 - \rho^4)\Sigma^2\right)^{\frac{1}{2}}\int_1^\infty dy\frac{1}{(y^4 - \rho^4)^{\frac{1}{2}}(y^4 - 1 + (1 - \rho^4)\Sigma^2)^{\frac{1}{2}}}, \tag{3.34}$$

where $y \equiv z/z_e$. We have evaluated (3.34) numerically, and in Fig. 3-2 we plot L versus ρ for several values of η. We see that L is small when ρ is small (meaning that z_e is large). As we decrease z_e, pulling the D5-brane in Fig. 3-1 downward, ρ increases and the size of the baryon configuration L at first increases, then reaches a maximum value, and then decreases to zero. For a given η, therefore, there is a maximum possible baryon radius, which we denote L_s, beyond which no baryon configurations are found. We shall identify L_s with the screening length, although in so doing we neglect a small correction that we shall discuss below. We see from Fig. 3-2 that at any η for $L < L_s(\eta)$ there are two solutions with different values of ρ. We shall see below that the configuration with the larger ρ is unstable and has a higher energy.

According to (3.34), the nonzero value of ρ at which $L \to 0$ in Fig. 3-2 is the ρ at which the right-hand side of (3.33) vanishes. At this value of ρ, K is zero and $\partial_z x|_{z_e} = 0$, corresponding to a configuration whose strings have become vertical. Note that the D5-brane becomes heavier when it is closer to the AdS black hole (i.e. Σ in (3.30) increases with ρ), meaning that the strings emerging from the D5-brane must
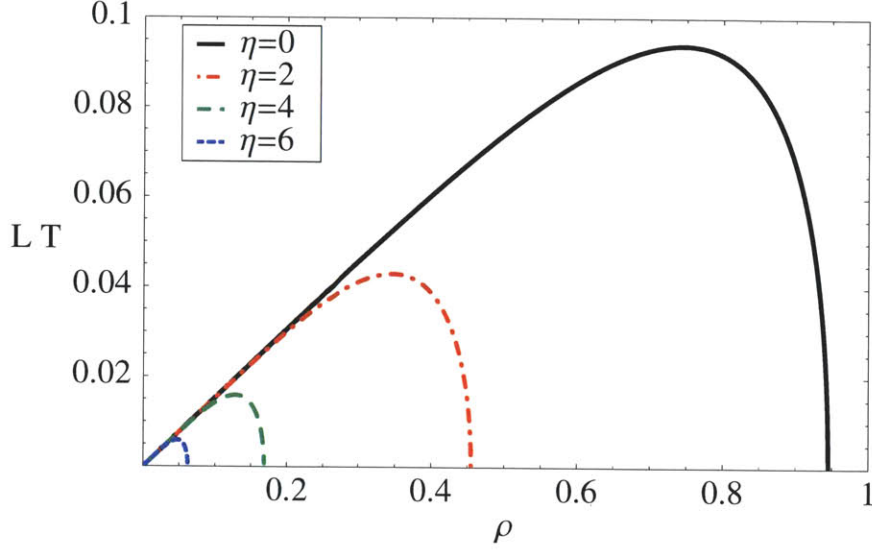
Figure 3-2: Baryon radius L versus ρ, where $\rho = z_h/z_e$ is the ratio of the position of the black hole horizon to the position of the D5-brane, for several different values of the rapidity η of the hot wind. The screening length L_s at a given η is the maximum of $L(\rho)$, namely the largest L at which a static baryon configuration can be found. We see that L_s decreases with increasing wind velocity.

be more and more vertical in order to hold it at rest. At some ρ, the strings become vertical and at larger ρ (smaller z_e) no static configuration can be found. From (3.33) we also see that this largest possible ρ is always smaller than the $\rho = 1/\sqrt{\cosh \eta}$ at which the speed v exceeds the local speed of light at the position of the D5-brane.

At any L for which there are two string configurations possible in Fig. 3-2, we expect that the solution with the larger ρ is unstable, as in the case of the string configuration between a quark and antiquark [145]. This instability can be seen on qualitative grounds as follows. For the solutions with smaller ρ, we see from Fig. 3-2 that L increases monotonically with ρ. This means that if we deform the configuration by pulling the D5-brane downward while keeping L fixed, the deformed configuration with its enlarged ρ has too small an L to be static. The fact that L "wants" to be larger means that the upward force on the D5-brane is greater than required to balance the downward force of gravity. So, there is a net restoring force pulling the D5-brane back upwards and the original configuration is stable against this deformation. In contrast, for the solutions with larger ρ we see from Fig. 3-2 that L decreases monotonically

93

with ρ, meaning that if we pull the D5-brane downward, L "wants" to be smaller and the upward force on the D5-brane is less than the downward force of gravity (the downward force has increased more than the upward force) and the D5-brane will accelerate downward. The configurations described by the part of the curve in Fig. 3-2 for which L decreases with increasing ρ are therefore unstable. We shall see below that these configurations have higher energy than the stable configurations with the same L and smaller ρ.

We can use (3.34) and Fig. 3-2 to compare the length scale R_{AdS}^2/z_e of the disturbance of the gluon field induced by the N_c external quarks to $2L$, the size of the circle of quarks itself. In the small-ρ limit, (3.34) simplifies to

$$LT \approx \frac{0.4811\,\rho}{\pi} \,, \tag{3.35}$$

which describes the linear region seen in all of the curves in Fig. 3-2 at small ρ. This implies that at small ρ

$$\frac{R_{AdS}^2}{z_e} \approx 2.079\,L \,, \tag{3.36}$$

comparable to $2L$. We see from Fig. 3-2 that as we go from this small ρ regime towards $L = L_s$, the ratio of R_{AdS}^2/z_e to $2L$ increases by a further few tens of percent.

We see from Fig. 3-2 that the screening length L_s decreases with increasing velocity. At zero velocity, $L_s = 0.094/T$ as can be obtained from previous results [140]. We have evaluated L_s as a function of rapidity η, and shall plot the result in Fig. 3-7, along with analogous results from Section 3.3.2 for the case where the wind velocity is parallel to the plane of the baryon configuration. From our numerical evaluation, we find that at large η

$$L_s \approx \frac{a}{T\sqrt{\cosh\eta}}, \tag{3.37}$$

with $a = 0.0830$. The screening length for a quark and antiquark separated by a distance L^{meson} moving through the plasma in a direction perpendicular to the dipole also takes the form (3.37) in the high velocity limit, with $a = 0.237$ [42]. When we compare the L_s that we have computed for the baryon configuration to $L_s^{\text{meson}}/2$ (the

"radius" of the meson configuration at its screening length) we see that, in addition to having precisely the same velocity dependence at high velocity, their numerical values are comparable. Finally, it is perhaps not surprising that L_s^{baryon} is somewhat smaller than $L_s^{\text{meson}}/2$, for a given η and T, since the baryon vertex (D5-brane) pulls the strings further downward, closer to the horizon.

We can also find the large η dependence of L_s analytically. If we define

$$\hat{\rho} \equiv \rho\sqrt{\cosh\eta}, \qquad \hat{L} \equiv L\sqrt{\cosh\eta} \tag{3.38}$$

and take the scaling limit in which

$$\eta \to \infty \quad \text{with} \quad \hat{\rho}, \ \hat{L} \quad \text{held fixed}, \tag{3.39}$$

we find that $\cosh\eta$ drops out of the leading terms in Eq. (3.34) and this equation becomes

$$\begin{aligned}
\hat{L} &= \frac{\hat{\rho}}{\pi T}\left(1 - \hat{\rho}^4 - \Sigma^2\right)^{\frac{1}{2}} \int_1^\infty dy \frac{1}{y^2\left(y^4 - 1 + \Sigma^2\right)^{\frac{1}{2}}} + O\left((\cosh\eta)^{-\frac{1}{2}}\right) \\
&= \frac{\hat{\rho}}{3\pi T}\left(1 - \hat{\rho}^4 - \Sigma^2\right)^{\frac{1}{2}} {}_2F_1\left(\frac{1}{2}, \frac{3}{4}, \frac{7}{4}, 1 - \Sigma^2\right) + O\left((\cosh\eta)^{-\frac{1}{2}}\right) .
\end{aligned} \tag{3.40}$$

(Note that according to (3.30), Σ only depends on $\hat{\rho}$.) The right-hand side of (3.40) is function of $\hat{\rho}$ that goes to zero at $\hat{\rho} \to 0$ and at $\hat{\rho} \to 0.880$, and that has a maximum at $\hat{\rho} = 0.666$ where $\hat{L} = 0.0830/T$, yielding an L_s that is in precise agreement with (3.37).

We close this Section by evaluating the energy of the baryon configurations that we have constructed. The energy of one string can be found using S_{string} and is given by

$$\begin{aligned}
E_{\text{string}} &= \frac{1}{2\pi\alpha'} \int_{z_e}^\infty dz \sqrt{A\left(\frac{(x')^2 z^2}{R_{AdS}^2} + \frac{1}{f}\right)} \\
&= \frac{T\sqrt{\lambda}}{2\rho} \int_1^\infty dy \frac{y^4 - \rho^4\cosh^2\eta}{(y^4 - \rho^4)^{\frac{1}{2}}\left(y^4 - 1 + (1 - \rho^4)\Sigma^2\right)^{\frac{1}{2}}} ,
\end{aligned} \tag{3.41}$$

where $y \equiv z/z_e$. This energy is infinite because we have included the masses of the
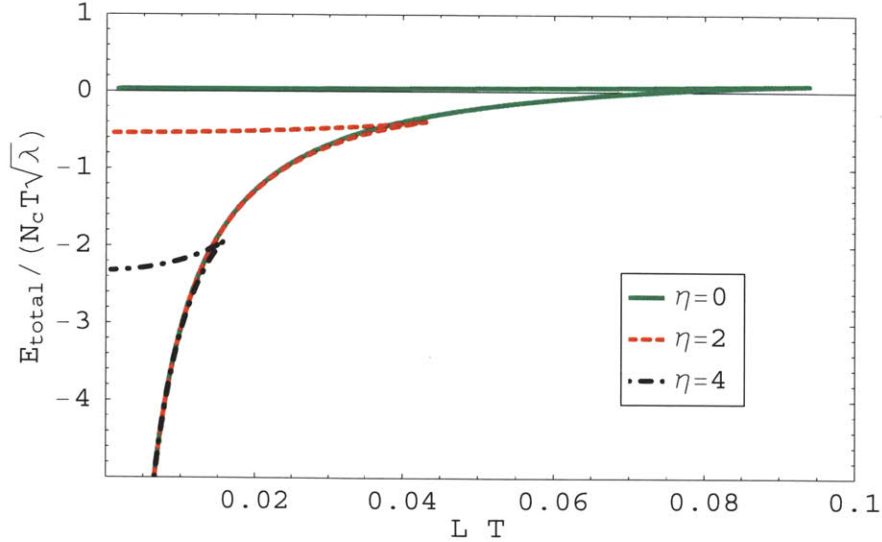
Figure 3-3: The total energy of the baryon configuration with a given L (relative to that of N_c disjoint quarks moving with the same velocity) for several values of the wind rapidity η. The lower (higher) energy branch corresponds to the solution in Fig. 3-2 with lower (higher) ρ. The cusps where the two branches meet are at $L = L_s$.

quarks. As in Refs. [42, 129], we regularize the baryon energy by subtracting the energy of (in this case N_c) disjoint quarks in a hot plasma wind of velocity v, whose strings are dragging behind them in the x_3 direction according to the solution found in [83, 84]. This corresponds to regulating the z-integral in (3.41) with a large-z cutoff Λ, subtracting

$$E_{\text{mass}} = \frac{N_c}{2\pi\alpha'} \int_{z_h}^{\Lambda} dz = \frac{N_c T \sqrt{\lambda}}{2\rho} \int_{\rho}^{\Lambda/z_e} dy \ , \tag{3.42}$$

and then taking Λ to infinity. This procedure yields a finite answer. The total energy of the baryon (strings plus D5-brane) becomes

$$
E_{\text{total}} = \frac{N_c T \sqrt{\lambda}}{2} \left[\frac{1}{\rho} \int_1^{\infty} dy \left(\frac{y^4 - \rho^4 \cosh^2 \eta}{(y^4 - \rho^4)^{\frac{1}{2}} (y^4 - 1 + (1 - \rho^4)\Sigma^2)^{\frac{1}{2}}} - 1 \right) + 1 - \frac{1}{\rho} \right.
$$
$$
\left. + \frac{\sqrt{1 - \rho^4 \cosh^2 \eta}}{4\rho} \right] \ , \tag{3.43}
$$

where the last term is the contribution of the D5 brane to the energy.

In Fig. 3-3 we plot the energy of the baryon configurations at several values of η. As in Fig. 3-2, we see two configurations at every $L < L_s$. We have argued above

that the higher energy configurations (those with the larger ρ) are unstable, so we focus on the lower branch. We see that at $\eta = 0$ this branch crosses zero energy at $L = 0.073/T$, whereas the largest L at which a baryon configuration can be found is $L_s = 0.094/T$. This means that for $0.073 < LT < 0.094$, even the lower branch solutions have become metastable, as they have more energy than N_c disjoint quarks. We see from Fig. 3-3 that this phenomenon does not occur at larger velocities; in fact, it arises only for $\eta \leq 0.755$ since at $\eta = 0.755$ the baryon configuration with $L = L_s$ has the same energy as N_c disjoint quarks, i.e. zero energy in Fig. 3-3. At the low velocities $\eta < 0.755$, a more precise definition of the screening length would be to define it as the length at which the lower curve in Fig. 3-3 crosses zero. We see from Fig. 3-3 that by using L_s as our definition of the screening length at all velocities, as we do for simplicity, we are introducing only a small imprecision at low velocities, $\eta < 0.755$. These considerations have no effect on our calculation of L_s at large η, namely (3.37).

It is clear from (3.43) that in the large η limit (3.39) with $\hat{L}$ held fixed and L therefore decreasing, the energy scales as $-\sqrt{\cosh \eta}$. This scaling can also be deduced from Fig. 3-3, as follows. The subtraction term (3.42) is defined such that for any given T and η, at small enough L the potential energy $E(L)$ is the same as in vacuum (i.e. for $T = \eta = 0$), namely $E(L) \propto -1/L$. And, if $E \propto -1/L$ and the $E(L)$ curves for different η overlap as seen in Fig. 3-3, then E must scale like $-\sqrt{\cosh \eta}$ in the limit (3.39).

The baryon configuration that we have analyzed in this Subsection is special in that all N_c strings are equivalent. In the next Subsection we shall analyze a configuration for which this is not the case, for which we shall need the full formalism developed in Section 3.2.

3.3.2 Wind parallel to the baryon configuration

We now analyze the case where the N_c quarks are moving through the plasma (or, equivalently in their rest frame, feeling a hot wind blowing) in a direction parallel to their plane. We shall keep the wind blowing in the x_3 direction as before, meaning

that the boosted AdS black hole metric given by (3.9) is unchanged. We shall now put the N_c quarks in the (x_1, x_3)-plane.

With the quarks in the (x_1, x_3)-plane and the wind velocity in the x_3 direction, the N_c strings in a circular baryon configuration are no longer equivalent, as the strings make different angles relative to the wind direction. The N_c strings would not all hit the D5-brane at the same angle in this case. Analyzing this case is possible, but we will instead consider a simpler configuration in which all N_c strings hit the D5-brane symmetrically. In terms of the formalism developed in Section 3.2, we choose a configuration in which the string density at the D5-brane is

$$\rho_V(s_1, s_2, s_3) = \frac{1}{\pi} \delta(s_1^2 + s_3^2 - s^2) \, \delta(s_2) \,, \tag{3.44}$$

where s is some constant and $s_i = \partial_z x_i(z)|_{z_e}$. The distribution (3.44) corresponds to requiring that the N_c strings hit the D5-brane with a uniform distribution in the azimuthal angle ϕ in the (x_1, x_3)-plane and all with the same $\partial_z x|_{z_e} = s$. (Here, $x \equiv \sqrt{x_1^2 + x_3^2}$.) Unlike in the previous Subsection, this specification of the baryon configuration in the vicinity of $z = z_e$ will *not* correspond to having the N_c quarks at $z = \infty$ arranged on a circle. Note that (3.44) guarantees that the net force exerted on the D5-brane in the x_1- and x_3-directions by the N_c quarks vanishes, meaning that (3.25), or equivalently (3.18), is automatically satisfied. Given the choices that we have made in specifying our baryon configuration, our task is twofold: we must determine s as a function of z_e such that the forces on the D5-brane in the z-direction due to gravity and due to the strings cancel; and, we must solve for the shape of the strings to determine what baryon configuration at $z = \infty$ our choices correspond to.

The shape of each string is specified by two functions $x_1(z)$ and $x_3(z)$ that we must obtain. We shall find that, when projected onto the (x_1, x_3)-plane, the string worldsheets do not follow radial trajectories. That is, the trajectories $x_1(z)$ and $x_3(z)$ are not specified just by $x(z)$; their azimuthal angle ϕ is a nontrivial function of z also.

Applying equations (3.15) and (3.16) to (3.9) with nontrivial $x_1(z)$ and $x_3(z)$, we

find that

$$\mathcal{L}_{\text{string}} = \sqrt{A\left(\frac{1}{f(z)} + \frac{(x_1')^2 z^2}{R_{AdS}^2}\right) + \frac{(x_3')^2 z^2 f(z)}{R_{AdS}^2}} \ , \tag{3.45}$$

and find that the D5-brane action is given by (3.28) as before. With $\mathcal{L}_{\text{string}}$ given by (3.45), the equations of motion (3.17) can be rearranged to give

$$x_1'^2 = \left(\frac{R_{AdS}^4}{z^2}\right)\left(\frac{K_1^2}{z^2 f A - R_{AdS}^2 K_3^2 A - R_{AdS}^2 K_1^2 f}\right) , \tag{3.46}$$

$$x_3'^2 = \left(\frac{R_{AdS}^4}{f^2 z^2}\right)\left(\frac{K_3^2 A^2}{z^2 f A - R_{AdS}^2 K_3^2 A - R_{AdS}^2 K_1^2 f}\right) . \tag{3.47}$$

Equation (3.19) for the balance of force in the radial direction becomes

$$\sum_{\text{strings}} \frac{R_{AdS}\, A/\sqrt{f}}{\sqrt{A\left(R_{AdS}^2 + f z^2 x_1'^2\right) + f^2 z^2 x_3'^2}}\bigg|_{z_e} = N_c \Sigma(\rho, \eta) \ , \tag{3.48}$$

where $\Sigma(\rho, \eta)$ is as in (3.30) and is the downward gravitational force on the D5-brane and the left-hand side of (3.48) is the upward force due to the N_c strings. If we define ϕ to be the azimuthal angle in the (x_1, x_3)-plane that a string makes at $z = z_e$ where it connects to the D5-brane, defined such that $\phi = 0$ ($\phi = \pi/2$) is in the positive-x_3 (positive-x_1) direction, then our choice of having the N_c strings uniformly distributed in ϕ turns the sum over strings in equation (3.48) into an integral over ϕ,

$$\sum_{\text{strings}} \rightarrow N_c \int_0^{2\pi} \frac{d\phi}{2\pi}, \tag{3.49}$$

and expression (3.48) becomes

$$\frac{R_{AdS}\, A}{\sqrt{f}} \int_0^{2\pi} \frac{d\phi}{2\pi} \frac{1}{\sqrt{A R_{AdS}^2 + s^2 f z^2 \left(A \sin^2\phi + f \cos^2\phi\right)}}\bigg|_{z_e} = \Sigma(\rho, \eta), \tag{3.50}$$

where $s = \partial_z x|_{z_e}$ was introduced in (3.44) and as before $\rho \equiv z_h/z_e$.

The constants K_1 and K_3 must be the same at any z. By evaluating (3.46) and

99

(3.47) at $z = z_e$ and rearranging, we determine that

$$K_1^2 = \frac{s^2 A^2 z^4 f \sin^2 \phi}{R_{AdS}^2 \left(A R_{AdS}^2 + s^2 z^2 f \left(A \sin^2 \phi + f \cos^2 \phi\right)\right)}\bigg|_{z_e}, \qquad (3.51)$$

$$K_3^2 = \frac{s^2 z^4 f^3 \cos^2 \phi}{R_{AdS}^2 \left(A R_{AdS}^2 + s^2 z^2 f \left(A \sin^2 \phi + f \cos^2 \phi\right)\right)}\bigg|_{z_e}. \qquad (3.52)$$

With these integration constants now determined, we can integrate Eqs. (3.46) and (3.47), obtaining

$$x_1(z) = \frac{\rho^3 R_{AdS}^4 K_1}{z_h^3} \int_1^{z/z_e} dy \frac{1}{\sqrt{Q}}, \qquad (3.53)$$

and

$$x_3(z) = \frac{\rho^3 R_{AdS}^4 K_3}{z_h^3} \int_1^{z/z_e} dy \frac{y^4 - \rho^4 \cosh^2 \eta}{y^4 - \rho^4} \frac{1}{\sqrt{Q}}, \qquad (3.54)$$

where

$$Q \equiv (y^4 - \rho^4)(y^4 - \rho^4 \cosh^2 \eta) - \frac{R_{AdS}^4 \rho^4 K_1^2}{z_h^4}(y^4 - \rho^4) - \frac{R_{AdS}^4 \rho^4 K_3^2}{z_h^4}(y^4 - \rho^4 \cosh^2 \eta). \qquad (3.55)$$

Equations (3.53) and (3.54) specify the shape of the string worldsheets, while z_e (equivalently, ρ) is determined in terms of s by (3.50).

The calculation proceeds as follows. First, we solve (3.50) numerically to obtain the s required at a given ρ. Second, we pick a particular value of ϕ and use s to evaluate (3.51) and (3.52), obtaining the z-independent, but ϕ-dependent, K_1 and K_3. Third, we evaluate (3.53) and (3.54) numerically, thus obtaining the shape of the string with a particular value of ϕ. The position of the quark at $z = \infty$ corresponding to this choice of ϕ is then $(x_1(\infty), x_3(\infty))$ and we can determine $L = \sqrt{x_1(\infty)^2 + x_3(\infty)^2}$ for this choice of ϕ. Fourth, we repeat the second and third steps for all values of ϕ.

In Fig. 3-4 we show the L obtained as we have just described at three values of ϕ, as a function of ρ. We conclude from the fact that L is different for different values of ϕ that the N_c quarks at $z = \infty$ are not arranged in a circle in the (x_1, x_3)-plane. We illustrate this explicitly in Figs. 3-5 and 3-6. We started with circularly sym-
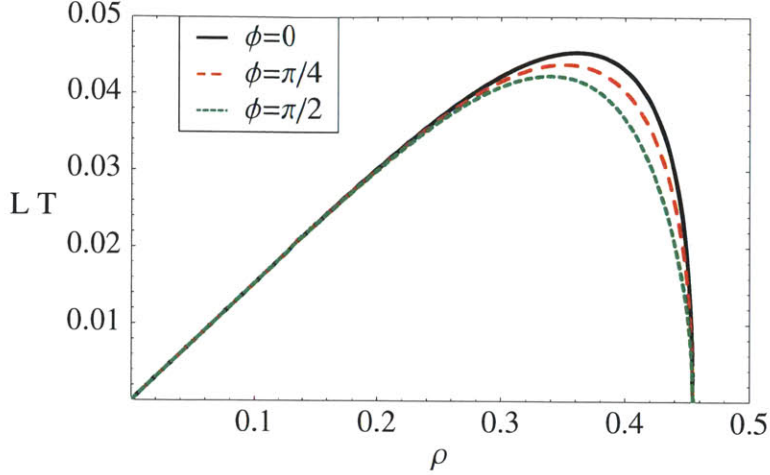
Figure 3-4: L versus ρ for strings oriented in the $\phi = 0, \pi/4, \pi/2$ directions in the (x_1, x_3)-plane in a baryon configuration immersed in a plasma moving in the x_3-direction with rapidity $\eta = 2$. We see that at a given ρ the distance L in the (x_1, x_3)-plane between a quark and the D5-brane at the center of the baryon configuration depends on the angular position of the quark. This means that the N_c quarks do not lie on a circle.
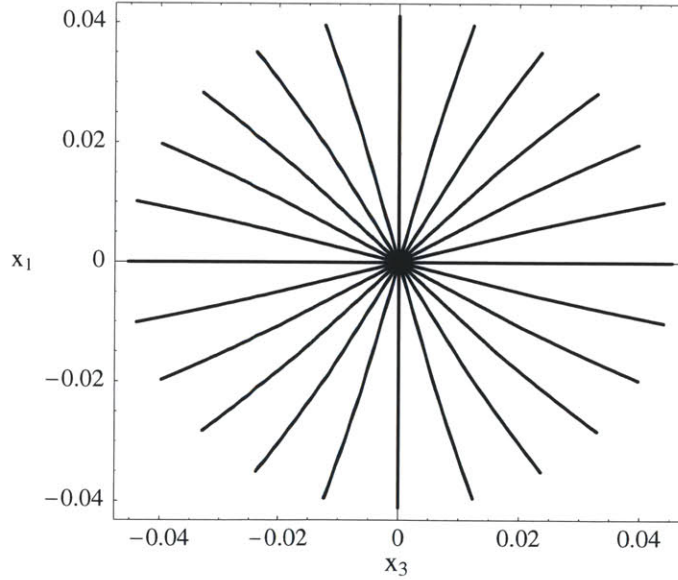
Figure 3-5: Strings projected on the AdS boundary for $\eta = 2$ and $\rho = 0.37$ for strings separated in ϕ by $\pi/12$. (We have done all our calculations for $N_c \to \infty$, but have shown only 24 quarks in the Figure.) Baryon motion is in the x_3 direction. The Figure is drawn in the rest frame of the baryon, meaning there is a hot wind in the x_3 direction. The N_c quarks that make up the baryon configuration are not arranged in a circle: the "squashed circle" is wider in the direction of motion. Note also that the projection of the strings are not straight lines.

101
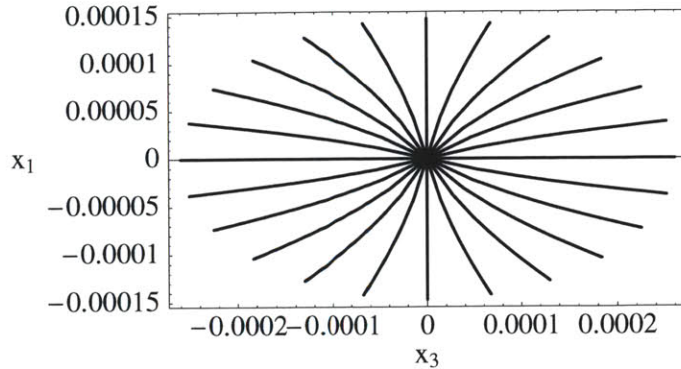
Figure 3-6: Same as Fig. 3-5, but for $\rho = 0.4550611$, very close to the maximum ρ at which a baryon configuration can be found at $\eta = 2$. This configuration is unstable, and has higher energy than the configurations with comparable L's at much lower ρ. However, it illustrates the "squashing" of the baryon configuration away from a circular shape and the curvature of the projections of the strings onto the (x_1, x_3) plane. Both these effects are present in Fig. 3-5, but are more visible here.

metric boundary conditions at the D5-brane, but the resulting baryon configuration at the AdS boundary is "squashed", wider in the direction of motion of the baryon and narrower in the perpendicular direction. Inspection of Fig. 3-4 or comparison of Figs. 3-5 and 3-6 shows that the shape of the baryon configuration at the AdS boundary changes with ρ, becoming more squashed as ρ increases. In Figs. 3-5 and 3-6 we also see that the projections of the string worldsheets onto the (x_1, x_3)-plane are not straight radial lines. Their curved shapes are strikingly similar to the shapes of the projections of strings joining a static quark-antiquark in the meson configurations analyzed in Refs. [42, 129], although they are not precisely the same. Note that Eqs. (3.50)–(3.52) are symmetric in $\phi \to \pi - \phi$, which implies that string configurations are symmetric with respect to reflection in the x_1 axis, i.e. under $x_3 \to -x_3$, as is manifest in Figs. 3-5 and 3-6. This forward-backward symmetry of the string configurations indicates that the baryon configuration feels no drag as it is moved through the plasma, just as for meson configurations [130, 42, 129], and as has been demonstrated previously for baryon configurations with zero size [146].

It is straightforward to compute the energy of the baryon configurations that we have found, as a function of ρ, but since (unlike in Subsection 3.3.1) the configurations are not characterized by a single $L(\rho)$ there is no analogue of Fig. 3-3 here. Also,

102
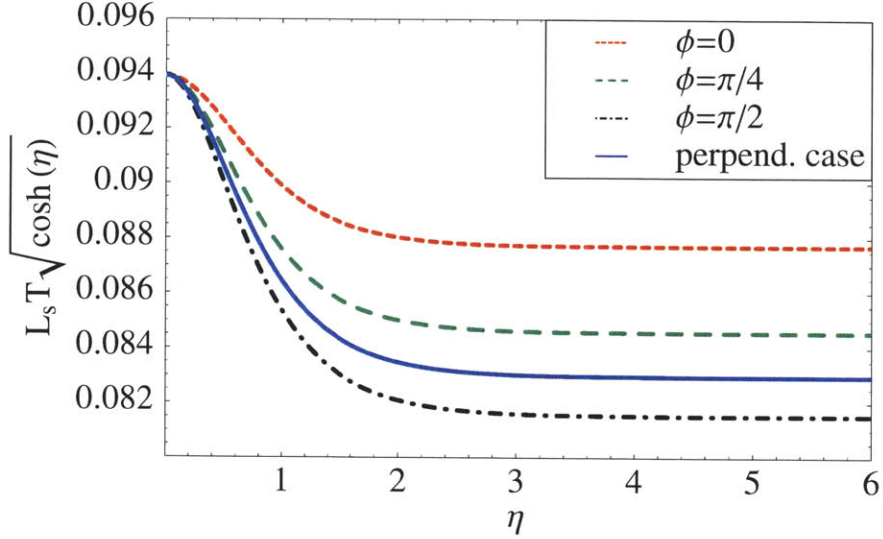
Figure 3-7: The screening length L_s as a function of η with its large-η dependence $\sqrt{\cosh\eta}$ scaled out. The solid curve is for the case of a wind velocity perpendicular to the plane of the baryon, as in Section 3.3.1. The other three curves are for wind velocity in the plane of the baryon, and show the L_s for the strings that make an angle $\phi = 0, \pi/4, \pi/2$ with the direction of the wind.

(again unlike when the wind blows perpendicular to the baryon configuration as in Subsection 3.3.1) we have no simple argument for at what ρ the baryon configurations in this Subsection become unstable. Our argument in the previous Subsection relied on the equivalence of all N_c strings, in that at a single ρ there was a change from "a deformation that increases ρ makes all N_c strings want to have larger L" to "a deformation that increases ρ makes all N_c strings want to have smaller L". Here, we see from Fig. 3-4 that there is a range of ρ within which a deformation that increases ρ makes some strings want to have smaller L while other strings want to have larger L. Within this range of ρ, our simple argument yields no conclusion and a full stability analysis as in Refs. [145] is required. We leave this to future work.

The maxima of curves as in Fig. 3-4 define a screening length L_s for each ϕ as a function of η. In Fig. 3-7 we plot $L_s T\sqrt{\cosh\eta} = L_s T/(1-v^2)^{1/4}$ versus η for different values of ϕ. We find that the large-η dependence of the screening length has the same form in all cases, namely

$$L_{s,\,\eta\gg1} \propto \frac{1}{T\sqrt{\cosh\eta}} \; . \tag{3.56}$$

103
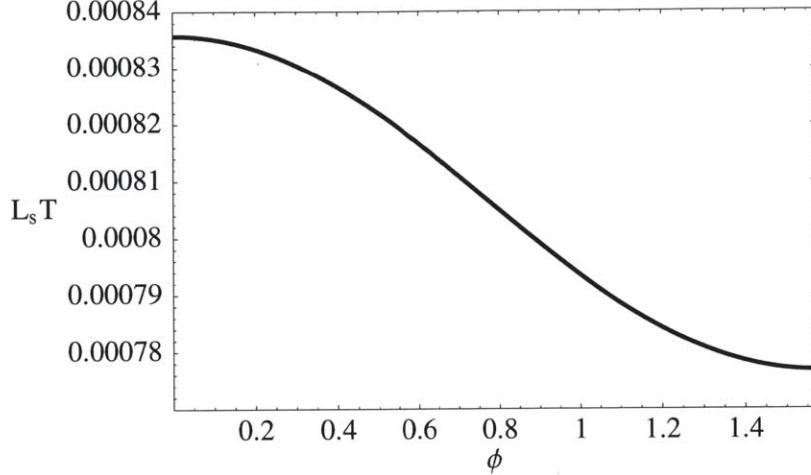
Figure 3-8: The screening length L_s as a function of ϕ at a large value of η. Specifically, $\eta = 10$ corresponding to $\sqrt{\cosh\eta} = 1/(1 - v^2)^{1/4} = 104.9$.

This is the same large η dependence found in Section 3.3.1, Eq. (3.37), and in mesons, Eq. (3.3). To make the former comparison manifest, in Fig. 3-7 we have also plotted $L_s T \sqrt{\cosh\eta}$ for the case analyzed in Section 3.3.1 in which the wind velocity is perpendicular to the plane of the baryon configuration. When the wind velocity is parallel to the plane of the baryon configuration, L_s has a weak angular dependence. In particular, the constant of proportionality in Eq. (3.56) varies between 0.082 and 0.088 for different ϕ, as can be seen in Fig. 3-7. A plot of L_s in the large η regime as a function of ϕ is given in Fig. 3-8, which shows the smooth variation of L_s for large η as we change ϕ. Note also that (3.56) is a good approximation all the way down to the small velocity limit $\eta \to 0$, since the proportionality constant in Eq. (3.56) merely changes from its (ϕ-dependent) value at large η to the (obviously ϕ-independent) value 0.094 at $\eta = 0$. The central conclusion to be drawn from Fig. 3-7, then, is that the simple velocity scaling (3.6) is a good approximation at all velocities and all angles.

The similarities between our results and those for the meson screening length go beyond just the dominant velocity scaling. Indeed, Fig. 3-7 is strikingly similar to Fig. 7 of Ref. [129]. There too, for the quark-antiquark case, $L_s T \sqrt{\cosh\eta}$ is largest at $\eta = 0$, a few percent smaller for $\eta \to \infty$ if the quark-antiquark dipole is oriented

104

parallel to the wind, and a few percent smaller still if the dipole is oriented perpendicular to the wind. The only feature in our Fig. 3-7 that does not have a direct, almost quantitative, analogue in Ref. [129] is the *very* small difference between the curves for the two cases in which the wind direction is perpendicular to the line between the quark and the D5-brane, namely the case in which the wind is parallel to the plane of the baryon configuration and the quark is at $\phi = \pi/2$ and the case in which the wind is perpendicular to the plane of the baryon configuration.

Although we have only done our analysis for a wind that is either perpendicular to or parallel to the plane of the baryon configuration, we expect that the qualitative features that we have found in this Section should all be present for any wind direction except perpendicular.

In Subsections 3.3.1 and 3.3.2 we have analyzed two particular baryon configurations that suffice to make our point regarding the velocity dependence of baryon screening. The general formalism of Section 3.2 can straightforwardly be applied to baryon configurations with other shapes, whether specified by the density of quarks at infinity or the density of strings at the D5-brane vertex. Technically, in order to solve equations (3.18) and (3.19), it is simpler to specify the density of strings at the D5-brane as we have done in this Subsection, but there is no obstacle of principle to analyzing arbitrary densities of quarks at infinity in any wind velocity. While the behavior at small η could differ for more general configurations, we expect that in the large η limit, the scaling behavior (3.56) should still apply. The formalism of Section 3.2 can also be used to generalize our results to the plasmas of other strongly coupled gauge theories. For example, following a line of reasoning developed in Ref. [132] for the meson sector, it can be shown that in a certain class of gauge theories whose gravity duals are asymptotically AdS, as $v \to 1$ the baryon screening length scales as $L_s \propto (1 - v^2)^{1/4}/\hat{\epsilon}^{1/4}$, where $\hat{\epsilon}$ is the energy density of the plasma. $\hat{\epsilon}$ is proportional to T^4 for the specific theory that we have analyzed, at any v, in this Section.

3.4 Discussion

We have analyzed the screening of the static potential for a baryon configuration consisting of N_c quarks in a circle (or slightly squashed circle) moving with velocity v through the plasma of $\mathcal{N} = 4$ SYM theory in a direction perpendicular (or parallel) to the plane of the configuration. We find a screening length

$$L_s = \frac{a(1 - v^2)^{1/4}}{T} , \tag{3.57}$$

where a depends only weakly on v and angles. For example, $a = 0.094$ for $v = 0$ while $a = 0.083$ for $v \to 1$ with the direction of motion perpendicular to the plane of the baryon configuration, and $0.082 < a < 0.088$ for the case where the motion is parallel to the plane, again for $v \to 1$. In this last case, a is smallest for those quarks on the circle which are connected to the D5-brane junction at the center of the baryon by a string that is perpendicular to the direction of motion. The velocity dependence in (5.1) is precisely the same as that for the screening length defined by a quark and antiquark moving through the plasma, and even the weak angular dependence of a is strikingly similar. This is a confirmation of the robustness of the velocity dependence of screening that in the meson sector has as a consequence the experimentally testable prediction that in a range of temperatures that is plausibly accessed in heavy-ion collisions at RHIC (or at the LHC) J/Ψ (or Υ) suppression may set in only for quarkonia moving with a transverse momentum above some threshold [42]. In the baryon sector, it indicates that if baryons composed of three charm quarks are ever studied in heavy-ion collision experiments which do not reach such high temperatures as to dissociate them at rest, their production would also be suppressed above some threshold transverse momentum.

We have found that if the baryon configuration we study feels a wind velocity parallel to its plane (and presumably at any direction except perpendicular) the N_c quarks are not all equivalent. Those in a direction perpendicular to the wind are most affected by the wind velocity, as in the configuration we analyze with azimuthally symmetric boundary conditions at the D5-brane they are the ones that are pulled in

closest to the D5-brane and yet they are also the ones that have the smallest L_s. It is tempting to conclude from this that as a function of increasing v or T these quarks will dissociate first. However, justifying such a conclusion requires further work. It could be interesting to investigate configurations that are held circular in a wind parallel to their plane, which would no longer have azimuthally symmetric boundary conditions at the D5-brane. This would allow the analysis of a sequence of configurations with the same shape but different size rather than a sequence of configurations whose degree of squashing changes with size, as in our analysis. However, a definitive conclusion requires comparing the energies of a baryon configuration on the one hand with a well-separated quark and $(N_c - 1)$-quarks+D5-brane configuration, each trailing a dragging string, on the other hand. If the varying effectiveness of the screening of the potential binding different quarks to the baryon that we have found were to manifest itself as some quarks dissociating before others, as a function of increasing T or v, this would suggest that when heavy baryons with $N_c = 3$ dissociate while moving through a strongly coupled plasma, they may at least initially dissociate into a quark and a diquark.

Chapter 4

Strongly Coupled Plasmas - Synchrotron Radiation

4.1 Introduction and Outlook

The emission and propagation of radiation is an interesting and natural topic of study in any field theory. For localized sources, one is typically interested in the angular distribution and spectrum of radiation at spatial infinity and in deciphering how information about the source is encoded in it. This topic has been studied for more than a century within the realm of classical electrodynamics (for a textbook treatment, see [147]). It is much less studied in realms where quantum effects can be important, as for example in a nonabelian gauge theory in the limit of strong coupling. This has largely been due to the absence of strong coupling methods for studying real-time dynamics, which has recently become possible with the discovery of gauge/gravity duality [61]. Because of this, strongly coupled real-time phenomena in theories with gravitational duals have become accessible to reliable calculation.

To date, much of the analysis of real-time phenomena in gauge theories with dual gravitational descriptions has focused on systems at nonzero temperature. The reason for this, as we discussed in Chapter 1, is that these strongly coupled plasmas are more similar to the strongly coupled quark-gluon plasma of QCD being produced and studied in heavy-ion collision experiments at the Relativistic Heavy Ion Collider [7,

8, 9, 10] than the vacua of these gauge theories are to the vacuum of QCD. Asking how a test quark moving along some trajectory with nonzero acceleration radiates in vacuum in a strongly coupled nonabelian gauge theory is a simpler question than many of those that have already been studied at nonzero temperature. We shall answer this question for the specific case of a test quark in circular motion in the vacuum of $\mathcal{N} = 4$ SYM theory.

As we have discussed in Chapter 1, the two parameters of $\mathcal{N} = 4$ SYM theory are the number of colors N_c and the 't Hooft coupling $\lambda \equiv g_{YM}^2 N_c$ with g_{YM}^2 the gauge coupling and we shall work in the large N_c limit throughout. Since the theory is conformal, we can specify λ. If we choose $\lambda \to 0$, we can study the radiation using methods similar to those used in classical electrodynamics. If we choose $\lambda \to \infty$, the dual gravitational description of this strongly coupled nonabelian quantum field theory becomes the classical gravity limit of Type IIB string theory in the AdS$_5\times$S$_5$ spacetime. The geometry of the five-sphere will play no role in our computation — indeed it can be replaced by any compact five-dimensional space X_5. This means that our strong coupling results will be valid for all conformal quantum field theories with a dual classical gravity description — since conformality of the quantum theory maps onto the presence of an AdS$_5$ spacetime in the gravitational description.[1]

Because the vacuum of $\mathcal{N} = 4$ SYM theory is not similar to that of our world, studying the radiation of a test quark in circular motion in this theory does not have direct phenomenological motivation. However, we shall find that the angular distribution of the radiation is very similar to that of classic synchrotron radiation: when the quark is moving along its circle with an increasingly relativistic velocity, the radiation is produced in an increasingly tightly collimated beam — a beam which, if Fourier analyzed, contains radiation at increasingly short wavelengths and high frequencies. This is interesting first in its own terms and second with a view to

---

[1]Our results are valid for all strongly coupled conformal quantum field theories with a dual classical gravity description as long as we express our results in terms of the 't Hooft coupling λ in each of the conformal field theories. The relations between this parameter, N_c, and the parameters that specify the gravitational physics in the AdS$_5$ space — namely the string coupling and the dimensionless ratio of the square of the AdS curvature and the string tension — will be different in different conformal field theories, since these relations do depend on the geometry of X_5.

extending the calculation to nonzero temperature. First, from the point of view of the quantum field theory we do not understand why the angular distribution of the radiation that we find is almost the same at $\lambda \to \infty$ as it is at $\lambda \to 0$. Why should the pattern of radiation when what is radiated is nonabelian and strongly coupled be similar to that seen in classical electrodynamics? In this sense, our results come as something of a surprise to us. Second, our results in this formal setting nevertheless open the way to a new means of modelling jet quenching in heavy-ion collisions. If we were to add a nonzero temperature to our calculation, we could watch the tightly collimated beam of synchrotron radiation interact with the strongly coupled plasma that would then be present. The beam of radiation should be slowed down from the speed of light to the speed of sound and should ultimately thermalize, and it would be possible to study how the length- and time-scales for these processes depend on the wavelength and frequency of the beam.

We shall consider a test quark moving on a circle of radius R_0 with constant angular velocity ω_0. In spherical coordinates $\{r, \theta, \varphi\}$ we can take the quark's trajectory to be given by

$$r = R_0, \quad \theta = \frac{\pi}{2}, \quad \varphi = \omega_0 t \ . \tag{4.1}$$

By a test quark we mean a test charge in the fundamental representation of the $SU(N_c)$ gauge group. The total power radiated by this test quark moving in the vacuum of $\mathcal{N} = 4$ SYM theory in the large-N_c and strong coupling limit has been computed previously by Mikhailov in Ref. [148], who finds

$$P = \frac{\sqrt{\lambda}}{2\pi} a^2 \ , \tag{4.2}$$

where a is the quark's proper acceleration, given by

$$a = \gamma^2 v \omega_0 \ , \tag{4.3}$$

where the quark has speed

$$v = R_0 \omega_0 \tag{4.4}$$

111

and where

$$\gamma \equiv \frac{1}{\sqrt{1-v^2}} \tag{4.5}$$

is the standard Lorentz factor. Mikhailov observed that upon making the substitution

$$\sqrt{\lambda} \leftrightarrow \frac{e^2}{3} \tag{4.6}$$

the result (4.2) becomes identical to the Larmor result in classical electrodynamics. Furthermore, Mikhailov showed that the power radiated by a test quark moving along an *arbitrary* trajectory is identical to what Liénard calculated in 1898 [149] — see [147] for a textbook treatment — upon making the substitution (4.6). We shall go beyond Mikhailov's result by computing the distribution in space and time of the power radiated by the quark in circular motion. We shall not attempt Mikhailov's generalization to an arbitrary trajectory.

Before leaping to the conclusion that Mikhailov's result suggests that the $\mathcal{N} = 4$ SYM synchrotron radiation pattern will be similar to that in classical electrodynamics, consider the results in the literature that push one's intuition in the opposite direction. One interesting study related to zero temperature radiation was performed in Ref. [56], where decays of off-shell bosons in strongly coupled holographic conformal field theories were analyzed. (One can think of the off-shell boson as the virtual photon produced in electron-positron annihilation, with that photon coupling to matter in a strongly coupled conformal field theory instead of to quarks in QCD.) It was shown in Ref. [56] that there is no correlation between the boson's spin and the angular distribution of power radiated through the sphere at infinity. In other words, if one prepares a state containing an off-shell boson with definite spin, in the rest frame of the boson the event averaged angular distribution of power at infinity will always be isotropic. This stands in stark contrast to similar weak coupling calculations in QCD, where the boson's spin imprints a distinct "antenna" pattern in the distribution of power at infinity [150, 151, 152]. Similar behavior regarding the isotropization of radiation at strong coupling was also reported in Refs. [58, 57]. A natural question to ask when considering the results of Ref. [56] is where does the isotropization of

radiation come from? Is isotropization a characteristic of the particular initial states studied in Ref. [56] or is it a natural process which happens during the propagation of strongly coupled radiation? Indeed, it has been suggested in Ref. [58] that the mechanism responsible for the isotropization is that parton branching is not suppressed at strong coupling and, correspondingly, successive branchings can scramble any initially preferred direction in the radiation as it propagates out to spatial infinity. Regardless of mechanism, these calculations provide an example in which the pattern of radiation is very different in the strongly coupled $\mathcal{N} = 4$ SYM theory to that in weakly coupled QCD or QED. If the intuition about the emission and propagation of radiation derived from these calculations applies to radiation from an accelerated test charge, then, we should expect that in our strongly coupled nonabelian theory this radiation should isotropize and "branch", populating longer and longer wavelength modes as it propagates. We find nothing like this. The straightforward guess based upon Mikhailov's result — namely that synchrotron radiation in strongly coupled $\mathcal{N} = 4$ SYM theory should look like that in classical electrodynamics — turns out to be close to correct.

We shall analyze the angular distribution of power radiated by a rotating quark in $\mathcal{N} = 4$ SYM theory at both weak and strong coupling. Our weak coupling results are valid only in this theory. At strong coupling, we obtain an analytic expression for the energy density which is valid at all distances from the quark and for all holographic conformal field theories. At weak coupling our analysis reduces to that of synchrotron radiation in classical electrodynamics with an additional contribution coming from a scalar field [153]. At strong coupling gauge/gravity duality maps the problem onto that of the linear gravitational response due to the presence of a string.

Fig. 4-1 shows a cartoon of the classical 5d dual gravitational description. The five dimensional geometry of AdS_5, which is the arena where the dual gravitational dynamics takes place, has a four dimensional boundary whose geometry is that of ordinary Minkowski space. Ending at the boundary is a classical string whose endpoint follows a trajectory that corresponds to the trajectory of the quark in the dual field theory. The condition that the endpoint rotates about a specific (Minkowski space)

113
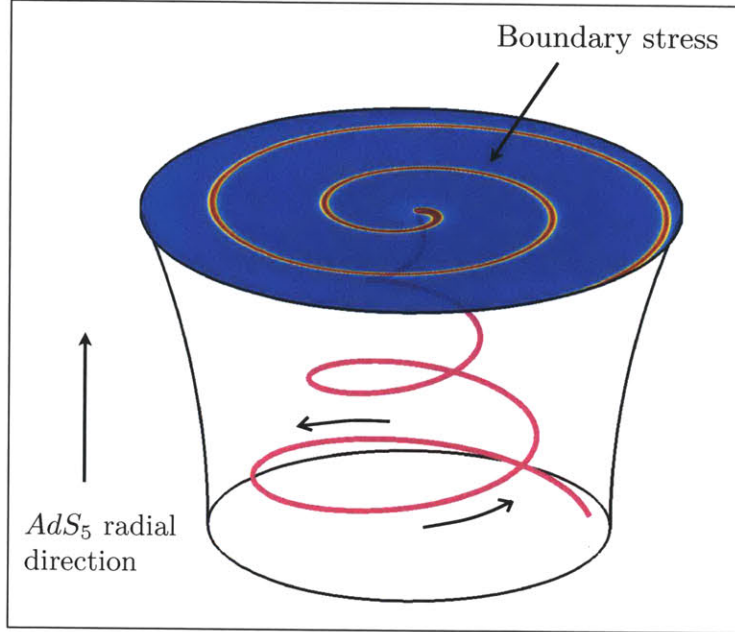
Figure 4-1: A cartoon of the gravitational description of synchrotron radiation at strong coupling. The arena where the gravitational dynamics takes place is the $5d$ geometry of AdS$_5$. A string resides in the geometry and an endpoint of the string is attached to the $4d$ boundary of AdS_5, which is where the dual quantum field theory lives. The trajectory of the endpoint of the string corresponds to the trajectory of the dual quark. Demanding that the endpoint rotates results in the string rotating and coiling around on itself as it extends in the AdS_5 radial direction. The presence of the string in turn perturbs the geometry and the near-boundary perturbation in the geometry induces a $4d$ stress tensor on the boundary. The induced stress has the interpretation as the expectation value of the stress tensor in the dual quantum field theory.

axis results in the entire string rotating about the same axis with the string coiling around on itself over and over. In turn, the rotating motion of the string creates gravitational radiation which propagates up to the boundary of the geometry. Just like electromagnetic fields induce surface currents on conductors, the gravitational disturbance near the boundary induces a $4d$ stress tensor on the boundary [154, 155]. As shown in Fig. 4-1, the induced $4d$ stress tensor inherits the coiled structure of the rotating string. Via the standard gauge/gravity dictionary [61, 156], the induced $4d$ stress tensor is the expectation value of the stress tensor in the dual quantum field theory. So, by doing a classical gravitational calculation in five dimensions (which happens to be somewhat analogous to a classical electromagnetic calculation) we can

compute the pattern of radiation in the boundary quantum field theory, including all quantum effects and working in a strong coupling regime in which quantum effects can be expected to dominate.

At both weak and strong coupling we find that the radiation pattern at infinity qualitatively resembles that of synchrotron radiation in classical electrodynamics. And, at both weak and strong coupling, for the case of relativistic circular motion we find the characteristic pattern of a lighthouse-like beam propagating out to infinity without broadening. As stated above, at weak coupling the difference between our results and those of classical electrodynamics simply amount to the presence of an additional contribution coming from a scalar field. At strong coupling both the total power and the angular distribution of power are found to differ somewhat from that obtained by extrapolating the weak coupling result to strong coupling. Interestingly, though, the angular distribution of power at strong coupling can be written as the sum of the angular distributions of power coming from vector and scalar modes at weak coupling with 2:1 relative strengths, whereas at weak coupling this ratio is 4:1. As the radiation is far from isotropic at infinity, this problem provides a concrete example demonstrating that radiation need not isotropize in a nonabelian gauge theory at strong coupling. And, the width of the outgoing pulse of radiation does not broaden as the pulse propagates outward, meaning that as it propagates out to infinity the radiation remains at the (short) wavelengths and (high) frequencies at which it was emitted.

We close this introduction with a look ahead at extending this calculation to nonzero temperature T. The authors of Ref. [157] have shown that the power that it takes to move the quark in a circle is given by the vacuum result (4.2) even for a test quark moving through the strongly coupled plasma present at $T \neq 0$ as long as

$$\omega_0^2 \gamma^3 \gg \pi^2 T^2 \ . \tag{4.7}$$

In the opposite regime, where $\omega_0^2 \gamma^3 \ll \pi^2 T^2$, the power it takes to move the quark in a circle through the plasma is the same as it would be to move the quark in a straight line

with speed v. This power has been computed using gauge/gravity duality in Refs. [83, 84], and corresponds to pushing the quark against a drag force. The analogue of our calculation — namely following where the dissipated or "radiated" power goes — was done, again using gauge/gravity duality, in Refs. [158, 159, 160, 161]. There, it was demonstrated that the test quark plowing through the strongly coupled plasma in a straight line excites hydrodynamic modes of the plasma, trailing a diffusion wake and — if the motion is supersonic — creating a Mach cone. It is a generic feature of a nonzero temperature plasma, at weak coupling or at strong coupling, that any power dumped into it in some localized fashion must eventually take the form of hydrodynamic excitations [161]. These considerations and our results motivate the extension of the present calculation to nonzero temperature, in particular in the regime (4.7). At these high velocities or low temperatures, we know that (4.2) is satisfied and, given our experience at zero temperature in this Chapter, we therefore expect that at length scales that are small compared to $1/T$ the rotating quark radiates a narrow beam of synchrotron radiation, even at strong coupling. If (4.7) is satisfied, the wavelengths characterizing the pulse of radiation heading outward into the plasma are much shorter than $1/T$. But, we also know on general grounds that this narrow pulse of beamed radiation must first reach local thermal equilibrium, likely converting into an outgoing hydrodynamic wave moving at the speed of sound, and must then ultimately dissipate and thermalize completely. Watching these processes occur may give insight into jet quenching in the strongly coupled quark-gluon plasma of QCD.

The outline of the rest of this Chapter is simple: we do the weak coupling calculation in Section 4.2 and use gauge/gravity duality to do the strong coupling calculation in Section 4.3. In Section 4.4 we discuss the results and conclude.

4.2 Weak coupling calculation

In the limit of weak coupling, the radiation produced by an accelerated test charge can be analyzed using classical field theory. For example, for the case of an electron

116

undergoing synchrotron motion in QED, the appropriate classical effective description is simply that of classical electrodynamics. For the case of a test quark (specifically, an infinitely massive spin-1/2 particle from the $\mathcal{N} = 2$ hypermultiplet that is in the fundamental representation of the $SU(N_c)$ gauge group) moving through the vacuum of $\mathcal{N} = 4$ SYM theory, more fields can be excited and the appropriate effective classical description is more complicated. The Lagrangian for this theory can be found, for example, in Ref. [162]. As can readily be verified by inspecting the field theory Lagrangian, in the limit of asymptotically weak coupling and large test quark mass the fields that can be excited by the test quark are the non-Abelian gauge field and an adjoint representation scalar field. Interactions with all other fields are either suppressed by an inverse power of the quark mass or a positive power of the 't Hooft coupling λ. Moreover, in the limit of asymptotically weak coupling the gauge and scalar fields satisfy decoupled linear equations of motion.

Following Ref. [153], instead of dealing with N_c^2 decoupled components of the gauge field and N_c^2 decoupled components of the adjoint scalar field, we consider the case of a single $U(1)$ gauge field and a single real scalar field with appropriate effective couplings tailored to compensate for the fact that the actual theory contains adjoint representation fields. The effective couplings can be determined by computing the vector and scalar contributions to the Coulomb field of a quark in the effective description and matching onto the full theory. In the large N_c limit the classical effective Lagrangian reads [153]

$$\mathcal{L}_{\text{classical}} = -\frac{1}{4}F_{\mu\nu}F^{\mu\nu} - J \cdot A - \frac{1}{2}(\partial\chi)^2 - \rho_{\text{charge}}\chi \,, \tag{4.8}$$

where $F^{\mu\nu}$ is the field strength corresponding to the $U(1)$ gauge field A^μ, χ is the scalar field, and the sources corresponding to the test quark are given by

$$\rho_{\text{charge}} = e_{\text{eff}}\sqrt{1 - v^2}\delta^3(\boldsymbol{r} - \boldsymbol{r}_{\text{quark}}) \,, \tag{4.9}$$

$$J^\mu = e_{\text{eff}}\frac{dr^\mu_{\text{quark}}}{dt}\delta^3(\boldsymbol{r} - \boldsymbol{r}_{\text{quark}}) \,, \tag{4.10}$$

with r^μ_{quark} the trajectory of the test quark, $v = \dot{r}^2_{\text{quark}}$ the velocity of the test quark, and where it turns out that both effective couplings take on the same value

$$e^2_{\text{eff}} = g^2 \frac{N_c^2 - 1}{2N_c} \simeq \frac{1}{2}\lambda. \tag{4.11}$$

In classical electrodynamics, $\rho_{\text{charge}} = 0$ and, in the source for the vector field J^μ, e_{eff} is just e. We shall take the trajectory of the test quark to be (4.1) throughout.

4.2.1 Solutions to the equations of motion and the angular distribution of power

Comprehensive analyses of the radiation coming from the gauge field can be found in classical electrodynamics textbooks (see for example [147]). However, because the case of scalar radiation is less well known and also for the sake of completeness, we present a brief analysis of the radiation for both fields. We shall linger in our discussion on those aspects which will also be of value in the analysis of our strong coupling results.

Choosing the Lorentz gauge $\partial \cdot A = 0$, the equations of motion for the fields read

$$-\partial^2 A^\mu = J^\mu, \quad -\partial^2 \chi = \rho_{\text{charge}}. \tag{4.12}$$

These equations are solved by

$$A^\mu(t, \boldsymbol{r}) = \int d^4 r' G(t-t', \boldsymbol{r}-\boldsymbol{r}') J^\mu(t', \boldsymbol{r}'), \tag{4.13a}$$

$$\chi(t, \boldsymbol{r}) = \int d^4 r' G(t-t', \boldsymbol{r}-\boldsymbol{r}') \rho_{\text{charge}}(t', \boldsymbol{r}'), \tag{4.13b}$$

where

$$G(t-t', \boldsymbol{r}-\boldsymbol{r}') = \frac{\theta(t-t')}{4\pi|\boldsymbol{r}-\boldsymbol{r}'|} \delta(t - t' - |\boldsymbol{r}-\boldsymbol{r}'|) \tag{4.14}$$

is the retarded Greens function of $-\partial^2$, and $(t', \boldsymbol{r}')$ is the point of emission. After

using delta functions to carry out the r'^μ integrations, we arrive at the expressions

$$A^\mu = \frac{e_{\text{eff}}}{4\pi r} \frac{1}{\Xi(t', \boldsymbol{r})} \frac{dr^\mu_{\text{quark}}}{dt'}\bigg|_{t'=t_{\text{ret}}} , \tag{4.15a}$$

$$\chi = \frac{e_{\text{eff}}}{4\pi r} \frac{1}{\Xi(t', \boldsymbol{r})} \frac{1}{\gamma}\bigg|_{t'=t_{\text{ret}}} , \tag{4.15b}$$

where

$$\Xi(t', \boldsymbol{r}) \equiv \frac{|\boldsymbol{r}-\boldsymbol{r}_{\text{quark}}(t')| - \boldsymbol{r} \cdot \dot{\boldsymbol{r}}_{\text{quark}}(t')}{r} , \tag{4.16}$$

$\gamma = 1/\sqrt{1-v^2}$, $r = |\boldsymbol{r}|$, and the retarded time t_{ret} is the solution to

$$t - t_{\text{ret}} - |\boldsymbol{r} - \boldsymbol{r}_{\text{quark}}(t_{\text{ret}})| = 0 . \tag{4.17}$$

$(t - t_{\text{ret}})$ is the light travel time between $\boldsymbol{r}_{\text{quark}}(t_{\text{ret}})$ and $\boldsymbol{r}$. Because the motion of the quark is periodic, $\boldsymbol{r}_{\text{quark}}(t_{\text{ret}})$ is a periodic function of its argument with period $2\pi/\omega_0$. Eq. (4.17) then implies that if t is shifted by $2\pi/\omega_0$, t_{ret} shifts by the same amount so that $(t-t_{\text{ret}})$ is left unchanged. Because the motion of the quark is circular, Eq. (4.17) also implies that a change in the position of the quark corresponding to a shift in its azimuthal angle by $\delta\varphi$ is equivalent to a shift in both t and t_{ret} by $\delta\varphi/\omega_0$.

We now describe the qualitative behavior of the solutions (4.15). Fig. 4-2 shows a pictorial representation of the solutions (4.15). As the quark moves along its circular trajectory, it emits radiation in the direction of its velocity in a narrow cone of angular width α. From the solutions (4.15) it can be shown that in the large γ limit α scales like $\alpha \sim 1/\gamma$ for both the scalar and vector radiation. The cone of radiation emitted at each time propagates outwards at the speed of light. At any one moment in time, the radiation emitted at all times in the past forms a spiral, as illustrated by the red spiral sketched in Fig. 4-2. Clearly, the radial width Δ of the spiral must go to zero as $\alpha \to 0$, namely as $\gamma \to \infty$. As we illustrate in Fig. 4-3, in the large γ limit the radial width scales like $\Delta \sim 1/\gamma^3$. To understand the scaling of Δ, consider an observer at the point p in Fig. 4-3. As the quark moves along its trajectory, an observer at p will see a short pulse of radiation of duration $\Delta t \sim R_0\alpha/v$. The leading edge of the pulse will be emitted by the quark at time t_1 and the trailing edge will be emitted at time
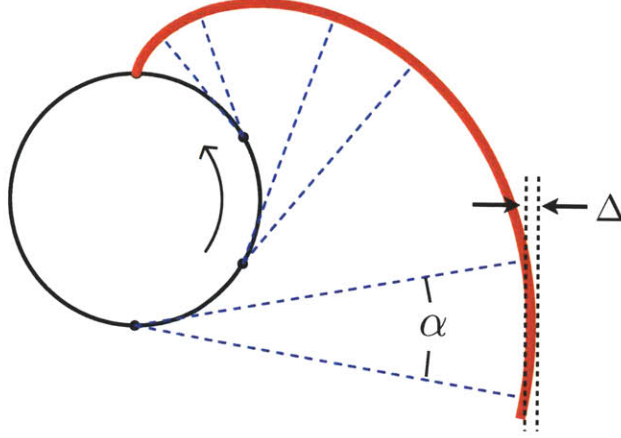
Figure 4-2: A sketch of the solutions (4.15). As the quark moves along its circular trajectory, it emits radiation in a narrow cone of angular width $\alpha \sim 1/\gamma$ in the direction of its velocity vector. The diagram is a snapshot at the time when the quark is at the top of the circle. The red spiral shows where the radiation emitted at earlier times is located at the time of the snapshot. The width Δ of the spiral scales like $\Delta \sim 1/\gamma^3$, as explained in Fig. 4-3.

$t_2 = t_1 + R_0\alpha/v$. At time t_2 the radiation emitted at t_1 will have traveled a distance $R_0\alpha/v$ towards p. Moreover, the chordal distance between the two emission points is approximately $R_0\alpha$ when α is small. It therefore follows that the spatial thickness Δ of the pulse observed at p scales like

$$\Delta \sim (R_0\alpha/v - R_0\alpha) \sim R_0\alpha/\gamma^2 \sim R_0/\gamma^3 . \tag{4.18}$$

We note that the fact that Δ and α scale with different powers of γ is a consequence of the fact that the radiation is emitted in the direction of the quark's velocity. If the radiation were emitted in any other direction, Δ and α would have the same γ scaling. Because we will re-use these arguments in the analysis of our strong coupling results, it is important to note that they are purely geometrical, relying only on the fact that the radiation travels at the speed of light and the fact that the outward going pulse of radiation propagates without broadening, maintaining the spiral shape whose origin we have illustrated.

In addition to determining how the pulse widths α and Δ are related, these geometrical considerations in fact specify the location of the spiral of radiation precisely.
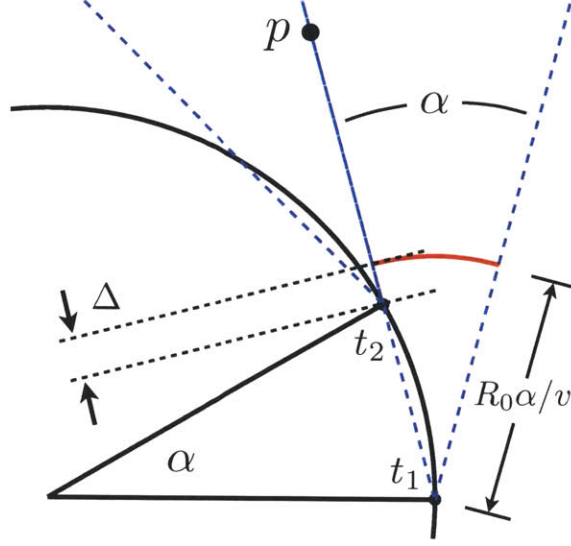
Figure 4-3:   A close-up illustration of the emission of radiation at two times t_1 and t_2. The radiation is emitted in the direction of the quark's velocity vector, within a cone of angular width α. An observer at the point p is illuminated by a pulse of radiation of duration $\Delta t \sim R_0 \alpha$ and of spatial thickness Δ. The leading edge of the pulse observed at p is emitted at t_1 and the trailing edge observed at p is emitted at t_2. At time t_2 the radiation emitted at t_1, denoted by the solid red line, has traveled a distance $R_0 \alpha / v$ towards p. The chordal distance between the two emission points is $R_0 \alpha$ in the $\alpha \to 0$ limit. The width Δ is therefore $\Delta = R_0 \alpha (1/v - 1)$.

For a quark moving in a circle of radius R_0 in the (x_1, x_2) plane, at the time at which the quark is located at $(x_1, x_2) = (R_0, 0)$ the spiral of energy density radiated at all times in the past is centered on a curve in the $x_3 = 0$ plane specified by

$$x_1 = R_0 \left[\cos \tilde{\rho} + \frac{\tilde{\rho}}{v} \sin \tilde{\rho} \right] , \quad x_2 = R_0 \left[-\sin \tilde{\rho} + \frac{\tilde{\rho}}{v} \cos \tilde{\rho} \right] , \tag{4.19}$$

where $\tilde{\rho}$ is a parameter running from 0 to ∞. At large r, this spiral can equivalently be written

$$\varphi(r, t) = \frac{\pi}{2} + \omega_0 t - \frac{rv}{R_0} + \mathcal{O}(1/r) \tag{4.20}$$

in spherical coordinates, where we have also added the t-dependence.

Recall that the γ-scaling of Δ depended on the fact that the radiation is emitted tangentially, in the direction of the velocity vector of the quark. The same is true for the shape of the spiral. For example, if we repeat the geometrical analysis for a hypothetical case in which the quark emits a narrow cone of radiation in the $\hat{r}$ direc-

tion, perpendicular to its direction of motion, the energy density would be centered on a different spiral specified by

$$x_1 = R_0 \left[1 + \frac{\tilde{\rho}}{v}\right] \cos \tilde{\rho}, \ \ x_2 = -R_0 \left[1 + \frac{\tilde{\rho}}{v}\right] \sin \tilde{\rho}. \tag{4.21}$$

This spiral, including its t-dependence, is given in spherical coordinates by

$$\varphi(r, t) = v + \omega_0 t - \frac{rv}{R_0}, \tag{4.22}$$

which differs from the correct spiral of Eqs. (4.19) and (4.20) by a phase shift at large r. If the quark emits radiation perpendicular to its direction of motion, a distant point p would be illuminated by light emitted when the quark was at the closest point on its circle to p, whereas for the correct spiral (4.19) the light seen at p was emitted one quarter of a period earlier but had travelled R_0 farther, leading to the phase shift of $(-\pi/2 + v)$. In the near zone, (4.21) differs from the correct spiral (4.19) in shape, not just by a phase shift.

In Section 4.4, we shall compare our results at strong coupling to those we have obtained in this Section via geometrical arguments built upon the fact that the outward going pulse of radiation propagates without spreading.

We now analyze the far zone behavior of the fields and compute the time-averaged angular distribution of power. In particular, we wish to compute the angular distribution of power radiated through the sphere at $r = \infty$ averaged over one cycle of the quark's motion. Denoting the energy flux by $\boldsymbol{S}$, the time averaged angular distribution of power is given by

$$\frac{dP}{d\Omega} = \frac{\omega_0}{2\pi} \lim_{r \to \infty} r^2 \int_0^{\frac{2\pi}{\omega_0}} dt_{\text{ret}} \frac{\partial t}{\partial t_{\text{ret}}} \hat{r} \cdot \boldsymbol{S}, \tag{4.23}$$

where, from Eqs. (4.17) and (4.16),

$$\frac{\partial t}{\partial t_{\text{ret}}} = \frac{r\Xi}{t - t_{\text{ret}}}. \tag{4.24}$$

122

(Technically, the integration in Eq. (4.23) should run from $t_{\text{ret}} = c$ to $t_{\text{ret}} = c + 2\pi/\omega_0$ where $c \sim -r$. This is simply because in the far-zone limit the retarded time always scales like $t_{\text{ret}} \sim -r$. However, as the motion of the quark is periodic one can always shift the integration variable so that the integration runs from 0 to $2\pi/\omega_0$.)

For the simple case of scalar or electromagnetic fields, the computation of the energy flux directly from the fields is relatively simple. However, in the gravitational setting discussed below, the computation of the energy flux requires solving three differential equations whereas the computation of the energy density requires only solving one. Therefore, if possible, it is useful to extract the angular distribution of power from the energy density alone.

For a conformal theory at zero temperature the far-zone energy density and flux associated with a localized source must take the form

$$\mathcal{E}(t, \boldsymbol{r}) = \frac{\varepsilon(t_{\text{ret}}, \theta, \varphi)}{r^2}, \quad \boldsymbol{S}(t, \boldsymbol{r}) = \frac{s(t_{\text{ret}}, \theta, \varphi)}{r^2}\hat{r}, \quad (4.25)$$

up to $O(1/r^3)$ corrections. Moreover, using the continuity equation and the fact that $\partial t_{\text{ret}}/\partial t = -\partial t_{\text{ret}}/\partial r$ in the far zone, it is easy to see that we must have $\varepsilon = s$. In terms of ε, the time-averaged angular distribution of power reads

$$\frac{dP}{d\Omega} = \frac{\omega_0}{2\pi} \int_0^{\frac{2\pi}{\omega_0}} dt_{\text{ret}} \frac{\partial t}{\partial t_{\text{ret}}}\varepsilon. \quad (4.26)$$

We see from Eq. (4.26) that we can extract the angular distribution of the radiated power at infinity by analyzing the asymptotic behavior of the energy density.

The energy density associated with the vector field is $\mathcal{E}_{\text{vector}} = \frac{1}{2}(\boldsymbol{E}^2 + \boldsymbol{B}^2)$ where $\boldsymbol{E}$ and $\boldsymbol{B}$ are the electric and magnetic fields. The energy density associated with the scalar is $\mathcal{E}_{\text{scalar}} = \frac{1}{2}(\nabla\chi)^2$. Evaluating these quantities for the solutions (4.15) in

the $r \to \infty$ limit yields

$$\mathcal{E}_{\text{vector}} = \frac{e_{\text{eff}}^2 v^2 \omega_0^2}{32\pi^2 r^2 \tilde{\xi}^6} \Big[3 + 2v^2 + \left(1 - 2v^2\right) \cos 2\theta - 8v \sin\theta \sin(\varphi - \omega_0 t_{\text{ret}})$$

$$- 2\sin^2\theta \cos\left(2(\varphi - \omega_0 t_{\text{ret}})\right) \Big], \tag{4.27a}$$

$$\mathcal{E}_{\text{scalar}} = \frac{e_{\text{eff}}^2 v^2 \omega_0^2}{32\pi^2 \gamma^2 r^2 \tilde{\xi}^6} \sin^2\theta \cos^2(\varphi - \omega_0 t_{\text{ret}}), \tag{4.27b}$$

up to subleading corrections proportional to $1/r^3$, where we have defined

$$\tilde{\xi} \equiv 1 - v\sin\theta \sin(\varphi - \omega_0 t_{\text{ret}}), \tag{4.28}$$

which is the $r \to \infty$ limit of Ξ:

$$\Xi = \tilde{\xi} + \mathcal{O}(1/r). \tag{4.29}$$

Note that the energy densities (4.27) are proportional to $1/\tilde{\xi}^6$ and therefore have maxima in the $\theta = \pi/2$ plane where $\tilde{\xi}$ has minima; at large r, these occur on the spiral (4.20).

Noting from (4.17) that $(t - t_{\text{ret}}) \sim r$ in the $r \to \infty$ limit, we see from (4.24) and (4.29) that $\partial t / \partial t_{\text{ret}} = \tilde{\xi}$ in the $r \to \infty$ limit. We can now evaluate the expression (4.26) for the time-averaged angular distribution of power, yielding

$$\frac{dP_{\text{vector}}}{d\Omega} = \frac{v^2 \gamma^3 \omega_0^2 e_{\text{eff}}^2}{128\pi^2} \frac{(7\gamma^2 - 3)\sin^4\theta + 3\gamma^4 \sin^2(2\theta) + 8\gamma^4 \cos^4\theta}{\left(\gamma^2 \cos^2\theta + \sin^2\theta\right)^{7/2}}, \tag{4.30a}$$

$$\frac{dP_{\text{scalar}}}{d\Omega} = \frac{v^2 \gamma^3 \omega_0^2 e_{\text{eff}}^2}{512\pi^2} \frac{\sin^2\theta \left[9\gamma^2 - 1 - v^2\gamma^2 \cos(2\theta)\right]}{\left(\gamma^2 \cos^2\theta + \sin^2\theta\right)^{7/2}}. \tag{4.30b}$$

Eqs. (4.30) show that the power radiated in vectors and in scalars are both focused about $\theta = \pi/2$ with a characteristic angular width $\delta\theta \propto 1/\gamma$. We shall plot the sum $dP_{\text{vector}}/d\Omega + dP_{\text{scalar}}/d\Omega$ in Section 4.4, where we compare this weak coupling result to that obtained at strong coupling.

Integrating Eqs. (4.30) over all solid angles we find the power radiated in vectors

and scalars

$$P_{\text{vector}} = \frac{2}{3}\frac{e_{\text{eff}}^2}{4\pi}a^2 \,, \tag{4.31a}$$

$$P_{\text{scalar}} = \frac{1}{6}\frac{e_{\text{eff}}^2}{4\pi}a^2 \,, \tag{4.31b}$$

where $a = v\omega_0/(1 - v^2)$ is the proper acceleration of the test quark. With $e_{\text{eff}} = e$, Eq. (4.31a) becomes the well known Larmor formula for the power radiated by an accelerated charge in classical electrodynamics. Evidently, at weak coupling four times as much energy is radiated into the vector mode as the scalar mode. We now see that Mikhailov's strong coupling result (4.2) is equivalent to the result for weakly coupled $\mathcal{N} = 4$ SYM theory upon making the substitution

$$\sqrt{\lambda} \leftrightarrow \frac{5}{12}e_{\text{eff}}^2 \,, \tag{4.32}$$

with the difference between this result and (4.6) — which was obtained by comparing the strong coupling $\mathcal{N} = 4$ SYM result to classical electrodynamics — coming from the fact that in weakly coupled $\mathcal{N} = 4$ SYM theory the rotating test quark radiates scalars as well as vectors.

4.3 Gravitational Description and Strong Coupling Calculation

In this Section we will use the gauge/gravity duality [61] in order to calculate the power radiated by the rotating quark at strong coupling. As we discussed in Chapters 1 and 3, the AdS/CFT correspondence provides a description of the (strongly coupled; quantum mechanical) vacuum of $\mathcal{N} = 4$ SYM theory in $N_c \to \infty$ and $\lambda \to \infty$ limit in terms of classical gravity in the $\text{AdS}_5 \times S_5$ spacetime. Since generalizing from $\mathcal{N} = 4$ SYM to any other conformal quantum field theory that has a classical gravity dual involves replacing the S_5 by some other compact five-dimensional space (see Section 4.1), in what follows, we shall never need to specify this five-dimensional

space, meaning that all our strong coupling results will be valid for any large-N_c conformal field theories with gravitational duals.

In the coordinate system used in this Chapter, the metric of the AdS$_5$ spacetime is

$$ds^2 = \frac{R_{AdS}^2}{u^2} \left[-f\,dt^2 + dr^2 + \frac{du^2}{f} \right] , \tag{4.33}$$

where R_{AdS} is the AdS_5 curvature radius, u is the (inverse) AdS_5 radial coordinate with the boundary at $u = 0$, and $f = 1$. (We have kept the factor of f in the metric in order to generalize some of our calculations to nonzero temperature, where

$$f = 1 - \frac{u^4}{u_h^4} \tag{4.34}$$

with $u_h = 1/(\pi T)$ and T the temperature of the field theory state.) A single test quark in the fundamental representation in the field theory corresponds in the gravitational description to an open string with one endpoint attached to the boundary at $u = 0$. Taking the $N_c \rightarrow \infty$ and $\lambda \rightarrow \infty$ limits eliminates fluctuations of the string and makes the probability for loops to break off the string vanish. Upon taking these limits, the string is therefore a classical object. The presence of the classical string hanging "down" into the five-dimensional bulk geometry perturbs that geometry via Einstein's equations, and the behavior of the metric perturbation near the boundary encodes the change in the boundary stress tensor. This is illustrated in Fig. 4-1, and in this Section we shall turn this cartoon into calculation.

4.3.1 The rotating string

We begin by describing the rotating string. The metric perturbations that this string creates are small in the large N_c limit, small enough that we can neglect their back reaction on the shape of the string itself. We can therefore begin by finding the shape of the rotating string in AdS$_5$, in the absence of any metric perturbations. The

dynamics of classical strings are governed by the Nambu-Goto action

$$S_{\text{NG}} = -T_0 \int d\tau \, d\sigma \sqrt{-g} \,, \tag{4.35}$$

where $T_0 = \sqrt{\lambda}/2\pi R_{AdS}^2$ is the string tension, σ and τ are the coordinates on the worldsheet of the string, and $g = \det g_{ab}$ where g_{ab} is the induced worldsheet metric. The string profile is determined by a set of embedding functions $X^M(\tau, \sigma)$ that specify where in the spacetime described by the metric G_{MN} the point (τ, σ) on the string worldsheet is located. The induced world sheet metric is given in terms of these functions by

$$g_{ab} = \partial_a X \cdot \partial_b X \,, \tag{4.36}$$

where a and b each run over (τ, σ). For the determinant we obtain

$$-g = (\partial_\tau X \cdot \partial_\sigma X)^2 - (\partial_\tau X)^2 (\partial_\sigma X)^2 \,. \tag{4.37}$$

We choose worldsheet coordinates $\tau = t$ and $\sigma = u$. As we are interested in quarks which rotate at constant frequency ω_0 about the $\hat{z}$ axis, we parametrize the string embedding functions via

$$X^M(t, u) = (t, \boldsymbol{r}_s(t, u), u) \,, \tag{4.38}$$

where in spherical coordinates $\{r, \theta, \varphi\}$ the three-vector $\boldsymbol{r}_s$ is given by

$$\boldsymbol{r}_s(t, u) \equiv \left(R(u), \tfrac{\pi}{2}, \phi(u) + \omega_0 t \right) \,. \tag{4.39}$$

The function $\phi(u)$ describes how the purple string in Fig. 4-1 winds in azimuthal angle as a function of "depth" in the AdS$_5$ radial direction, whose coordinate is u. The function $R(u)$ describes how the string in Fig. 4-1 spreads outward as a function of depth. Because we are describing a situation in which the test quark at the boundary has been rotating on its circle for all time, the purple string in Fig. 4-1 is rotating at all depths with the same angular frequency ω_0, meaning that the two functions $R(u)$ and $\phi(u)$ in the parametrization (4.39) fully specify the shape of the rotating string

at all times. With this parameterization, the Nambu-Goto action reads

$$S_{\mathrm{NG}} = -\frac{\sqrt{\lambda}}{2\pi} \int dt\, du\, \mathcal{L}, \qquad (4.40)$$

where

$$\mathcal{L} = \frac{\sqrt{(1 - \omega_0^2 R^2)(1 + R'^2) + R^2 \phi'^2}}{u^2}. \qquad (4.41)$$

To determine the shape of the string in Fig. 4-1, we must extremize (4.40).

The equations of motion for $\phi(u)$ and $R(u)$ follow from extremizing the Nambu-Goto action (4.40). One constant of motion can be obtained by noting that the action is independent of $\phi(u)$. This implies that

$$\Pi \equiv -\frac{\partial \mathcal{L}}{\partial \phi'} \qquad (4.42)$$

is constant. Here and throughout, by $'$ we mean $\partial/\partial u$. The minus sign on the right-hand side of (4.42) is there in order to make Π positive for positive ω_0. In terms of Π, the equation of motion for $\phi'(u)$ reads

$$\phi'^2 = \frac{u^4 \Pi^2 (1 - \omega_0^2 R^2)(1 + R'^2)}{R^2 (R^2 - u^4 \Pi^2)}. \qquad (4.43)$$

The equation of motion for $R(u)$ is given by

$$\frac{\partial \mathcal{L}}{\partial R} - \frac{\partial}{\partial u} \frac{\partial \mathcal{L}}{\partial R'} = 0. \qquad (4.44)$$

Taking the above partial derivatives of $\mathcal{L}$ and then eliminating ϕ derivatives via Eq. (4.43), we obtain the following equation of motion:

$$R'' + \frac{R(u + 2RR')(1 + R'^2)}{u(u^4 \Pi^2 - R^2)} + \frac{1 + R'^2}{R(1 - \omega_0^2 R^2)} = 0. \qquad (4.45)$$

As a second order differential equation, one might expect that Eq. (4.45) requires two initial conditions for the specification of a unique solution. However, it was shown in Ref. [157] that this is not the case — together, Eqs. (4.43) and (4.45) imply that

all required initial data for (4.45) is fixed in terms of Π and ω_0. To see how this comes about note that Eq. (4.45) is singular when $1 - \omega_0^2 R^2 = 0$ or when $R^2 - u^4\Pi^2 = 0$. In order to maintain the positivity of the right hand side of Eq. (4.43), $1 - \omega_0^2 R^2$ and $R^2 - u^4\Pi^2$ must vanish at the same point. This happens where

$$u = u_c \equiv \frac{1}{\sqrt{\Pi\omega_0}}, \quad R = R_c \equiv \frac{1}{\omega_0}. \tag{4.46}$$

We can then solve (4.45) in the vicinity of $u = u_c$ by expanding $R(u)$ as

$$R(u) = R_c + R_c'(u - u_c) + \frac{1}{2}R_c''(u - u_c)^2 + \dots, \tag{4.47}$$

where $R_c^{(n)} \equiv \partial_u^n R|_{u=u_c}$. The second and third terms in (4.45) are divergent at $u = u_c$ while the R'' term is finite there. This means that when we substitute (4.47) into (4.45) and collect powers of $(u-u_c)$, we obtain an equation for R_c' that does not involve R_c'', meaning that the equation of motion itself determines R_c'. A short calculation yields

$$R_c' = \frac{1}{2}\left[\sqrt{\frac{\omega_0}{\Pi} + 4} - \sqrt{\frac{\omega_0}{\Pi}}\right]. \tag{4.48}$$

Therefore, both R_c and R_c' are determined by ω_0 and Π and consequently, for given ω_0 and Π there is only one solution to Eq. (4.45). From the perspective of the boundary field theory this had to happen: for a given angular frequency ω_0, the radiation produced by the rotating quark can only depend on the radius R_0 of the quark's trajectory (which as we will see below can be related to Π).

With the above point in mind, the unique solution to Eq. (4.45) is given by[2]

$$R(u) = \sqrt{v^2\gamma^2 u^2 + R_0^2}, \tag{4.49}$$

where $v = R_0\omega_0$ is the velocity of the quark and $\gamma = 1/\sqrt{1 - v^2}$. The velocity of the quark is related to Π via

$$\Pi = v^2\gamma^4\omega_0. \tag{4.50}$$

---

[2] One way to derive the solution (4.49) is simply to solve Eq. (4.45) with the series expansion (4.47) and recognize the resulting series as that of (4.49).

With $R(u)$ given by (4.49), it is easy to integrate Eq. (4.43). Taking the negative root of Eq. (4.43) so that the string trails its $u = 0$ endpoint, we find

$$\phi(u) = -u\gamma\omega_0 + \arctan(u\gamma\omega_0) \tag{4.51}$$

and thus

$$\varphi(t, u) = \omega_0(t - \gamma u) + \arctan(u\gamma\omega_0) . \tag{4.52}$$

We thus have an analytic description of the shape of the rotating string.

We can obtain the profile of the rotating string projected onto the plane at the boundary by using (4.49) to eliminate u from (4.52), yielding

$$\varphi(t, r) = \omega_0 t - \sqrt{\frac{r^2}{R_0^2} - 1} + \arctan\left(\sqrt{\frac{r^2}{R_0^2} - 1}\right) . \tag{4.53}$$

In the limit of $r \gg R_0$, we have

$$\varphi(t, r) = \omega_0 t + \frac{\pi}{2} - \frac{r}{R_0} + \mathcal{O}(1/r) . \tag{4.54}$$

Equation (4.54) describes a spiral whose neighboring circles (at fixed t) are separated by $2\pi R_0$. Note that the curve (4.54) is the same spiral as (4.20) when the velocity of the quark is $v \to 1$. Indeed, it can also be shown that at all radii (4.53) is the same spiral as (4.19) with $v = 1$. We conclude that for $v \to 1$ the rotating string hanging down into the AdS_5 metric is lined up precisely below the spiral in the boundary theory where the radiated synchrotron energy density is located, in electrodynamics, in the weak coupling calculation of Section 4.2 and, we shall see below, at strong coupling.[3] At velocities less than 1, the shape of the rotating string is not related to

---

[3] This identification suggests interesting possibilities at nonzero temperature. Whereas at $T = 0$ the rotating string has a profile $R(u)$ such that it extends out to infinite r, when $T \neq 0$ the rotating string only extends out to some finite maximum radius r_{max} that depends on ω_0 and v [157]. The fact that at zero temperature we can identify the the spiral of the rotating string with the spiral of energy density in the boundary quantum field theory suggests that, at least at $v \to 1$, the maximum radius out to which the rotating string reaches may be some length scale related to how far the beam of synchrotron radiation can travel through the hot strongly coupled plasma before it thermalizes. Interestingly, if one takes the $v \to 1$ at fixed R_0, one finds $r_{max} \to \infty$ [157].

the shape of the spiral of energy density, at least not directly by projection.

The shape of the rotating string determines the total power radiated, as we now explain. The string has an energy density π_0^0 and energy flux π_0^1, where

$$\pi_M^a \equiv \frac{\delta S_{\mathrm{NG}}}{\delta(\partial_a X^M)} \tag{4.55}$$

with S_{NG} given in (4.35), which satisfy

$$\partial_t \pi_0^0 + \partial_u \pi_0^1 = 0 . \tag{4.56}$$

This is simply the statement of energy conservation on the string worldsheet. The energy flux down the rotating string is given by

$$-\pi_0^1 = \frac{\sqrt{\lambda}}{2\pi} \omega_0 \Pi = \frac{\sqrt{\lambda}}{2\pi} \frac{1}{u_c^2} = \frac{\sqrt{\lambda}}{2\pi} a^2 , \tag{4.57}$$

where we have used (4.50) and where $a = v\omega_0\gamma^2$ is the proper acceleration of the test quark, and where the minus sign comes from our choice of parametrization of the world sheet with a coordinate u that increases downward, away from the boundary. The energy flux down the string is the energy that must be supplied by the external agent which moves the test quark in a circle; by energy conservation, therefore, it is the same as the total power radiated by the quark.[4] Thus far, we have reproduced

---

[4] The energy loss rate (4.57) can also be derived from the energy density along the string

$$-\pi_0^0 = \frac{\sqrt{\lambda}}{2\pi} \frac{\gamma}{u^2} \left(1 + \Pi\omega_0 u^2\right) , \tag{4.58}$$

as follows. For $u \gg u_c$, this energy density approaches the constant

$$-\pi_0^0 \approx \frac{\sqrt{\lambda}}{2\pi} \gamma\Pi\omega_0 . \tag{4.59}$$

Now, consider the total energy along a segment of the string whose extent in u is δu, which we shall denote by $\delta E = -\pi_0^0 \delta u$. The rotating quark can be thought of as "producing this much new string" in a time δt that, from (4.52), is given by $\delta t = \frac{\delta u}{\gamma}$. One should then identify δE with the energy pumped into the system during δt. Equating $\delta E = \frac{dE}{dt}\delta t = P\delta t$ we thus find that

$$P = \frac{1}{\gamma}\pi_0^0 = \frac{\sqrt{\lambda}}{2\pi} \Pi\omega_0 . \tag{4.60}$$

Mikhailov's result (4.2) via a calculation along the lines of Ref. [157] — but with the advantage that we have been able to find analytic expressions for $R(u)$ and $\phi(u)$, which will be a significant help below.

We close this Subsection by commenting on an aspect of the physics of the rotating string that we shall not pursue in detail. As pointed out earlier, there is a special value of u, $u = u_c$ where we should specify the initial condition needed to solve the equations of motion that determine the shape of the rotating string. u_c has a more physical interpretation: it is the depth at which the local velocity of the rotating string, $\omega_0 R(u_c)$, becomes equal to the speed of light in the five-dimensional spacetime. This has a simple interpretation from the point of view of the string worldsheet. It can be verifed that the induced metric on the string worldsheet g_{ab} has an event horizon at $u = u_c$. Thus disturbances on the string become causally disconnected across u_c. (This suggests that in the boundary field theory the regime $r \gg R(u_c) = R_0/v$ can be thought of as the far field region, while $r \lesssim R_0/v$ can be thought of as the near field region.) Even though the AdS$_5$ spacetime with metric G_{MN} has zero temperature, the worldsheet metric is that of a $(1+1)$-dimensional Schwarzschild black hole whose horizon is at $u = u_c$ and whose Hawking temperature is given by

$$T_{\text{ws}} = \frac{1}{2\pi\gamma u_c} = \frac{1}{\gamma} T_{\text{Unruh}} \tag{4.61}$$

where $T_{\text{Unruh}} = \frac{a}{2\pi}$ is the Unruh temperature for an accelerated particle with proper acceleration a. As it radiates, the rotating test quark should experience small kicks which would lead to Brownian motion in coordinate space if the quark had finite mass. At strong coupling such fluctuations can be found from small fluctuations of the worldsheet fields $X^M(t, u)$ in the worldsheet black hole geometry. The thermal nature of the worldsheet metric indicates that such Brownian motion can be described as if due to the presence of a thermal medium with a temperature given by (4.61).

4.3.2 Gravitational perturbation set-up

In the limit $N_c \to \infty$, the $5d$ gravitational constant is parametrically small and consequently the presence of the string acts as a small perturbation on the geometry. To obtain leading order results in $1/N_c$ we write the full metric as

$$G_{MN} = G_{MN}^{(0)} + h_{MN}, \qquad (4.62)$$

where $G_{MN}^{(0)}$ is the unperturbed metric (4.33), and linearize the resulting Einstein equations in the perturbation h_{MN}. This results in the linearized equation of motion

$$- D^2 h_{MN} + 2D^P D_{(M} h_{N)P} - D_M D_N h + \frac{8}{R_{AdS}^2} h_{MN}$$
$$+ \left(D^2 h - D^P D^Q h_{PQ} - \frac{4}{R_{AdS}^2} h \right) G_{MN}^{(0)} = 2\kappa_5^2 t_{MN}, \qquad (4.63)$$

where $h \equiv h^M_M$, D_M is the covariant derivative under the background metric (4.33), κ_5^2 is the $5d$ gravitational constant and t_{MN} is the $5d$ stress tensor of the string. In $\mathcal{N} = 4$ SYM theory, $\kappa_5^2 = 4\pi^2 R_{AdS}^3/N_c^2$, but this relation would be different in other strongly coupled conformal field theories with dual gravitational descriptions. We shall see that κ_5^2 does not appear in any of our results.

According to the gauge/gravity dictionary, the on-shell gravitational action

$$S_G = \frac{1}{2\kappa_5^2} \int d^5x \sqrt{-G} \left(\mathcal{R} + \frac{12}{R_{AdS}^2} \right) + S_{GH} \qquad (4.64)$$

is the generating functional for the boundary stress tensor [156, 155]. Here, G is the determinant of G_{MN}, $\mathcal{R}$ is its Ricci scalar, and S_{GH} is the Gibbons-Hawking boundary term [163], discussed and evaluated in the present context in Ref. [161]. The $5d$ metric G_{MN} induces a $4d$ metric $g_{\mu\nu}$ on the boundary of the the $5d$ geometry. The boundary metric is related to the bulk metric by

$$g_{\mu\nu}(x) \equiv \lim_{u \to 0} \frac{u^2}{R_{AdS}^2} G_{\mu\nu}(x, u). \qquad (4.65)$$

Because $G_{MN} \propto 1/u^2$, the rescaling by u^2 in (4.65) yields a boundary metric that is

regular at $u = 0$. The boundary stress tensor is then given by [155]

$$T^{\mu\nu}(x) = \frac{2}{\sqrt{-g}} \frac{\delta S_G}{\delta g_{\mu\nu}(x)}, \qquad (4.66)$$

with g denoting the determinant of $g_{\mu\nu}$, which was already introduced in Chapter 1 (expression 1.12). We see that in order to compute the boundary stress tensor, one needs to find the string profile dual to the rotating quark and compute its $5d$ stress tensor t_{MN}. One then solves the linearized Einstein equations (4.63) in the presence of the string source and then extracts the boundary stress tensor from the variation of the on-shell gravitational action, as in (4.66). The κ_5^2 dependence drops out because $S_G \propto 1/\kappa_5^2$ while we see from (4.63) that the perturbation to the metric is proportional to κ_5^2.

We determined the string profile in Section 4.3.1. From this, we may now compute the $5d$ string stress tensor, which is what we need in order to determine the metric perturbation due to the string. In general,

$$t^{MN} = -\frac{T_0}{\sqrt{-G}} \sqrt{-g} g^{ab} \partial_a X^M \partial_b X^N \delta^3(\boldsymbol{r} - \boldsymbol{r}_s). \qquad (4.67)$$

For the rotating string given by (4.38) and (4.39) with (4.49) and (4.51), this reduces

to

$$t_{MN} = \frac{\sqrt{\lambda}}{2\pi u R_{AdS}\sqrt{-g}}\delta^3(\boldsymbol{r} - \boldsymbol{r}_s) \tag{4.68}$$

$$\times \begin{pmatrix} R'^2 + R^2s^2\phi'^2 + 1 & R^2s^2\omega_0 R'\phi' & 0 & -R^2s^2\omega_0(R'^2+1) & R^2s^2\omega_0\phi' \\[2ex] R^2s^2\omega_0 R'\phi' & R'^2(R^2s^2\omega_0^2-1) & 0 & -R^2s^2R'\phi' & R'\,(R^2s^2\omega_0^2-1) \\[2ex] 0 & 0 & 0 & 0 & 0 \\[2ex] -R^2s^2\omega_0(R'^2+1) & -R^2s^2R'\phi' & 0 & R^4s^4(\omega_0^2R'^2+\omega_0^2-\phi'^2) & -R^2s^2\phi' \\[2ex] R^2s^2\omega_0\phi' & R'(R^2s^2\omega_0^2-1) & 0 & -R^2s^2\phi' & R^2s^2\omega_0^2-1 \end{pmatrix} , \tag{4.69}$$

where the components are in spherical coordinates, with the rows and columns ordered $(t, r, \theta, \varphi, u)$, and where $s \equiv \sin\theta$.

4.3.3   Gauge invariants and the boundary energy density

Given the string stress tensor (4.68), one can solve the linearized Einstein equations (4.63). However, doing this in its full glory is more work than is necessary. The metric perturbation h_{MN} contains fifteen degrees of freedom which couple to each other via the linearized Einstein equations. This should be contrasted with the $4d$ boundary stress tensor, which is traceless and conserved and thus contains five independent degrees of freedom. Therefore, not all of the degrees of freedom contained in h_{MN} are physical. The linearized Einstein equations are invariant under infinitesimal coordinate transformations $X^M \to X^M + \xi^M$ where ξ^M is an arbitrary infinitesimal vector field. Under such transformations, the metric perturbation transforms as

$$h_{MN} \to h_{MN} - D_M\xi_N - D_N\xi_M , \tag{4.70}$$

135

where D_M is the covariant derivative under the background metric $G_{MN}^{(0)}$. The physical information contained in h_{MN} must be gauge invariant. This requirement restricts the number of physical degrees of freedom in h_{MN} to five,[5] matching that of the boundary stress tensor.

Just as in electromagnetism where gauge invariant quantities (*e.g.* electric and magnetic fields) can be constructed from a gauge field, it is possible to construct gauge invariant quantities out of linear combinations of h_{MN} and its derivatives. The utility of doing this lies in the fact that the equations of motion for gauge invariants don't carry any of the superfluous gauge variant information contained in the full linearized Einstein equations and thus can be simpler to work with. Indeed, as demonstrated in Refs. [164, 161, 159], the equations of motion for gauge invariants can be completely decoupled from each other.

As the background geometry is translationally invariant, it is useful to introduce a $4d$ spacetime Fourier transform and work with mode amplitudes $h_{MN}(u; \omega, \boldsymbol{q})$. Useful gauge invariants can then be constructed out of linear combinations of $h_{MN}(u; \omega, \boldsymbol{q})$ and its radial derivatives and classified according to their behavior under rotations about the $\hat{\boldsymbol{q}}$-axis. As h_{MN} is a spin two field, there exists one independent helicity zero combination and a pair each of independent helicity one and two combinations.[6]

For utility in future work, we shall give an expression for the gauge invariant quantity that is valid at zero or nonzero temperature, even though in this Chapter we shall only use it at $T = 0$. At nonzero T, the warp factor f appearing in the metric (4.33) is given by (4.34). When we later want to recover $T = 0$, we will simply set $f = 1$.

---

[5] Five degrees of freedom in h_{MN} can be eliminated by exploiting the gauge freedom to set $h_{5M} = 0$ for all M, reducing the number of degrees of freedom in h_{MN} to ten. However, just as in electromagnetism, this does not completely fix the gauge. There exists a residual gauge freedom which allows one to eliminate five more components of h_{MN} on any $u = $ const. slice.

[6] There exist many different helicity zero, one and two gauge invariant combinations of h_{MN}, but only five are independent. Different gauge invariants of the same helicity are related to each other by the linearized Einstein equations.

136

We define $H_{MN} \equiv \frac{u^2}{L^2} h_{MN}$ and

$$Z \equiv \frac{4f}{\omega} q^i H'_{0i} - \frac{4f'}{\omega} q^i H_{0i} - \frac{2f'}{q^2} q^i q^j H_{ij} + 4if q^i H_{i5}$$
$$- \frac{(2uq^2 - f')}{q^2} \left(q^2 \delta^{ij} - q^i q^j \right) H_{ij} + \frac{4q^2 f}{i\omega} H_{05} - \frac{8\kappa_5^2 f}{i\omega} t_{05} , \qquad (4.71)$$

where the zeroth and fifth coordinates are t and u respectively and where i and j run over the three spatial coordinates. The quantity Z clearly transforms as a scalar under rotations. With some effort, one can show that Z is invariant under the infinitesimal gauge transformations (4.70). Z is therefore a suitable gauge invariant quantity for our purposes.

The dynamics of Z are governed by the linearized Einstein equations (4.63). Using the linearized Einstein equations, it is straightforward but tedious to show that Z satisfies the equation of motion

$$Z'' + AZ' + BZ = S , \qquad (4.72)$$

where

$$A \equiv -\frac{24 + 4q^2 u^2 + 6f + q^2 u^2 f - 30 f^2}{uf \left(u^2 q^2 + 6 - 6f \right)} , \qquad (4.73)$$

$$B \equiv \frac{\omega^2}{f^2} + \frac{q^2 u^2 (14 - 5f - q^2 u^2) + 18(4 - f - 3f^2)}{u^2 f \left(q^2 u^2 + 6 - 6f \right)} , \qquad (4.74)$$

$$\frac{S}{\kappa_5^2} \equiv \frac{8}{f} t'_{00} + \frac{4 \left(q^2 u^2 + 6 - 6f \right)}{3uq^2 f} (q^2 \delta^{ij} - 3q^i q^j) t_{ij} \qquad (4.75)$$
$$+ \frac{8i\omega}{f} t_{05} + \frac{8u \left[q^2 \left(q^2 u^2 + 6 \right) - f \left(12q^2 - 9f'' \right) \right]}{3f^2 \left(q^2 u^2 - 6f + 6 \right)} t_{00} - \frac{8q^2 u}{3} t_{55} - 8iq^i t_{i5} .$$

The connection between Z and the energy density may be found by considering the behavior of Z and H_{MN} near the boundary. Choosing for convenience the gauge $H_{5M} = 0$, one can solve the linearized Einstein equations (4.63) with a power series expansion about $u = 0$ in order to ascertain the asymptotic behavior of the metric perturbation. Setting the boundary value of $H_{\mu\nu}$ to vanish so the boundary geometry is flat and considering sources t_{MN} corresponding to strings ending at $u = 0$, one

finds an expansion of the form [165, 161]

$$H_{\mu\nu}(u) = H_{\mu\nu}^{(3)}\, u^3 + H_{\mu\nu}^{(4)}\, u^4 + \cdots .$$ (4.76)

In the gauge $H_{5M} = 0$ the variation of the gravitational action (4.66) relates the asymptotic behavior of $H_{\mu\nu}$ to the perturbation in the boundary energy density via [155]

$$\mathcal{E} = \frac{2R_{AdS}^3}{\kappa_5^2} H_{00}^{(4)} .$$ (4.77)

The coefficient $H_{00}^{(4)}$ can in turn be related to the asymptotic behavior of Z by substituting the expansion (4.76) into Eq. (4.71). In doing so one finds that Z has the asymptotic form

$$Z(u) = Z_{(2)}\, u^2 + Z_{(3)}\, u^3 + \cdots ,$$ (4.78)

and that

$$H_{00}^{(4)} = -\frac{1}{16} Z_{(3)} .$$ (4.79)

We therefore see that the energy density is given by

$$\mathcal{E} = -\frac{R_{AdS}^3}{8\kappa_5^2} Z_{(3)} .$$ (4.80)

The coefficient $Z_{(2)}$ in the expansion (4.78), which has delta function support at the location of the quark, gives the divergent stress of the infinitely massive test quark. It is therefore not of interest to us. We now see explicitly that, as we argued above, in order to obtain the energy density in the boundary quantum field theory the only aspect of the metric perturbation that we need to compute is Z, and furthermore that all we need to know are the coefficients in the expansion of Z about $u = 0$.

4.3.4 The solution to the bulk to boundary problem and the boundary energy density

Although we have defined Z at nonzero temperature, henceforth as we determine Z we return to $T = 0$, meaning $f = 1$. At zero temperature the coefficients A and B appearing in (4.72) are given by

$$A = -\frac{5}{u}, \tag{4.81}$$

$$B = \omega^2 - q^2 + \frac{9}{u^2}. \tag{4.82}$$

and the general solution to (4.72) may be written

$$Z(u) = -u^3 I_0(uQ)\left[\int_u^\infty du'\frac{K_0(u'Q)}{u'^2}S(u') + \alpha\right] - u^3 K_0(uQ)\lim_{\epsilon\to 0}\left[\int_\epsilon^u du'\frac{I_0(u'Q)}{u'^2}S(u') + \beta\right],$$
$$\tag{4.83}$$

where $Q \equiv \sqrt{q^2 - \omega^2}$, I_0 and K_0 are modified Bessel functions, and α and β are constants of integration.

The constants of integration are fixed by requiring that $Z(u)$ satisfy appropriate boundary conditions. As $I_0(uQ)$ diverges as $u \to \infty$, regularity at $u = \infty$ requires $\alpha = 0$. The constant β is fixed by the requirement that the $\epsilon \to 0$ limit exists (so all points on the string contribute to the induced gravitational disturbance) and that no logarithms appear in the expansion of $Z(u)$ near $u = 0$. This last condition is equivalent to the boundary condition that the metric perturbation H_{MN} vanish at $u = 0$ so the boundary geometry is flat and unperturbed. For strings which end at $u = 0$, we have

$$S(u) = s_0 + \mathcal{O}(u^2), \tag{4.84}$$

where

$$s_0 = 8\kappa_5^2 \lim_{u\to 0} u^2 \partial_u\left(\frac{t_{00}}{u^2}\right) = -8\kappa_5^2 \lim_{u\to 0}\frac{t_{00}}{u}, \tag{4.85}$$

where we have used the fact that $t_{00} \propto u$ at small u. Furthermore, the Bessel functions

have the asymptotic expansions

$$I_0(uQ) = 1 + \mathcal{O}(u^2) \,, \tag{4.86}$$

$$K_0(uQ) = -\gamma_E - \log(\tfrac{1}{2}uQ) + \mathcal{O}(u^2) \,, \tag{4.87}$$

where γ_E is Euler's constant. Substituting these expansions into the second integral in (4.83), we find

$$\int_\epsilon^\infty du' \frac{I_0(u'Q)}{u'^2} S(u') = \frac{s_0}{\epsilon} + \mathcal{O}(1) \,. \tag{4.88}$$

Therefore, in order for the $\epsilon \to 0$ limit to exist we must have

$$\beta = -\frac{s_0}{\epsilon} \,. \tag{4.89}$$

As one may readily verify, this value of β also eliminates all logarithms appearing in the expansion of Z near the boundary.[7]

With constants of integration determined and with the asymptotic forms (4.84)–(4.87), it is easy to read off from (4.83) the asymptotic behavior of Z. In particular, we find

$$Z_{(3)} = \lim_{\epsilon \to 0} \left[\int_\epsilon^\infty du\, \mathcal{G}(u)S(u) - s_0 \left(\frac{1}{\epsilon} + \epsilon\, \mathcal{G}(\epsilon) \right) \right] \,, \tag{4.90}$$

where

$$\mathcal{G} \equiv -\frac{K_0(u\sqrt{q^2 - \omega_0^2})}{u^2} \,, \tag{4.91}$$

is the *bulk to boundary* propagator.

At this point it is convenient to Fourier transform back to real space. At zero

---

[7] A deformation in the boundary geometry implies that logarithms will occur in the expansion of Z at order u^3 and beyond. The linearized Einstein equations relate all higher order log coefficients to that of the u^3 coefficient in a linear manner. Therefore, if the order u^3 coefficient vanishes all other coefficients vanish. As is easily seen from the asymptotic forms (4.84) – (4.87), the value of β given in (4.89) ensures the order u^3 logarithm coefficient vanishes.

temperature the source (4.75) Fourier transforms to

$$\frac{S(t, \boldsymbol{x}, u)}{\kappa_5^2} = 8u^2 \partial_u \left(\frac{t_{00}}{u^2}\right) - \frac{4u}{3}\nabla^2(2t_{00} - 2t_{55} + t_{ii})$$

$$+ 4u\nabla_i \nabla_j t_{ij} - 8\partial_t t_{05} - 8\nabla_i t_{i5}, \qquad (4.92)$$

where sums over repeated spatial indices i and j are implied. To take the Fourier transform of the bulk to boundary propagator one must give a prescription for integrating around singularities at $\omega = q$. The relevant prescription comes from causality and requires analyticity in the upper half frequency plane. This requires sending $\omega \to \omega + i\epsilon$. With this prescription we have

$$\mathcal{G}(t, \boldsymbol{r}, u) = \frac{1}{\pi u^2}\theta(t)\delta'(-t^2 + r^2 + u^2). \qquad (4.93)$$

We therefore have

$$Z_{(3)}(t, \boldsymbol{r}) = \lim_{\epsilon \to 0} \int d^4r' \left[\int_\epsilon^\infty du\, \mathcal{G}(t-t', \boldsymbol{r}-\boldsymbol{r}', u)S(t', \boldsymbol{r}', u) - \epsilon\, s_0(t', \boldsymbol{r}')\mathcal{G}(t', \boldsymbol{r}-\boldsymbol{r}', \epsilon)\right] - \frac{s_0(t, \boldsymbol{r})}{\epsilon}.$$

$$(4.94)$$

When we use (4.92) to express $S(t', \boldsymbol{r}', u)$ we find that when the du-integral of the first term in (4.92) is done by parts, the resulting boundary term cancels the ϵ-dependent bulk-to-boundary propagator in (4.94).

Upon assuming that the stress-energy tensor on the boundary does not have support at $(t, \boldsymbol{r})$, i.e. that the observer is located away from the source, we can safely take the $\epsilon \to 0$ limit and obtain for the energy density

$$\mathcal{E}(t, \boldsymbol{r}) = \frac{R_{AdS}^3}{\pi}\int d^4r' \int_0^\infty du\, \theta(t-t')\left[(4ut_{00} - t_{M5}\nabla_M'\mathcal{W})\frac{\delta''(\mathcal{W})}{u^2}\right.$$

$$\left. + |\boldsymbol{r} - \boldsymbol{r}'|^2 (4t_{00} - 4t_{55} + 2t_{ii})\frac{\delta'''(\mathcal{W})}{3u} - (t_{ij}\nabla_i'\mathcal{W}\nabla_j'\mathcal{W})\frac{\delta'''(\mathcal{W})}{2u}\right], (4.95)$$

141

where

$$\mathcal{W} \equiv -(t-t')^2 + u^2 + |\boldsymbol{r}-\boldsymbol{r}'|^2 \qquad (4.96)$$

and ∇'_M is the partial derivative with respect to $X'^M = \{t', \boldsymbol{r}', u\}$. We see that the κ_5^2 factors in (4.80) and (4.92) have cancelled, as expected. Because we have analytic expressions for the profile of the rotating string, it turns out that we can evaluate $\mathcal{E}$ explicitly, in two stages. First, using (4.68) including its three-dimensional delta function, and using our expressions (4.49) and (4.51) for $R(u)$ and $\phi(u)$, we obtain

$$\mathcal{E}(t, \boldsymbol{x}) = \frac{\sqrt{\lambda}}{\pi^2} \int_0^\infty du \int_{-\infty}^t dt' \left[\mathcal{A}\, \delta''(\mathcal{W}_s) + \mathcal{B}\, \delta'''(\mathcal{W}_s) \right] , \qquad (4.97)$$

with

$$
\begin{aligned}
\mathcal{A} &= \gamma \left(3 + v^2\gamma^3\omega_0^2 u \left(-t' + t + u\gamma \right) \right) - v\gamma\omega_0 r \sin\theta \cos\psi + v^3\gamma^4\omega_0^2 ur \sin\theta \sin\psi \,, \\
\mathcal{B} &= v^4\gamma^3 u^2 \left(1 - v^2\gamma^4\omega_0^2 u^2 \right) + \left(v^4\gamma^5\omega_0^2 u^2 + \gamma + \frac{1}{3\gamma} \right) |\boldsymbol{r} - \boldsymbol{r}_s(t', u)|^2 \\
&\quad - 2v^3\gamma^3\omega_0 u^2 \left(\cos\psi - v^2\gamma^3\omega_0 u \sin\psi \right) r \sin\theta - v^2\gamma(1 + v^2\gamma^4\omega_0^2 u^2) r^2 \sin^2\psi \, \sin^2\theta \\
&\quad + 2v^2\gamma^2\omega_0 u \, r^2 \cos\psi \, \sin\psi \, \sin^2\theta \,, \qquad (4.98)
\end{aligned}
$$

where $\psi = \varphi + \omega_0(\gamma u - t')$ and

$$\mathcal{W}_s \equiv -(t-t')^2 + u^2 + |\boldsymbol{r} - \boldsymbol{r}_s(t', u)|^2 \,. \qquad (4.99)$$

Next, the integral (4.97) can be carried out via the change of variables

$$\zeta = \frac{1}{2}(\gamma u + t' - t) \,, \quad \nu = \frac{1}{2}(\gamma u - t' + t) \,. \qquad (4.100)$$

Since points with $-(t' - t) < \gamma u$ are causally disconnected from an observer on the boundary at time t, the argument of the δ-functions in Eq. (4.97) is non-vanishing. This allows us to deform the domain of integration and the integral takes the generic

142

form

$$I_n = \int_0^\infty du \int_{-\infty}^{t-\gamma u} dt' F_n(t', u) \delta^{(n)}(\mathcal{W}_s)$$

$$= \frac{2}{\gamma} \int_0^\infty d\nu \int_{-\nu}^0 d\zeta \, \tilde{F}_n(\zeta, \nu) \delta^{(n)}(\mathcal{W}_s), \qquad (4.101)$$

where $\tilde{F}_n(\zeta, \nu) = F_n(t'(\zeta, \nu), u(\zeta, \nu))$. Furthermore, the argument of the δ-functions takes the form

$$\mathcal{W}_s = r^2 + R_0^2 + \zeta \left(4\nu - 2\nu r \sin\theta \sin(2\nu\omega_0 + \varphi - \omega_0 t)\right) - 2r R_0 \sin\theta[\nu\omega_0 \sin(2\nu\omega_0 + \varphi - \omega_0 t)$$

$$+ \cos(2\nu\omega_0 + \varphi - \omega_0 t)], \qquad (4.102)$$

which is then linear in ζ and therefore allows us to evaluate I_n formally, obtaining

$$I_n = \frac{2}{\gamma} \int_{\nu_0}^\infty d\nu \, \frac{(-1)^n \partial_\zeta^n \tilde{F}_n(\zeta, \nu)}{(\partial_\zeta \mathcal{W})^{n+1}} \bigg|_{\zeta = \zeta_0(v)} \qquad (4.103)$$

$$+ \frac{2}{\gamma} \int_0^\infty d\nu \sum_{l=1}^n \frac{(-1)^l}{(\partial_\zeta \mathcal{W})^l} \partial_\zeta^{l-1} \tilde{F}_n(\zeta, \nu) \bigg|_{\zeta = -\nu} \delta^{(n-l)}(\mathcal{W}_s(t' = t - 2\nu, u = 0)).$$

Here $\zeta_0(v)$ is the unique zero of $\mathcal{W}_s$ at a given ν and $\nu_0 = (t - t_{\text{ret}})/2$, but we will not describe in detail how these arise because the integrand in the first term in I_n vanishes: by direct inspection of $F_2 \equiv \mathcal{A}$ and $F_3 \equiv \mathcal{B}$ we find $\partial_\nu^2 \tilde{F}_2(\zeta, \nu) = 0$ and $\partial_\nu^3 \tilde{F}_3(\zeta, \nu) = 0$. Consequently only the boundary terms in the second line of Eq. (4.103) contribute and we can perform the remaining integral using the δ-function. Finally, we obtain

$$\mathcal{E} = \frac{\sqrt{\lambda}}{24\pi^2 \gamma^4 r^6 \Xi^6} \Bigg[-2r^2 \Xi^2 + 4r\gamma^2 \Xi(t_{\text{ret}} - t) + (2\gamma^2 - 4r^2 v^2 \gamma^2 \omega_0^2 \sin^2\theta + 3r^2 \gamma^4 \omega_0^2 \Xi^2)(t_{\text{ret}} - t)^2$$

$$+ 7r\gamma^2 \omega_0^2 \Xi(t_{\text{ret}} - t)^3 + 4\gamma^2 \omega_0^2 (t_{\text{ret}} - t)^4 + 8v\gamma^2 \omega_0 r(t_{\text{ret}} - t)(t_{\text{ret}} - t + r\,\Xi) \times \sin\theta \cos(\varphi - \omega_0 t_{\text{ret}}) \Bigg]$$

$$(4.104)$$

where Ξ was given in (4.16). Recalling the discussion after (4.17), we note that $\mathcal{E}$ is invariant under a shift of φ by $\delta\varphi$ that is compensated by shifts in both t and t_{ret} by

$\delta\varphi/\omega_0$. $\mathcal{E}$ is a periodic function of φ with period 2π and a periodic function of t with period $2\pi/\omega_0$, as it must be.

Eq. (4.104) is the main result of this Chapter. It is an explicit analytic expression for the energy density of the radiation emitted by a test quark in circular motion, valid at all times and at all distances from the quark. The only aspect of the calculation that requires numerical evaluation is that one must solve the transcendental equation (4.17) for t_{ret}. With t_{ret} in hand, one uses (4.16) to compute Ξ and then evaluates the energy density $\mathcal{E}$ using the solution (4.104). We shall illustrate our result (4.104) in several ways in Section 4.4.

4.3.5 Far zone and angular distribution of power

We close this Section by evaluating the energy density (4.104) in the $r \to \infty$ limit and extracting the angular distribution of power à la Eq. (4.26). In the far zone limit we can replace Ξ by its $r \to \infty$ limit, namely $\tilde{\xi}$ in (4.28), and we can safely replace t_{ret} by $(t - r)$ everywhere in (4.104) except within the φ-dependent argument of the cosine. In the far zone, the energy density (4.104) then reduces to that of Eq. (4.25) with

$$\varepsilon = \frac{\omega_0^2\sqrt{\lambda}}{24\pi^2} \frac{4 - 4v^2\sin^2\theta - 7\tilde{\xi} + 3\tilde{\xi}^2\gamma^2}{\tilde{\xi}^6\gamma^2}. \tag{4.105}$$

Using Eq. (4.26), we find that the time-averaged angular distribution of power is given by

$$\frac{dP}{d\Omega} = \frac{v^2\gamma^3\omega_0^2\sqrt{\lambda}}{32\pi^2} \frac{5\gamma^2 - 1 - v^2\gamma^2\cos(2\theta)}{\left(\gamma^2\cos^2\theta + \sin^2\theta\right)^{5/2}}. \tag{4.106}$$

Just as in the case of weak coupling, the radiated power is focused about $\theta = \pi/2$ with a characteristic width $\sim 1/\gamma$. We shall plot (4.106) and compare it to the weak coupling result in Section 4.4.

Upon integrating over all solid angles, we find the total power radiated

$$P = \frac{\sqrt{\lambda}}{2\pi}a^2, \tag{4.107}$$

144
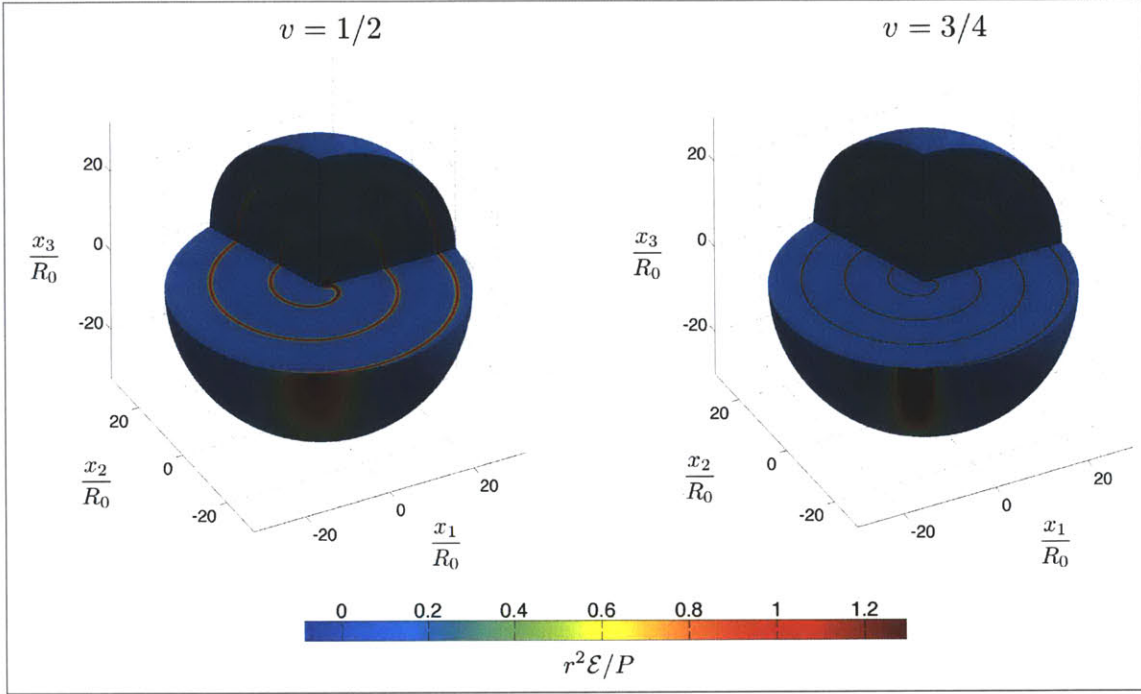
Figure 4-4: Left: a cutaway plot of $r^2\mathcal{E}/P$ for $v = 1/2$. Right: a cutaway plot of $r^2\mathcal{E}/P$ for $v = 3/4$. In both plots the quark is at $x_1 = R_0$, $x_2 = 0$ at the time shown and its trajectory lies in the plane $x_3 = 0$. The cutaways coincide with the planes $x_3 = 0$, $\varphi = 0$ and $\varphi = 7\pi/5$. At both velocities the energy radiated by the quark is concentrated along a spiral structure which propagates radially outwards at the speed of light. The spiral is localized about $\theta = \pi/2$ with a characteristic width $\delta\theta \sim 1/\gamma$. As $v \to 1$ the radial thickness Δ of the spirals rapidly decreases like $\Delta \sim 1/\gamma^3$.

where again $a = v\gamma^2\omega_0$ is the quark's proper acceleration, reproducing Mikhailov's result (4.2) again. The fact that the power that we have obtained in this Section by integrating over the angular distribution of the radiation (4.106) in the quantum field theory matches the energy flux (4.57) flowing down the classical string in the dual gravitational description is a nontrivial check of our calculations.

4.4 Results and Discussion

4.4.1 Radiation at strong coupling, illustrated

Fig. 4-4 shows two cutaway plots of the energy density $\mathcal{E}$ at strong coupling (multiplied by r^2/P where P is the total power radiated) produced by a quark moving on a circle

145
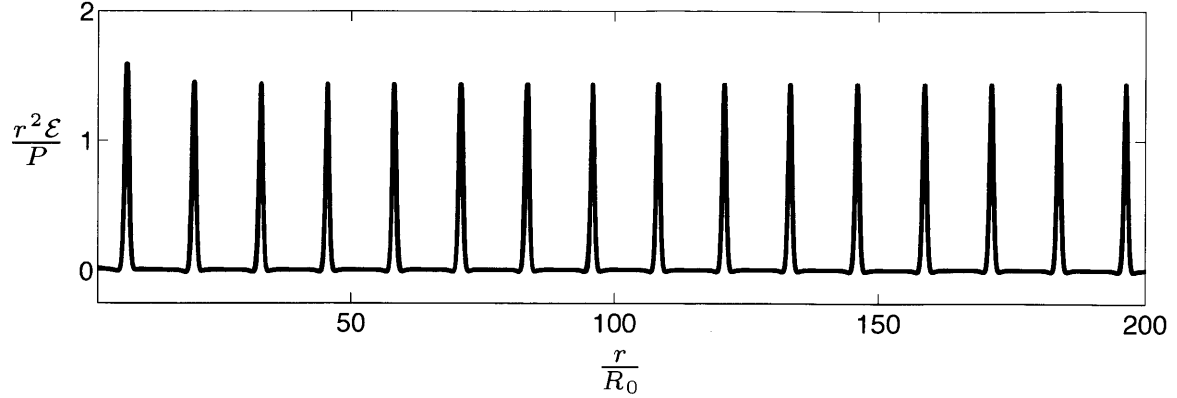
Figure 4-5: Plot of $r^2\mathcal{E}/P$ at $\theta = \pi/2$ and $\varphi = 5\pi/4$ at $t = 0$ as a function of r for $v = 1/2$. The plot illustrates the fact that the pulses of radiated energy do not broaden as they propagate outward. This implies that they do not broaden in azimuthal angle, either. Strongly coupled synchrotron radiation does not isotropize.

of radius R_0 at velocities $v = 1/2$ and $v = 3/4$. The Figure is obtained by evaluating (4.104). The motion of the quark is confined to the plane $x_3 = 0$ and at the time shown the quark is at $x_1 = R_0$, $x_2 = 0$, and is rotating counter clockwise. The cutaways in the plots show the energy density on the planes $x_3 = 0$, $\varphi = 0$ and $\varphi = 7\pi/5$ where φ is the azimuthal angle. As is evident from the Figure, as the quark accelerates along its trajectory energy is radiated outwards in a spiral pattern. This radiation falls off like $1/r^2$ and hence has a constant amplitude in the Figure and propagates radially outwards at the speed of light. The Figure shows the location of the energy density at one time; as a function of time, the entire pattern of energy density rotates with constant angular frequency $\omega_0 = R_0 v$. This rotation of the pattern is equivalent to propagation of the radiation outwards at the speed of light. As seen by an observer far away from the quark, the radiation appears as a short pulse just like a rotating lighthouse beam does to a ship at sea.

What we see in Fig. 4-4 looks like an outward going pulse of radiation that does not broaden as it propagates. Analysis of (4.104) confirms this, as we have illustrated in Fig. 4-5 by extending the plot of the energy density outward to much larger radii at one value of the angular coordinates, at time $t = 0$. As time progresses, the pulses move outward at the speed of light, and an observer at large r sees repeating flashes of radiation. This Figure provides a convincing answer to a central question that we set

146

out to answer in Section 4.1. We see that even though the gauge theory is nonabelian and strongly coupled, the narrow pulses of radiation propagate outward without any hint of broadening. We find the same result at much larger values of γ, where the pulses become even narrower — their widths are proportional to $1/\gamma^3$, as at weak coupling and as we shall discuss below. The behavior that we find is familiar from classical electrodynamics — in which the radiated energy is carried by noninteracting photons. Here, though, the energy is carried by fields that are strongly coupled to each other. And, yet, there is no sign of this strong coupling in the propagation of the radiation. No broadening. No isotropization.

Fig. 4-5 is also of some interest from a holographic point of view. The qualitative idea behind gauge/gravity duality is that depth in the 5th dimension in the dual gravitational description corresponds to length-scale in the quantum field theory. In many contexts, if one compares two classical strings in the gravitational description which lie at different depths in the 5th dimension, the string which is closer to the boundary corresponds to a thinner tube of energy density in the quantum field theory while the string which is deeper, farther from the boundary, corresponds to a fatter tube of energy density. Our calculation shows that this intuitive way of thinking about gauge/gravity duality need not apply. The rotating string falls deeper and deeper into the 5th dimension with each turn of its coils and yet the thickness of the spiral tube of energy density in the quantum field theory that this string describes changes not at all. Reference [94] gives a nice geometric description of our results using gravitational shock waves which shines some light on this apparent contradiction with the IR/UV duality.

The behavior of the outgoing pulse of radiation illustrated in Fig. 4-5 is different than what one may have expected for a nonabelian gauge theory given that solutions to the *classical* field equations in $SU(2)$ and $SU(3)$ gauge theory are chaotic with positive Lyapunov exponents and are thought to be ergodic [166, 167, 168]. Of course, we have not solved classical field equations; we have done a fully quantum mechanical analysis of the radiation in a nonabelian gauge theory, in the limit of large N_c and strong coupling. It is nevertheless surprising from the gauge theory perspective that
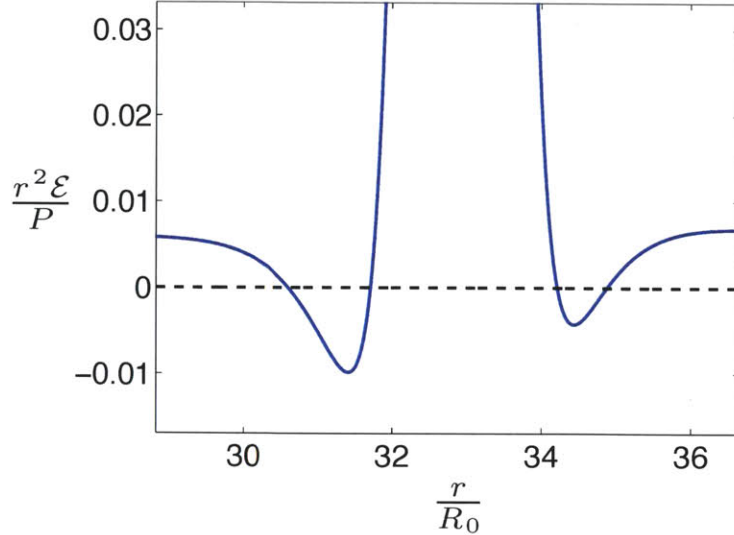
Figure 4-6: The energy density at $\theta = \pi/2$ and $\varphi = 5\pi/4$ for quark velocity $v = 1/2$, as in Fig. 4-5. $r \approx 33 R_0$ corresponds to the location of a spiral in the energy density. Directly ahead of and directly behind the spiral, the energy density is slightly negative. To see how slightly, compare the vertical scale here with that in Fig. 4-5.

the radiation we find turns out to behave (almost) like that in classical electrodynamics. From the gravitational perspective, we saw that the equations describing the five-dimensional metric perturbations linearize, meaning that there is no possibility of chaotic or ergodic dynamics.

The synchrotron radiation that we have found at strong coupling is, in at least one respect, qualitatively different from that in familiar classical electrodynamics. The difference is in principle visible in Fig. 4-5, but the effect is small and hard to see without zooming in — which we do in Fig. 4-6. For large enough v we find that the energy density is *negative* in some regions of space! Directly ahead of and behind the spiral, the energy density dips slightly below zero. This is impossible in classical electrodynamics. The effect that we have found is numerically small, as a comparison of the vertical scales in Figs. 4-6 and 4-5 makes clear, but it is nevertheless in stark contrast to the weak coupling results of Section 4.2, where the energy density is always positive, as in classical electrodynamics. This small effect serves as a reminder that the calculation that we have done is quantum mechanical. In a quantum field theory the energy density need not be positive everywhere — only its integral over all space

is constrained to be positive. In a strongly coupled quantum field theory, quantum effects should be large. So, it is not surprising that we see a quantum mechanical effect. What is surprising is that it is so small, and that in other respects Figs. 4-4 and 4-5 look so similar to synchrotron radiation in classical electrodynamics.

4.4.2 Synchrotron radiation at strong and weak coupling

Given the qualitative similarities between Figs. 4-4 and 4-5 and the physics of synchrotron radiation in classical electrodynamics and weakly coupled $\mathcal{N} = 4$ SYM theory, we shall attempt several more quantitative comparisons. First, as can be seen from Fig. 4-4, the radiation emitted by the quark is localized in polar angle about the equator, $\theta = \pi/2$. From the far-zone expression for the energy density, Eqs. (4.25) and (4.105), it is easy to see that the characteristic opening angle about $\theta = \pi/2$ scales like $\delta\theta \sim 1/\gamma$ in the $v \to 1$ limit. Furthermore, from Fig. 4-4 it can be seen that the radial thickness Δ of each pulse of radiation decreases as v increases. Again, from Eqs. (4.25) and (4.105) it is easy to see that $\Delta \sim 1/\gamma^3$ in the $v \to 1$ limit.[8] Intriguingly, the scaling of both $\delta\theta$ and Δ with γ are identical to those at weak coupling.

Emboldened by the agreement between the γ-scaling of Δ and $\delta\theta$ at weak and strong coupling, we have compared the shape of the spiral of energy density in the $x_3 = 0$ plane, for example as depicted at two velocities in Fig. 4-4, with the shape of the classic synchrotron radiation spiral (4.19). We find precise agreement, as illustrated in Fig. 4-7. At strong coupling, the energy density $\mathcal{E}$ of (4.104) is proportional to $1/\Xi^6$ and so has maxima where Ξ has minima. We have already seen that in the $r \to \infty$ limit, $\Xi \to \tilde{\xi}$ of (4.28) whose minima lie on the spiral (4.20), which is the

---

[8] There may be a holographic interpretation of $\Delta \sim 1/\gamma^3$. We saw in Section 4.3.1 that there is one special point on the string, namely the worldsheet horizon at $u = u_c$. Using the correspondence between u and length-scale in the boundary quantum field theory, we expect u_c to translate into a length scale in the rest frame of the rotating quark, corresponding to a length scale

$$\delta \sim \frac{u_c}{\gamma} = \frac{1}{\gamma^3 v \omega_0} = \frac{R_0}{\gamma^3 v^2} \; , \tag{4.108}$$

in the inertial frame in which the center of motion is at rest. It is tempting to identify δ with Δ at $v \to 1$.
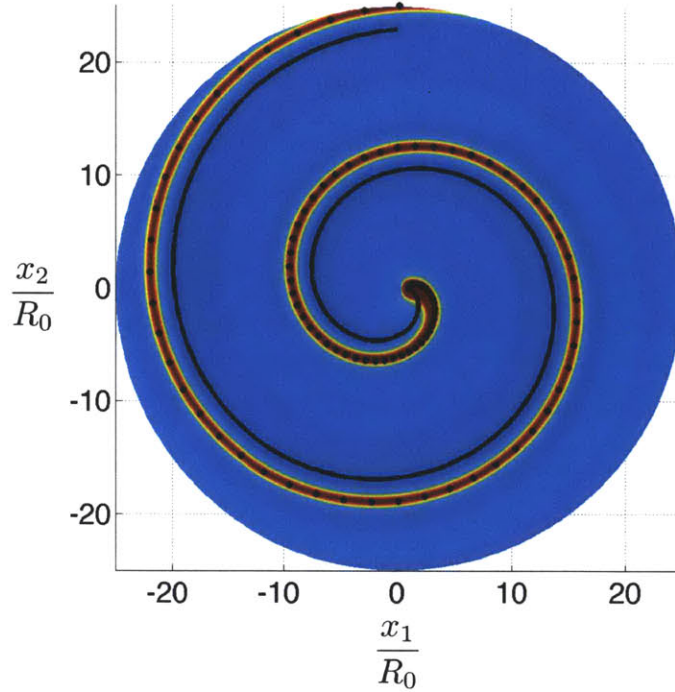
Figure 4-7: $r^2\mathcal{E}/P$ for $v = 1/2$ in the $x_3 = 0$ plane. The color code is the same as in Fig. 4-4, with zero energy density blue and maximal energy density red. The spiral curve marked with the black dots is (4.19), namely the place where the spiral of synchrotron radiation would be in electrodynamics or in weakly coupled $\mathcal{N} = 4$ SYM theory. We see that the spiral of radiation in the strongly coupled gauged theory with a gravitational dual is at the same location. This indicates that, as at weak coupling, strongly coupled synchrotron radiation is beamed in the direction of the motion of the quark. For reference, the solid black line is (4.21), namely the place where the synchrotron radiation would be if the quark were emitting a beam of radiation perpendicular to its direction of motion.

large-r approximation to (4.19). It can also be shown that the minima of Ξ lie on the spiral (4.19) at all r.

Recall that our derivation of (4.19) in Section 4.2 was purely geometrical, relying only on the fact that the radiation is emitted tangentially, in the direction of the velocity vector of the quark and the fact that the pulse of radiated energy density propagates at the speed of light without spreading. We have seen in Fig. 4-5 that at strong coupling and in the limit of a large number of colors, the radiation emitted by a rotating quark does indeed propagate outwards at the speed of light, without spreading. This justifies the application of the geometrical arguments of Section 4.2 to the strongly coupled radiation. The agreement with (4.18) and (4.19) then

implies that the strongly coupled radiation is also emitted in the direction of the velocity vector of the quark: if it were emitted in any other direction, Δ would have the same γ-scaling as α and $\delta\theta$; if the radiation were, for example, emitted perpendicular to the direction of motion of the quark, the spiral of energy density would have the shape (4.21) instead of (4.19) — see Fig. 4-7. We therefore reach the following conclusions: at both weak and strong coupling, the energy radiated by the rotating quark is beamed in a cone in the direction of the velocity of the quark with a characteristic opening angle $\alpha \sim 1/\gamma$; at both weak and strong coupling, the synchrotron radiation propagates outward in a spiral with the shape (4.19), with pulses whose width $\Delta \sim 1/\gamma^3$ does not broaden.[9]

4.4.3 Angular distribution of power at strong and weak coupling

We now turn to the time-averaged angular distribution of power radiated through the sphere at infinity. By time-averaging, we eliminate all dependence on azimuthal angle but nontrivial dependence on the polar angle θ remains. For the case of weakly coupled $\mathcal{N} = 4$ SYM, in Section 4.2 we calculated the angular distribution of the radiated power, finding

$$\left.\frac{dP}{d\Omega}\right|_{\lambda \ll 1} = \frac{dP_{\text{vector}}}{d\Omega} + \frac{dP_{\text{scalar}}}{d\Omega} \, , \qquad (4.109)$$

with $dP_{\text{vector}}/d\Omega$ and $dP_{\text{scalar}}/d\Omega$ given in (4.30a) and (4.30b). For the case of strongly coupled radiation, in any conformal quantum field theory with a classical dual gravity description, our result for the time-averaged angular distribution of power is given in (4.106). Since we know that the total power radiated at weak and strong coupling are equivalent up to a substitution of their prefactors (4.32), it is natural to ask whether the angular distribution (4.106) can be related to (4.109). The answer is yes, but

---

[9]Note that if the radiation is isotropic in the instantaneous rest frame of the quark, then in the inertial "lab" frame it will be beamed in a cone with opening angle $\sim 1/\gamma$ pointed along the velocity of the quark. This, together with the result that the pulses of radiation propagate without broadening, would yield a spiral with the shape (4.19).
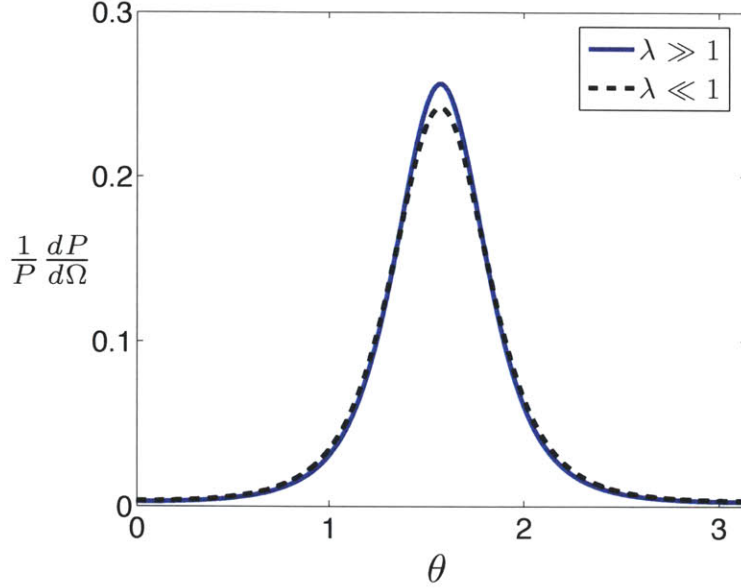
Figure 4-8: The normalized time-averaged angular distribution of power at both weak and strong coupling at $v = 0.9$. At both weak and strong coupling, the time averaged angular distribution of power is localized about $\theta = \pi/2$ with a characteristic width $\delta\theta \sim 1/\gamma$. The (slight) difference in the shapes of the two angular distributions is as if the ratio of power radiated in vectors and scalars is $2 : 1$ in the strongly coupled radiation, while it is $4 : 1$ in the weakly coupled case.

with a twist: we find that our strong coupling result (4.106) can be written as

$$\frac{dP}{d\Omega}\bigg|_{\lambda \gg 1} = \frac{\sqrt{\lambda}}{5e_{\text{eff}}^2/12} \left[\frac{5}{6} \frac{dP_{\text{vector}}}{d\Omega} + \frac{5}{3} \frac{dP_{\text{scalar}}}{d\Omega} \right], \tag{4.110}$$

where the relation between e_{eff}^2 and λ is given by (4.11) in $\mathcal{N} = 4$ SYM theory. We see that the time averaged angular distribution of power at weak and strong coupling are related by the following prescription: start with the weakly coupled result (4.109); suppress the vector contribution by a factor of $5/6$ and enhance the scalar contribution by a factor of $5/3$, noting from (4.31a) and (4.31b) that this does not change the total power but means that the scalar/vector ratio in the total power has been increased from $1/4$ to $1/2$; then make the change of prefactors (4.32); that gives you the strongly coupled result (4.106).

The solid blue curve in Fig. 4-8 shows the time-averaged angular distribution of power at strong coupling (4.106) for $v = 0.9$, normalized by the total power radiated

152

at strong coupling, $P_{\lambda \gg 1}$ given in (4.107). The dashed black curve in the Figure is the normalized time-averaged angular distribution of power at weak coupling (4.109), normalized by the total power radiated at weak coupling, which is $P_{\lambda \ll 1} = P_{\text{vector}} + P_{\text{scalar}}$, with (4.31a) and (4.31b). Because the two curves are normalized by their respective total powers which are related by $P_{\lambda \gg 1}/P_{\lambda \ll 1} = \sqrt{\lambda}/(5e_{\text{eff}}^2/12)$, the comparison of the two curves is the comparison of the right-hand side of (4.109) with the quantity in square brackets on the right-hand side of (4.110). It is evident from the Figure that the radiation pattern at strong coupling is qualitatively similar to that at weak coupling. In both regimes, the angular distribution of power is focused about $\theta = \pi/2$ with a characteristic width $\delta\theta \sim 1/\gamma$. The small difference between the angular distributions is as if the ratio of the power radiated in vectors and scalars is $2 : 1$ in the strongly coupled radiation, whereas it is $4 : 1$ in the weakly coupled case. Of course, we cannot actually separate the strongly coupled vectors from the strongly coupled scalars.

4.4.4 Relation with previous work

Next, we return to the discussion of the relation between our present work and previous works that we began in Section 4.1. In Ref. [56], states produced by the decay of off-shell bosons in strongly coupled conformal field theories were studied. It was shown in Ref. [56] that the event-averaged angular distribution of power radiated from the decay is isotropic (in the rest frame of the boson where the total momentum vanishes) and independent of the boson's spin. This should be contrasted with similar weak coupling calculations in QCD, where the boson's spin imprints an "antenna" pattern on the distribution of radiation at infinity [150, 151, 152]. Our results are not inconsistent with those of Ref. [56]. First of all, we and the authors of Ref. [56] are considering very different initial states. Second, as discussed in Ref. [56], if their initial off-shell boson has a non-trivial distribution of momentum, this distribution imprints itself on the angular distribution of radiation at infinity and generically results in an anisotropic distribution of power. It is only the spin of the boson which doesn't produce any anisotropy.

In Ref. [58] it was argued that isotropization must occur in the strongly coupled limit due to parton branching. Heuristically, the authors of Ref. [58] argued that at strong coupling parton branching is not suppressed and that successive branchings can scramble any initially preferred direction in the radiation as it propagates out to spatial infinity. However, our results clearly demonstrate that this need not be the case. We see no evidence for isotropization of the radiation emitted by the rotating quark. In fact, the time-averaged angular distribution of power, shown in Fig. 4-8, is slightly more peaked about $\theta = \pi/2$ in the strongly coupled limit. And, just as for weakly coupled radiation, the strongly coupled radiation that we have illustrated in Figs. 4-4 and 4-5 propagates outward in pulses that do not broaden: their extent in azimuthal angle at a given radius remains the same out to arbitrarily large radii and, correspondingly, their radial width is also unchanging as they propagate. It is not clear in any precise sense what parton branching would mean in our calculation if it occurred, since no partons are apparent. But, the essence of the effect is the transfer of power from shorter wavelength modes to longer wavelength modes. In our calculation, that would correspond to the pulses in Fig. 4-5 broadening as they propagate. This we do not see.

4.4.5 A look ahead to nonzero temperature

It is exciting to contemplate shining a tightly collimated beam of strongly coupled synchrotron radiation into a strongly coupled plasma. Although this will have its failings as a model of jet quenching in the strongly coupled quark-gluon plasma of QCD, so too do all extant strongly coupled approaches to this complex dynamical problem. The calculation that is required is simple to state: we must repeat the analysis of the radiation emitted by a rotating quark, but this time in the AdS black hole metric that describes the strongly coupled plasma that arises at any nonzero temperature in any conformal quantum field theory with a dual gravitational description. The calculation will be more involved, and likely more numerical, both because the temperature introduces a scale into the metric and because to date we have only a numerical description of the profile of the rotating string [157]. If we choose $T \ll 1/R_0$

154

and $\gamma \gg 1$ then the criterion (4.7) will be satisfied and the total power radiated will be as if the quark were rotating in vacuum [157]. Based upon our results, we expect to see several turns of the synchrotron radiation spiral before the radiation has spread to radii of order $1/T$ where it must begin to thermalize, converting into hydrodynamic excitations moving at the speed of sound, broaden, and dissipate due to the presence of the plasma. We will be able to investigate how the length scale or scales associated with these processes vary with R_0 and γ. Note that the typical transverse wavelengths of the quanta of radiation in the pulse will be of order R_0/γ while their typical longitudinal wavelengths and inverse frequencies will be of order R_0/γ^3, meaning that we will have independent control of the transverse momentum and the frequency of the gluons in the beam of radiation whose quenching we will be observing.

Since at nonzero temperature the coils of the rotating string only extend outwards to some γ-dependent $r_{\max}$, it is natural to expect that this $r_{\max}$ will correlate with at least one of the length-scales describing how the spiral of synchrotron radiation shines through the strongly coupled plasma. Our guess is that $r_{\max}$ will prove to be related to the length scale at which the energy carried by the nonhydrodynamic spiral of synchrotron radiation as in vacuum converts into hydrodynamic waves. If so, we can estimate the parametric dependence of $r_{\max}$ at large γ, as follows. For $r \gg r_{\max}$, the power $P \propto \sqrt{\lambda} a^2 \propto \sqrt{\lambda} \gamma^4 / R_0^2$ radiated by the rotating quark will be carried by long wavelength hydrodynamic modes whose energy density will fall off $\propto \sqrt{\lambda} \gamma^4 / r^2$. For $r \ll 1/T$, we will have a spiral of synchrotron radiation whose energy density is ε/r^2 with ε given by (4.105). Recalling from Section 4.2 that on the spiral $\tilde{\xi} = 1 - v \propto 1/\gamma^2$, we see from (4.105) that, on the spiral, the energy density is $\propto \sqrt{\lambda} \gamma^8 / r^2$. We expect that for $1/T \ll r \ll r_{\max}$ this energy density will be attenuated by a factor $\propto \exp(-\text{const}\, r\, T)$. The parametric dependence of the $r_{\max}$ at which the hydrodynamic modes take over from the nonhydrodynamic spiral can then be determined by comparing the parametric dependence of the two energy densities:

$$\frac{\sqrt{\lambda}\gamma^4}{r_{\max}^2} \sim \frac{\sqrt{\lambda}\gamma^8}{r_{\max}^2} \exp\left(-\text{const}\, r_{\max}\, T\right) , \qquad (4.111)$$

meaning that

$$r_{\mathrm{max}} \propto \frac{\log \gamma}{T} \; .$$

(4.112)

Interestingly, the numerical results of Ref. [157] do indicate that r_{max} diverges slowly as $\gamma \to \infty$.

Chapter 5

Summary

Quantum Chromodynamics (QCD) is a very successful theory in describing the interactions between quarks and gluons. But, as it becomes strongly coupled at low energies, its phase diagram and many properties of QCD matter are still not well understood. Examples of such not well-known QCD properties include the location of the QCD critical point - the endpoint of the first-order phase transition line between hadron matter and the Quark-Gluon Plasma (QGP) - and properties of the strongly coupled QGP, which is formed at the early stages of heavy-ion collision experiements. In this thesis, we studied some of these properties and we summarize our work below.

In Chapter 2, we studied selected fluctuation observables in order to locate the QCD critical point in heavy-ion collision experiments. The characteristic signature is the non-monotonic behavior as a function of the collision energy of higher, non-Gaussian, moments of the event-by-event distributions of pion, proton and net proton multiplicities and of various measures of pion-proton correlations. We presented quantitative estimates of the contribution of critical fluctuations to all these observables as a function of the same five non-universal parameters, one of which is the correlation length that parametrizes proximity to the critical point. We constructed ratios of observables that will allow an overconstrained experimental determination of currently poorly known parameters of the theory. And, we constructed other ratios of observables that, if the measured cumulants are indeed dominated by critical fluctuations, are independent of all the parameters in our calculation and are independent of the

value of the correlation length. We are therefore able to make parameter-independent predictions for these ratios, predictions that we hope will some day make it possible to determine with confidence that observed fluctuations do indeed indicate proximity to the critical point. At the time of writing this thesis, experimental data on pion and proton cumulant ratios are being analyzed by the STAR collaboration which could give us some indication on the location of critical point.

As we discussed in Chapter 1, the QGP created at the early stages of heavy-ion collisions is strongly coupled and hence we cannot use perturbative methods to analyze its properties. In this thesis, we used the gauge/gravity duality (or AdS/CFT correspondence) as a tool to study two properties of strongly coupled plasmas - the velocity dependence of the baryon screening length and the synchrotron radiation. The duality applies to strongly coupled gauge theories that have gravity duals and in this thesis, we applied the duality to $\mathcal{N} = 4$ Supersymmetric Yang-Mills (SYM) gauge theory.

In Chapter 3, we found that the screening length of a baryon configuration consisting of N_c quarks in a circle (or a slightly squashed circle), moving with velocity v through the plasma of $\mathcal{N} = 4$ SYM theory in a direction perpendicular (or parallel) to the plane of the configuration is given by

$$L_s = \frac{a(1 - v^2)^{1/4}}{T} , \tag{5.1}$$

where a depends only weakly on v and, in the case of the baryon moving parallel to the plane defined by the quarks, the angle between the strings and the velocity. This velocity dependence is precisely the same as that for the screening length defined by a quark and antiquark moving through the plasma, and even the weak angular dependence of a is strikingly similar. This is a confirmation of the robustness of the velocity dependence of screening that in the meson sector has as a consequence the experimentally testable prediction that in a range of temperatures, that is plausibly accessed in heavy-ion collisions at RHIC (or at the LHC), J/Ψ (or Υ), suppression may set in only for quarkonia moving with a transverse momentum above some threshold [42].

In the baryon sector, it indicates that if baryons composed of three charm quarks are ever studied in heavy-ion collision experiments, which do not reach such high temperatures as to dissociate them at rest, their production would also be suppressed above some threshold transverse momentum.

In Chapter 4, we used the gauge/gravity duality to study another property of strongly coupled plasmas - the synchrotron radiation. We computed the energy density and angular distribution of the power radiated by a quark undergoing circular motion in the vacuum of strongly coupled $\mathcal{N} = 4$ SYM theory. Our strong coupling results are in fact valid for any strongly coupled conformal field theory with a dual classical gravity description. We compared the strong coupling results to those at weak coupling, finding them to be very similar. In both regimes, the angular distribution of the radiated power is in fact similar to that of synchrotron radiation produced by an electron in circular motion in classical electrodynamics: the quark emits radiation in a narrow beam along its velocity vector with a characteristic opening angle $\alpha \sim 1/\gamma$ - something that looks like a "jet". This jet-like beam of gluons opens a new way of modeling jet quenching in heavy-ion collisions. By turning on a finite temperature, we can study the broadening of this beam of radiation and the length scales at which it converts into hydrodynamic excitations.

The gauge/gravity duality has given us many insights relevant for heavy-ion phenomenology in recent years. Heavy-ion experiments at the LHC and RHIC are underway and will provide us with additional experimental information on the properties of hot QCD matter at strong coupling. Therefore, a better understanding of these properties will be a key theoretical focus in the coming years and we expect that the gauge/gravity duality will continue to be a powerful tool in helping us understand these topics.

Appendix A

Toy Model Probability Distribution for Critical Point Fluctuations

In Section 2.2.2 we presented the calculation of (and results for) the second, third and fourth cumulants of the pion, proton and net proton multiplicity distributions near the QCD critical point. We found, for example, that with our benchmark parameters ω_{4p} peaked at a value of around 400, while for a Poisson distribution $\omega_{4p} = 1$. This dramatic increase in ω_{4p} due to critical fluctuations with a reasonable value of $\xi = \xi_{\max} = 2$ fm raises the question of what the distribution whose moments we calculated looks like — does it in any way look unreasonable or unphysical? Although the results from Section 2.2.2 of Chapter 2 determine arbitrarily high cumulants of the proton multiplicity distribution, they do not allow us to determine the shape of the distribution itself. In this Appendix, we provide an example of a probability distribution $\mathcal{P}(N_p)$ which has values of ω_{ip} for $i = 2, 3$ and 4 that are comparable to those we calculated in Section 2.2.2. This toy model distribution is somewhat, but not completely, *ad hoc*, since we shall construct it in a way that does reflect the origin of the critical contribution to the fluctuations.

Let us consider a free gas of particles of a given species that have a mass $M(\sigma)$ which is a function of a background field σ. As an example, for protons we shall

use $M(\sigma) = m_p + g_p\sigma$. And, let us assume that the σ field fluctuates with a given probability distribution $\mathcal{P}_\sigma(\sigma)$. The central simplification that we are making in constructing this toy model is that we are assuming that σ is spatially homogeneous. The field σ fluctuates, but at any given time it is the same everywhere in space. Let us model the probability distribution for the number N_p of particles with mass $M(\sigma)$ by considering the fluctuations of N_p due to the fluctuations in σ. Integrating over the fluctuating σ we obtain the probability distribution for N_p:

$$\mathcal{P}(N_p) = \int d\sigma\, \mathcal{P}_\sigma(\sigma)\, P_{M(\sigma)}(N_p) \tag{A.1}$$

where $P_M(N)$ is the probability distribution for a particle with *fixed* mass M which we choose to be Poisson:

$$P_M(N_p) = \frac{\bar{N}^{N_p}}{N_p!} e^{-\bar{N}}, \tag{A.2}$$

where $\bar{N}$ is the expectation (mean) value of N_p for the distribution $P_M(N_p)$. In thermal and chemical equilibrium,

$$\bar{N} = V \int_k \frac{1}{\exp\left(\frac{\sqrt{k^2 + M(\sigma)^2} - \mu}{T}\right) \pm 1} \tag{A.3}$$

where we choose the positive sign since protons are fermions. $\bar{N}$ depends on M and, therefore, on σ.

The probability distribution of σ is determined by the effective potential $\Omega(\sigma)$:

$$\mathcal{P}_\sigma(\sigma) \sim \exp\left(-V\frac{\Omega(\sigma)}{T}\right), \tag{A.4}$$

where the effective potential can be written as

$$\Omega(\sigma) = \frac{m^2}{2}\sigma^2 + \frac{\lambda_3}{3}\sigma^3 + \frac{\lambda_4}{4}\sigma^4 + \dots, \tag{A.5}$$

namely (2.21) without the spatial gradients. Eqs. (A.1)-(A.5) define the probability distribution for the particle number, which will depend, among other things, on the
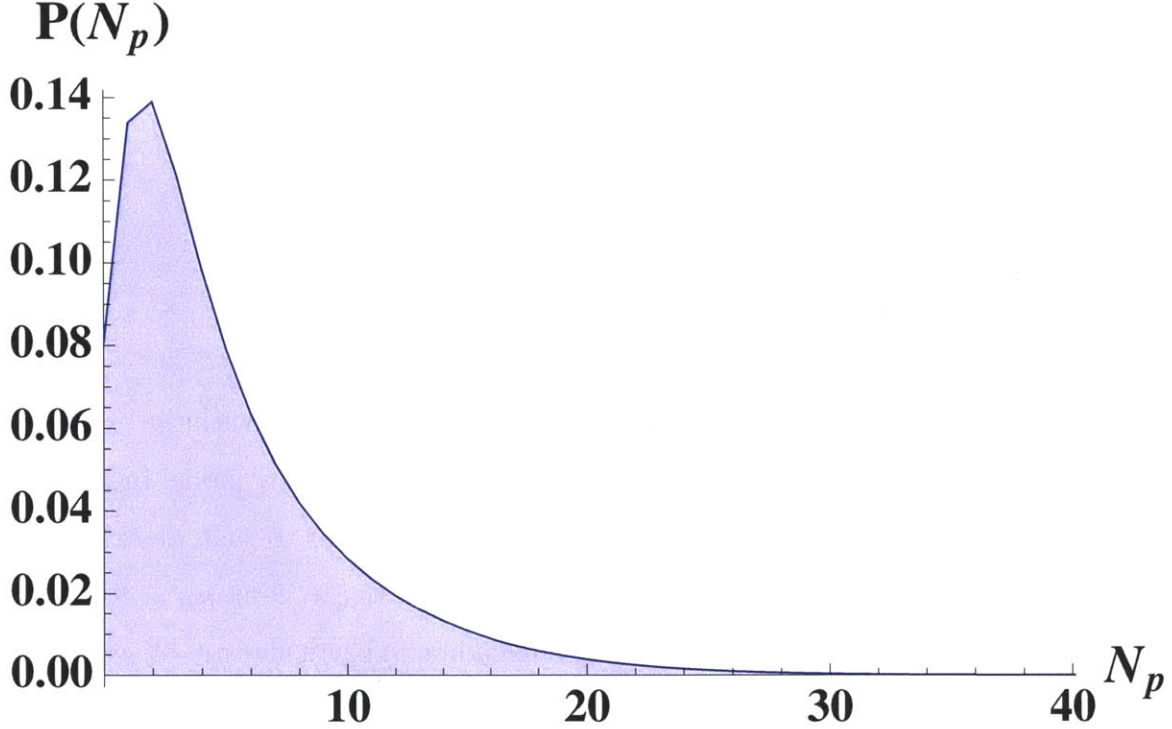
Figure A-1: An example of a distribution with $\omega_{4p}^{\text{model}} \approx 400$. The construction of the model distribution is described in the text, as are the values of its first few cumulants. N_p is the number of protons in a volume $V = (5\,\text{fm})^3$ in the toy model distribution. Other parameter choices are described in the text.

correlation length $\xi \equiv m_\sigma^{-1}$. Note that since the volume V in the model corresponds to the volume within which the σ field is homogenous we should think of V as a parameter in the toy model just as ξ is. The model treats only the zero-momentum mode $\sigma = \int_x \sigma(\boldsymbol{x})/V$ of the critical field, ignoring all other modes, i.e., the space variation of the field $\sigma(\boldsymbol{x})$. This means, in particular, that it ignores the fact that the correlations are exponentially small between regions of space separated by distances further than ξ. For this reason we should not choose a value of $V^{1/3}$ that is very much larger than ξ.

As an example, in Fig. A-1 we plot the toy model probability distribution for the number of protons, $\mathcal{P}(N_p)$ of (A.1), with $\xi = 2$ fm, $\tilde{\lambda}_3$ and $\tilde{\lambda}_4$ taking their benchmark values, $\mu_B = 400$ MeV, $V = (5\,\text{fm})^3$ and $g_p = 6.185$. We can then evaluate the mean

and cumulants of this toy model probability distribution, and we find

$$
\begin{aligned}
\langle N_p \rangle^{\text{model}} &= 5.2, \\
\omega_{2p}^{\text{model}} &= 4.5, \\
\omega_{3p}^{\text{model}} &= 37, \\
\omega_{4p}^{\text{model}} &= 405.
\end{aligned}
\tag{A.6}
$$

We chose all parameters in the toy model at their benchmark values with the exception of g_p, whose benchmark value is 7. We chose $g_p = 6.185$ in the toy model in order to get a probability distribution whose fourth cumulant is similar to that we calculated in Section 2.2.2. In our full calculation of Section 2.2.2, with $\xi = 2$ fm, $\mu_B = 400$ MeV, and all parameters at their benchmark values including in particular $g_p = 7$ we obtain

$$
\begin{aligned}
\langle N_p \rangle &= 3.0, \\
\omega_{2p} &= 4.2, \\
\omega_{3p} &= 30, \\
\omega_{4p} &= 405 ,
\end{aligned}
\tag{A.7}
$$

where we have quoted $\langle N_p \rangle = V n_p$ for $V = (5 \text{ fm})^3$. (The ω's calculated in Section 2.2 are intensive, meaning that they are the same for any choice of V.) We see that the distribution in Fig. A-1 has cumulants that are similar to those we calculated in Section 2.2.2, including in particular having as dramatically large a value of ω_{4p}. We see from the Figure that an ω_{4p} that is ~ 400 times larger than the Poisson value does not indicate an unusual looking distribution. We can also note that the large positive 4th cumulant is a consequence of the skewness of the distribution. If the distribution were symmetric, the large positive 4th cumulant would indicate a highly peaked distribution, but not so here.

We can also use our toy model to make a crude estimate of how our results for the cumulants would be affected by an upper cutoff on N_p. In a heavy-ion collision, N_p (say in one unit of rapidity) cannot fluctuate to arbitrarily large values. We can

implement this in the toy model by putting an upper cutoff on N_p. Lets assume that the neutrons are fluctuating with the protons, as is in fact expected [112]. It seems clear that nucleon-nucleon repulsion (that we have not taken into consideration) would cut off upward fluctuations in N_p somewhere below those that correspond to nucleon densities of $1/\text{fm}^3$, meaning ~ 60 protons per $(5\text{ fm})^3$ volume. To get a sense of the size of these effects, we tried cutting off the distribution in Fig. A-1 at $N_p = 30$. We find

$$
\begin{aligned}
\langle N_p \rangle^{\text{cutoff model}} &= 5.1 \ , \\
\omega_{2p}^{\text{cutoff model}} &= 4.4 \ , \\
\omega_{3p}^{\text{cutoff model}} &= 33 \ , \\
\omega_{4p}^{\text{cutoff model}} &= 289 \ .
\end{aligned}
\tag{A.8}
$$

We see that a cutoff like this has little effect on the 2nd and 3rd cumulants, but it does reduce ω_{4p} by 28%. (See also Ref. [120] for a study of the effects of introducing a cutoff at large N_p in the absence of critical fluctuations.)

Appendix B

Mean Transverse Momentum Fluctuations Near the Critical Point

The correlators found in Chapter 2, Section 2.2.1 can also be used to estimate the effect of the long wavelength fluctuations in the vicinity of the critical point on higher cumulants of the mean transverse momentum p_T. For example, the cubic cumulant of the mean p_T distribution around the all event mean $\overline{p_T}$, namely $\kappa_3(\delta p_T)$, is given by

$$\kappa_3(\delta p_T) \equiv \langle\langle (p_T - \overline{p_T})^3 \rangle\rangle$$

$$= \frac{1}{\left(\int_k \langle n_k \rangle\right)^3} \int_{k_1} \int_{k_2} \int_{k_3} ([k_1]_T - \overline{p_T})([k_2]_T - \overline{p_T})([k_3]_T - \overline{p_T}) \langle\langle \delta n_{k_1} \delta n_{k_2} \delta n_{k_3} \rangle\rangle \,,$$

$$\text{(B.1)}$$

and similarly for $\kappa_4(\delta p_T)$. We can normalize $\kappa_k(\delta p_T)$ by defining a dimensionless and intensive variable F_k:

$$F_k \equiv \frac{\langle N \rangle^{k-1} \kappa_k(\delta p_T)}{v_{\text{inc}}^k(p_T)}, \qquad \text{(B.2)}$$

where $\langle N \rangle$ is the total particle multiplicity and $v_{\text{inc}}^2(p_T)$ is the variance of the inclusive (single-particle) p_T-distribution, defined as

$$v_{\text{inc}}^2(p_T) = \frac{1}{\int_k \langle n_k \rangle} \int_k (k_T - \overline{p_T})^2 \langle n_k \rangle \ . \tag{B.3}$$

Upon evaluating (B.2) using the correlators given in Section 2.2.1, we obtain the critical contribution to F_k. For pions with $\mu_\pi = 0$ at $T = 120$ MeV and $\xi = 2$ fm, we find

$$F_3^\sigma = -0.0131 \quad \text{and} \quad F_4^\sigma = 0.0177. \tag{B.4}$$

In addition to the critical point contribution, expression (B.2) receives contributions from Poisson statistics, Bose-Einstein enhancement, resonances, effects of radial flow, etc. It was shown in [30] that the effects of resonances and radial flow are very small and hence we will ignore them. Here we compare the critical point contribution to that coming from Bose-Einstein enhancement. The 3- and 4-particle correlators for an ideal Bose gas are given by

$$\langle\langle (\delta n_k)^3 \rangle\rangle_{\text{BE}} = \langle n_k \rangle (\langle n_k \rangle + 1)(2\langle n_k \rangle + 1), \tag{B.5}$$

$$\langle\langle (\delta n_k)^4 \rangle\rangle_{\text{BE}} = \langle n_k \rangle (\langle n_k \rangle + 1)(1 + 6\langle n_k \rangle (\langle n_k \rangle + 1)), \tag{B.6}$$

where here by $\langle n_k \rangle$ we mean the mean occupation number for an ideal Bose gas. Evaluating (B.2) using the above correlators will give us the Bose-Einstein and the Poisson contribution to F_k. In order to isolate the Bose-Einstein effect we subtract the Poisson contribution $\langle n_k \rangle$ from κ_k and then evaluate F_k. Using the same parameters as above we find

$$F_3^{\text{BE}} = -0.2480 \quad \text{and} \quad F_4^{\text{BE}} = 0.9388. \tag{B.7}$$

We see that the contribution of critical fluctuations is smaller than that due to Bose-Einstein effects. We conclude that it would be very difficult to use higher cumulants of the mean p_T distribution in order to search for the critical point. Furthermore, as kinetic freeze-out (where particle momenta freeze) occurs after chemical freeze-out (where particle numbers freeze), it is easier for p_T fluctuations to get washed out (see,

e.g. Ref. [121]), making them even less favorable observables in searching for the critical point.

Bibliography

[1] B. Barrois, Nucl. Phys. **B129**, 390 (1977); S. Frautschi, Proceedings of workshop on hadronic matter at extreme density, Erice 1978; B. Barrois, "Nonperturbative effects in dense quark matter," Cal Tech PhD thesis, UMI 79-04847-mc (1979).

[2] D. Bailin and A. Love, Phys. Rept. **107**, 325 (1984), and references therein.

[3] M. Alford, K. Rajagopal and F. Wilczek, Phys. Lett. **B422**, 247 (1998) [hep-ph/9711395].

[4] R. Rapp, T. Schafer, E. V. Shuryak and M. Velkovsky, Phys. Rev. Lett. **81**, 53 (1998) [hep-ph/9711396].

[5] M. Alford, K. Rajagopal and F. Wilczek, Nucl. Phys. **B537**, 443 (1999) [hep-ph/9804403].

[6] M. G. Alford, K. Rajagopal, T. Schaefer and A. Schmitt, Rev. Mod. Phys. **80**:1455-1515, 2008 [arXiv:0709.4635]

[7] **PHENIX** Collaboration, K. Adcox *et al.*, "Formation of dense partonic matter in relativistic nucleus nucleus collisions at RHIC: Experimental evaluation by the PHENIX collaboration," *Nucl. Phys.* **A757** (2005) 184–283, arXiv:nucl-ex/0410003.

[8] B. B. Back *et al.*, "The PHOBOS perspective on discoveries at RHIC," *Nucl. Phys.* **A757** (2005) 28–101, arXiv:nucl-ex/0410022.

[9] **BRAHMS** Collaboration, I. Arsene *et al.*, "Quark Gluon Plasma an Color Glass Condensate at RHIC? The perspective from the BRAHMS experiment," *Nucl. Phys.* **A757** (2005) 1–27, arXiv:nucl-ex/0410020.

[10] **STAR** Collaboration, J. Adams *et al.*, "Experimental and theoretical challenges in the search for the quark gluon plasma: The STAR collaboration's critical assessment of the evidence from RHIC collisions," *Nucl. Phys.* **A757** (2005) 102–183, arXiv:nucl-ex/0501009.

[11] STAR Collaboration, J. Adams et al., "Azimuthal anisotropy in Au + Au collisions at s(NN)**(1/2) = 200-GeV," Phys. Rev. **C72** (2005) 014904 [arXiv:nucl-ex/0409033].

[12] F. R. Brown *et al.*, Phys. Rev. Lett. **65** (1990) 2491.

[13] M. Asakawa and K. Yazaki, Nucl. Phys. A **504** (1989) 668; A. Barducci, R. Casalbuoni, S. De Curtis, R. Gatto and G. Pettini, Phys. Lett. B **231** (1989) 463; Phys. Rev. D **41** (1990) 1610; A. Barducci, R. Casalbuoni, G. Pettini and R. Gatto, Phys. Rev. D **49** (1994) 426; J. Berges and K. Rajagopal, Nucl. Phys. B **538** (1999) 215 [arXiv:hep-ph/9804233]; M. A. Halasz, A. D. Jackson, R. E. Shrock, M. A. Stephanov and J. J. M. Verbaarschot, Phys. Rev. D **58** (1998) 096007 [arXiv:hep-ph/9804290]; O. Scavenius, A. Mocsy, I. N. Mishustin and D. H. Rischke, Phys. Rev. C **64** (2001), 045202 [arXiv:nucl-th/0007030]; N. G. Antoniou and A. S. Kapoyannis, Phys. Lett. B **563** (2003) 165 [arXiv:hepph/0211392]; Y. Hatta and T. Ikeda, Phys. Rev. D **67** (2003) 014028 [arXiv:hep-ph/0210284].

[14] M. A. Stephanov, Prog. Theor. Phys. Suppl. **153**, 139 (2004) [Int. J. Mod. Phys. A **20**, 4387 (2005)] [arXiv:hep-ph/0402115].

[15] C. Schmidt, PoS **LAT2006**, 021 (2006) [arXiv:hep-lat/0610116].

[16] M. A. Stephanov, PoS **LAT2006**, 024 (2006) [arXiv:hep-lat/0701002].

[17] V. Koch, arXiv:0810.2520 [nucl-th].

[18] S. Gupta, arXiv:0909.4630 [nucl-ex].

[19] O. Philipsen, arXiv:0910.0785 [hep-ph].

[20] C. Schmidt, arXiv:0910.4321 [hep-lat].

[21] A. Li, arXiv:1002.4459 [hep-lat].

[22] K. Fukushima and T. Hatsuda, arXiv:1005.4814 [hep-ph].

[23] M. M. Aggarwal *et al.*, arXiv:1004.4959 [nucl-ex].

[24] A. Andronic, P. Braun-Munzinger, and J. Stachel, "Hadron production in central nucleus nucleus collisions at chemical freeze-out," Nucl. Phys. **A772** (2006) 167-199 [arXiv:nucl-th/0511071].

[25] P. Braun-Munzinger, K. Redlich, and J. Stachel, "Particle production in heavy ion collisions," [arXiv:nucl-th/0304013].

[26] J. Cleymans, H. Oeschler, K. Redlich and S. Wheaton, Phys. Rev. C **73**, 034905 (2006) [arXiv:hep-ph/0511094].

[27] B. Berdnikov and K. Rajagopal, Phys. Rev. D **61**, 105017 (2000) [arXiv:hep-ph/9912274].

[28] D. T. Son and M. A. Stephanov, Phys. Rev. D **70**, 056001 (2004) [arXiv:hep-ph/0401052].

[29] C. Nonaka and M. Asakawa, Phys. Rev. C **71**, 044904 (2005) [arXiv:nucl-th/0410078].

[30] M. A. Stephanov, K. Rajagopal and E. V. Shuryak, Phys. Rev. D **60**, 114028 (1999) [arXiv:hep-ph/9903292].

[31] M. A. Stephanov, K. Rajagopal and E. V. Shuryak, Phys. Rev. Lett. **81**, 4816 (1998) [arXiv:hep-ph/9806219].

[32] M. A. Stephanov, Phys. Rev. Lett. **102**, 032301 (2009) [arXiv:0809.3450 [hep-ph]].

[33] D. Teaney, "Effect of shear viscosity on spectra, elliptic flow, and Hanbury Brown-Twiss radii," Phys. Rev. C **68**, 034913 (2003) [arXiv:nucl-th/0301099].

[34] K. Dusling and D. Teaney, "Simulating elliptic flow with viscous hydrodynamics," Phys. Rev. C **77**, 034905 (2008) [arXiv:0710.5932 [nucl-th]].

[35] M. Luzum and P. Romatschke, "Conformal Relativistic Viscous Hydrodynamics: Applications to RHIC results a: sqrt(sNN) = 200 GeV," Phys. Rev. C **78**, 034915 (2008) [Erratum-ibid. C 79, 039903 (2009)] [arXiv:0804.4015 [nucl-th]].

[36] D. T. Son and A. O. Starinets, "Visocisty, Black Holes, and Quantum Field theory" Ann. Rev. Nucl. Part. Sci. **57**, 95 (2007) [arXiv:0704.0240 [hep-th]].

[37] P. Kovtun, D. T. Son, A. O. Starinets, "Viscosity in Strongly Interacting Quantum Field Theories from Black Hole Physics" [arXiv:hep-th/0405231v2]

[38] F. Karsch, D. Kharzeev and H. Satz, Phys. Lett. B **637**, 75 (2006)

[39] S. Digal, P. Petreczky and H. Satz, Phys. Lett. B **514**, 57 (2001); H. Satz [arXiv:hep-ph/0609197]

[40] T. Matsui and H. Satz, "J / Psi Suppression By Quark - Gluon Plasma Formation," Phys. Lett. B **178**, 416 (1986).

[41] B. Alessandro *et al.* [NA50 Collaboration], Eur. Phys. J. C **39**, 335 (2005); R. Arnaldi et al. [NA60 Collaboration], Nucl. Phys. A **783**, 261-268 (2007) [arXiv:nucl-ex/0701033v1]; H.Pereira da Costa. [PHENIX Collaboration], Nucl. Phys. A **774** 747-750 (2006) [arXiv:nucl-ex/0510051v1].

[42] H. Liu, K. Rajagopal and U. A. Wiedemann, Phys. Rev. Lett. **98**, 182301 (2007) [arXiv:hep-ph/0607062].

[43] STAR Collaboration, J. Adams *et al.*, "Distributions of charged hadrons associated with high transverse momentum particles in p p and Au + Au collisions at s(NN)**(1/2) = 200-GeV," Phys. Rev. Lett. **95** (2005) 152301, [arXiv:nucl-ex/0501016].

[44] Jorge Casalderrey-Solana, Hong Liu, David Mateos, Krishna Rajagopal, Urs Achim Wiedemann, "Gauge/String Duality, Hot QCD and Heavy Ion Collisions" [arXiv:1101.0618v1]

[45] H. Liu, K. Rajagopal, and U. A. Wiedemann, "Calculating the jet quenching parameter from AdS/CFT," Phys. Rev. Lett. **97** (2006) 182301, [arXiv:hep-ph/0605178].

[46] H. Liu, K. Rajagopal, and U. A. Wiedemann, "Wilson loops in heavy ion collisions and their calculation in AdS/CFT," JHEP **03** (2007) 066 [arXiv:hep-ph/0612168].

[47] F. D'Eramo, H. Liu, and K. Rajagopal, "Jet Quenching Parameter via Soft Collinear Effective Theory (SCET)" [arXiv:1010.0890 [hep-ph]].

[48] E. Caceres and A. Guijosa, "On Drag Forces and Jet Quenching in Strongly Coupled Plasmas," JHEP **12** (2006) 068 [arXiv:hep-th/0606134].

[49] E. Nakano, S. Teraguchi, and W.-Y. Wen, "Drag Force, Jet Quenching, and AdS/QCD," Phys. Rev. **D75** (2007) 085016 [arXiv:hep-ph/060827].

[50] U. Gursoy, E. Kiritsis, G. Michalogiorgakis, and F. Nitti, "Thermal Transport and Drag Force in Improved Holographic QCD," JHEP **12** (2009) 056, [arXiv:0906.1890 [hep-ph]].

[51] C. Hoyos-Badajoz, "Drag and jet quenching of heavy quarks in a strongly coupled N=2* plasma," JHEP **09** (2009) 068 [arXiv:0907.5036 [hep-th]].

[52] A. Buchel, "On jet quenching parameters in strongly coupled non- conformal gauge theories," Phys. Rev. **D74** (2006) 046006 [arXiv:hep-th/0605178].

[53] F.-L. Lin and T. Matsuo, "Jet quenching parameter in medium with chemical potential from AdS/CFT," Phys. Lett. **B641** (2006) 45-49 [arXiv:hep-th/0606136].

[54] S. D. Avramis and K. Sfetsos, "Supergravity and the jet quenching parameter in the presence of R-charge densities," JHEP **01** (2007) 065 [arXiv:hep-th/0606190].

[55] N. Armesto, J. D. Edelstein, and J. Mas, "Jet quenching at finite 't Hooft coupling and chemical potential from AdS/CFT," JHEP **09** (2006) 039 [arXiv:hep-ph/0606245].

[56] D. M. Hofman and J. Maldacena, "Conformal collider physics: Energy and charge correlations," *JHEP* **05** (2008) 012, arXiv:0803.1467 [hep-th].

[57] P. M. Chesler, K. Jensen, and A. Karch, "Jets in strongly-coupled N = 4 super Yang-Mills theory," *Phys. Rev.* **D79** (2009) 025021, arXiv:0804.3110 [hep-th].

[58] Y. Hatta, E. Iancu, and A. H. Mueller, "Jet evolution in the N=4 SYM plasma at strong coupling," *JHEP* **05** (2008) 037, arXiv:0803.2481 [hep-th].

[59] G. 't Hooft, "Dimensional reduction in quantum gravity," [arXiv:gr-qc/9310026].

[60] L. Susskind, "The World as a hologram," J. Math. Phys. **36** (1995) 6377-6396, [arXiv:hep-th/9409089].

[61] J. M. Maldacena, "The large N limit of superconformal field theories and super-gravity," *Adv. Theor. Math. Phys.* **2** (1998) 231–252, arXiv:hep-th/9711200.

[62] E. Witten, "Anti-de Sitter space and holography," Adv. Theor. Math. Phys. **2**, 253 (1998) [arXiv:hep-th/9802150].

[63] S. S. Gubser, I. R. Klebanov and A. M. Polyakov, "Gauge theory correlators from non-critical string theory," Phys. Lett. B **428**, 105 (1998) [arXiv:hepth/9802109].

[64] O. Aharony, S. S. Gubser, J. M. Maldacena, H. Ooguri and Y. Oz, "Large N field theories, string theory and gravity," Phys. Rept. **323**, 183 (2000) [arXiv:hepth/9905111].

[65] L. Susskind and E. Witten, arXiv:hep-th/9805114; A. W. Peet and J. Polchinski, Phys. Rev. D **59**, 065011 (1999) [arXiv:hep-th/9809022].

[66] E. Witten, "Anti-de Sitter Space, Thermal Phase Transition, And Confinement In Gauge Theories", *Adv. Theor. Math. Phys.* **2** (1998) 505–532 [arXiv:hep-th/9803131v2].

[67] S. S. Gubser, I. R. Klebanov and A. M. Polyakov, "Gauge theory correlators from non-critical string theory," Phys. Lett. B **428**, 105 (1998) [arXiv:hepth/9802109].

[68] E. Witten, "Anti-de Sitter space and holography," Adv. Theor. Math. Phys. **2**, 253 (1998) [arXiv:hep-th/9802150].

[69] O. Aharony, A. Fayyazuddin, and J. M. Maldacena, "The large N limit of N = 2,1field theories from three- branes in F-theory," JHEP **07** (1998) 013 [arXiv:hep-th/9806159].

[70] A. Karch and L. Randall, "Open and closed string interpretation of SUSY CFT's on branes with boundaries," JHEP **06** (2001) 063 [arXiv:hep-th/0105132].

[71] A. Karch and E. Katz, "Adding flavor to AdS/CFT," JHEP **06** (2002) 043 [arXiv:hep-th/0205236].

[72] M. Cheng *et al.*, "The QCD Equation of State with almost Physical Quark Masses," [arXiv:0710.0354 [hep-lat]].

[73] S. Borsanyi *et al.*, "The QCD equation of state with dynamical quarks," [arXiv:1007.2580 [hep-lat]].

[74] H. B. Meyer, "A calculation of the bulk viscosity in SU(3) gluodynamics," Phys. Rev. Lett. **100** (2008) 162001 [arXiv:0710.3717 [hep-lat]].

[75] S. S. Gubser, I. R. Klebanov, and A. W. Peet, "Entropy and Temperature of Black 3-Branes," Phys. Rev. **D54** (1996) 3915-3919 [arXiv:hep-th/9602135].

[76] For recent reviews, see J. Phys. Conf. Ser. **46**, 122 (2006) [arXiv:hep-lat/0608003]; F. Karsch, [arXiv:hep-ph/0610024].

[77] F. Karsch, Nucl. Phys. A **698**, 199 (2002) [arXiv:hep-ph/0103314].

[78] F. Karsch, E. Laermann and A. Peikert, Phys. Lett. B **478**, 447 (2000) [arXiv:hep-lat/0002003].

[79] P. Kovtun, D. T. Son, and A. O. Starinets, Holography and hydrodynamics: "Diusion on stretched horizons," JHEP **10** (2003) 064 [arXiv:hep-th/0309213].

[80] A. Buchel and J. T. Liu, "Universality of the shear viscosity in supergravity," Phys. Rev. Lett. **93** (2004) 090602 [arXiv:hep-th/0311175].

[81] A. Buchel, "On universality of stress-energy tensor correlation functions in supergravity," Phys. Lett. **B609** (2005) 392401 [arXiv:hep-th/0408095].

[82] G. Policastro, D. Son and A. Starinets, "The Shear viscosity of strongly coupled N=4 supersymmetric Yang-Mills plasma," Phys. Rev. Lett. **87** (2001) 081601, [arXiv:hep-th/0104066].

[83] C. P. Herzog, A. Karch, P. Kovtun, C. Kozcaz and L. G. Yaffe, JHEP **0607**, 013 (2006) [arXiv:hep-th/0605158].

[84] S. S. Gubser, Phys. Rev. D **74**, 126005 (2006) [arXiv:hep-th/0605182];

[85] C. P. Herzog, "Energy loss of heavy quarks from asymptotically AdS geometries," JHEP **09** (2006) 032 [arXiv:hep-th/0605191].

[86] E. Caceres and A. Guijosa, "Drag force in charged N = 4 SYM plasma," JHEP **11** (2006) 077 [arXiv:hep-th/0605235].

[87] E. Caceres and A. Guijosa, "On Drag Forces and Jet Quenching in Strongly Coupled Plasmas," JHEP **12** (2006) 068 [arXiv:hep-th/0606134].

[88] T. Matsuo, D. Tomino, and W.-Y. Wen, "Drag force in SYM plasma with B field from AdS/CFT," JHEP **10** (2006) 055 [arXiv:hep-th/0607178].

[89] E. Nakano, S. Teraguchi, and W.-Y. Wen, "Drag Force, Jet Quenching, and AdS/QCD," Phys. Rev. **D75** (2007) 085016 [arXiv:hep-ph/0608274].

[90] P. Talavera, "Drag force in a string model dual to large-N QCD," JHEP **01** (2007) 086, [arXiv:hep-th/0610179].

[91] S. S. Gubser, "Comparing the drag force on heavy quarks in N = 4 super-Yang-Mills theory and QCD," Phys. Rev. **D76** (2007) 126003 [arXiv:hep-th/0611272].

[92] U. Gursoy, E. Kiritsis, G. Michalogiorgakis, and F. Nitti, "Thermal Transport and Drag Force in Improved Holographic QCD," JHEP **12** (2009) 056 [arXiv:0906.1890 [hep-ph]].

[93] C. Hoyos-Badajoz, "Drag and jet quenching of heavy quarks in a strongly coupled N=2* plasma," JHEP **09** (2009) 068 [arXiv:0907.5036 [hep-th]].

[94] V. E. Hubeny, "Holographic dual of collimated radiation," [arXiv:1012.3561].

[95] C. Athanasiou, K. Rajagopal and M. Stephanov, Phys. Rev. D **82**, 074008 (2010) [arXiv:1006.4636]

[96] C. Athanasiou, H. Liu and K. Rajagopal, JHEP **05** (2008) 083 [arXiv:0801.1117]

[97] C. Athanasiou, P. M. Chesler, H. Liu, D. Nickel and K. Rajagopal, Phys. Rev. D **81**, 126001 (2010) [arXiv:1001.3880]

[98] G. S. F. Stephans, J. Phys. G **35**, 044050 (2008).

[99] B. Mohanty, Nucl. Phys. A **830**, 899C (2009) [arXiv:0907.4476 [nucl-ex]].

[100] T. Schuster, for the NA49 Collaboration, PoS C **POD2009**, 029 (2009) [arXiv:0910.0558 [nucl-ex]].

[101] G. Stepanek, for the NA61 Collaboration, arXiv:0908.1697 [nucl-ex].

[102] B. B. Back *et al.* [PHOBOS Collaboration], Nucl. Phys. A **757**, 28 (2005) [arXiv:nucl-ex/0410022]; I. Arsene *et al.* [BRAHMS Collaboration]; Nucl. Phys. A **757**, 1 (2005) [arXiv:nucl-ex/0410020]; J. Adams *et al.* [STAR Collaboration], Nucl. Phys. A **757**, 102 (2005) [arXiv:nucl-ex/0501009];

[103] Z. Fodor and S. D. Katz, JHEP **0404**, 050 (2004) [arXiv:hep-lat/0402006].

[104] C. R. Allton *et al.*, Phys. Rev. D **71**, 054508 (2005) [arXiv:hep-lat/0501030].

[105] R. V. Gavai and S. Gupta, Phys. Rev. D **78**, 114503 (2008) [arXiv:0806.2233 [hep-lat]].

[106] P. de Forcrand and O. Philipsen, JHEP **0811**, 012 (2008) [arXiv:0808.1096 [hep-lat]].

[107] M. A. Stephanov, Phys. Rev. D **65**, 096008 (2002) [arXiv:hep-ph/0110077].

[108] R. Guida and J. Zinn-Justin, J. Phys. A **31**, 8103 (1998) [arXiv:cond-mat/9803240].

[109] J. Zinn-Justin, "Quantum Field Theory and Critical Phenomena," Oxford, UK: Oxford University Press, Oxford (1989).

[110] Y. Hatta and T. Ikeda, Phys. Rev. D **67**, 014028 (2003) [arXiv:hep-ph/0210284].

[111] S. Gupta, private communication.

[112] Y. Hatta and M. A. Stephanov, Phys. Rev. Lett. **91**, 102003 (2003) [Erratum-ibid. **91**, 129901 (2003)] [arXiv:hep-ph/0302002].

[113] V. P. Konchakovski, M. Hauer, G. Torrieri, M. I. Gorenstein and E. L. Bratkovskaya, Phys. Rev. C **79**, 034910 (2009) [arXiv:0812.3967].

[114] M. M. Tsypin, Phys. Rev. Lett. **73**, 2015 (1994); M. M. Tsypin, arXiv:hep-lat/9601021.

[115] J. I. Kapusta and C. Gale, "Finite-Temperature Field Theory Principles and Applications," Cambridge, UK: Cambridge University Press (2006)

[116] S. Jeon and V. Koch, Phys. Rev. Lett. **85**, 2076 (2000) [arXiv:hep-ph/0003168].

[117] M. Asakawa, U. W. Heinz and B. Muller, Phys. Rev. Lett. **85**, 2072 (2000) [arXiv:hep-ph/0003169].

[118] E. V. Shuryak and M. A. Stephanov, Phys. Rev. C **63**, 064903 (2001) [arXiv:hep-ph/0010100].

[119] S. Jeon and V. Koch, arXiv:hep-ph/0304012.

[120] T. Schuster, M. Nahrgang, M. Mitrovski, R. Stock and M. Bleicher, arXiv:0903.2911 [hep-ph].

[121] M. A. Stephanov, Phys. Rev. D **81**, 054012 (2010) [arXiv:0911.1772 [hep-ph]].

[122] S. J. Rey and J. T. Yee, Eur. Phys. J. C **22**, 379 (2001) [arXiv:hep-th/9803001].

[123] J. M. Maldacena, Phys. Rev. Lett. **80**, 4859 (1998) [arXiv:hep-th/9803002].

[124] S. J. Rey, S. Theisen and J. T. Yee, Nucl. Phys. B **527**, 171 (1998) [arXiv:hep-th/9803135]; A. Brandhuber, N. Itzhaki, J. Sonnenschein and S. Yankielowicz, Phys. Lett. B **434**, 36 (1998) [arXiv:hep-th/9803137]; J. Sonnenschein, arXiv:hep-th/0003032.

[125] D. Bak, A. Karch and L. G. Yaffe, JHEP **0708**, 049 (2007) [arXiv:0705.0994 [hep-th]].

[126] For a review, see F. Karsch, Nucl. Phys. A **783**, 13 (2007) [arXiv:hep-ph/0610024].

[127] O. Kaczmarek and F. Zantow, Phys. Rev. D **71**, 114510 (2005) [arXiv:hep-lat/0503017].

[128] O. Kaczmarek, F. Karsch, F. Zantow and P. Petreczky, Phys. Rev. D **70**, 074505 (2004) [Erratum-ibid. D **72**, 059903 (2005)] [arXiv:hep-lat/0406036].

[129] H. Liu, K. Rajagopal and U. A. Wiedemann, JHEP **0703**, 066 (2007) [arXiv:hep-ph/0612168].

[130] K. Peeters, J. Sonnenschein and M. Zamaklar, Phys. Rev. D **74**, 106008 (2006) [arXiv:hep-th/0606195]; M. Chernicoff, J. A. Garcia and A. Guijosa, JHEP **0609**, 068 (2006) [arXiv:hep-th/0607089]; see also Appendix A of Ref. [83].

[131] S. D. Avramis, K. Sfetsos and D. Zoakos, Phys. Rev. D **75**, 025009 (2007) [arXiv:hep-th/0609079].

[132] E. Caceres, M. Natsuume and T. Okamura, JHEP **0610**, 011 (2006) [arXiv:hep-th/0607233].

[133] M. Natsuume and T. Okamura, JHEP **0709**, 039 (2007) [arXiv:0706.0086 [hep-th]].

[134] Q. J. Ejaz, T. Faulkner, H. Liu, K. Rajagopal and U. A. Wiedemann, arXiv:0712.0590 [hep-th].

[135] A. Karch and E. Katz, JHEP **0206**, 043 (2002) [arXiv:hep-th/0205236]; M. Kruczenski, D. Mateos, R. C. Myers and D. J. Winters, JHEP **0307**, 049 (2003) [arXiv:hep-th/0304032]; J. Babington, J. Erdmenger, N. J. Evans, Z. Guralnik and I. Kirsch, Phys. Rev. D **69**, 066007 (2004) [arXiv:hep-th/0306018]; M. Kruczenski, D. Mateos, R. C. Myers and D. J. Winters, JHEP **0405**, 041 (2004) [arXiv:hep-th/0311270].

[136] R. Sommer and J. Wosiek, Nucl. Phys. B **267**, 531 (1986); G. S. Bali, Phys. Rept. **343**, 1 (2001) [arXiv:hep-ph/0001312]; T. T. Takahashi, H. Matsufuru,

Y. Nemoto and H. Suganuma, Phys. Rev. Lett. **86**, 18 (2001) [arXiv:hep-lat/0006005]; C. Alexandrou, P. De Forcrand and A. Tsapalis, Phys. Rev. D **65**, 054503 (2002) [arXiv:hep-lat/0107006]; C. Alexandrou, P. de Forcrand and A. Tsapalis, Nucl. Phys. Proc. Suppl. **109A**, 153 (2002) [arXiv:nucl-th/0111046]; T. T. Takahashi, H. Suganuma, Y. Nemoto and H. Matsufuru, Phys. Rev. D **65**, 114509 (2002) [arXiv:hep-lat/0204011]; C. Alexandrou, P. de Forcrand and O. Jahn, Nucl. Phys. Proc. Suppl. **119**, 667 (2003) [arXiv:hep-lat/0209062]; O. Jahn and P. de Forcrand, Nucl. Phys. Proc. Suppl. **129**, 700 (2004) [arXiv:hep-lat/0309115]; T. T. Takahashi and H. Suganuma, Phys. Rev. D **70**, 074506 (2004) [arXiv:hep-lat/0409105]; Ph. de Forcrand and O. Jahn, Nucl. Phys. A **755**, 475 (2005) [arXiv:hep-ph/0502039].

[137] K. Hubner, F. Karsch, O. Kaczmarek and O. Vogt, arXiv:0710.5147 [hep-lat].

[138] E. Witten, JHEP **9807**, 006 (1998) [arXiv:hep-th/9805112].

[139] D. J. Gross and H. Ooguri, Phys. Rev. D **58**, 106002 (1998) [arXiv:hep-th/9805129].

[140] A. Brandhuber, N. Itzhaki, J. Sonnenschein and S. Yankielowicz, JHEP **9807**, 020 (1998) [arXiv:hep-th/9806158].

[141] Y. Imamura, Nucl. Phys. B **537**, 184 (1999) [arXiv:hep-th/9807179]; C. G. Callan, A. Guijosa and K. G. Savvidy, Nucl. Phys. B **547**, 127 (1999) [arXiv:hep-th/9810092]; B. Craps, J. Gomis, D. Mateos and A. Van Proeyen, JHEP **9904**, 004 (1999) [arXiv:hep-th/9901060]; C. G. Callan, A. Guijosa, K. G. Savvidy and O. Tafjord, Nucl. Phys. B **555**, 183 (1999) [arXiv:hep-th/9902197]; J. Gomis, A. V. Ramallo, J. Simon and P. K. Townsend, JHEP **9911**, 019 (1999) [arXiv:hep-th/9907022].

[142] G. C. Rossi and G. Veneziano, Nucl. Phys. B **123**, 507 (1977); B. Z. Kopeliovich and B. G. Zakharov, Z. Phys. C **43**, 241 (1989); D. Kharzeev, Phys. Lett. B **378**, 238 (1996) [arXiv:nucl-th/9602027]; M. Gyulassy, V. Topor Pop

and S. E. Vance, Heavy Ion Phys. **5**, 299 (1997) [arXiv:nucl-th/9706048]; H. W. Fricke and C. C. Noack, Phys. Rev. Lett. **80**, 3014 (1998) [arXiv:hep-ph/9711389]; S. E. Vance, M. Gyulassy and X. N. Wang, Phys. Lett. B **443**, 45 (1998) [arXiv:nucl-th/9806008]; B. Kopeliovich and B. Povh, Phys. Lett. B **446**, 321 (1999) [arXiv:hep-ph/9810530]; S. E. Vance and M. Gyulassy, Phys. Rev. Lett. **83**, 1735 (1999) [arXiv:nucl-th/9901009]; I. Vitev and M. Gyulassy, Phys. Rev. C **65**, 041902 (2002) [arXiv:nucl-th/0104066]; G. H. Arakelian, A. Capella, A. B. Kaidalov and Yu. M. Shabelski, Eur. Phys. J. C **26**, 81 (2002); V. T. Pop, M. Gyulassy, J. Barrette, C. Gale, X. N. Wang and N. Xu, Phys. Rev. C **70**, 064906 (2004) [arXiv:nucl-th/0407095];

[143] M. C. Chu and T. Matsui, Phys. Rev. D **39**, 1892 (1989).

[144] F. Karsch, E. Laermann and A. Peikert, Phys. Lett. B **478**, 447 (2000) [arXiv:hep-lat/0002003]; F. Karsch, Nucl. Phys. A **698**, 199 (2002) [arXiv:hep-ph/0103314].

[145] J. J. Friess, S. S. Gubser, G. Michalogiorgakis and S. S. Pufu, JHEP **0704**, 079 (2007) [arXiv:hep-th/0609137]; S. D. Avramis, K. Sfetsos and K. Siampos, Nucl. Phys. B **769**, 44 (2007) [arXiv:hep-th/0612139]; S. D. Avramis, K. Sfetsos and K. Siampos, arXiv:0706.2655 [hep-th].

[146] M. Chernicoff and A. Guijosa, JHEP **02**, 084 (2007) [arXiv:hep-th/0611155].

[147] J. D. Jackson, *Classical Electrodynamics*. Wiley, 3rd ed., 1999.

[148] A. Mikhailov, "Nonlinear waves in AdS/CFT correspondence," arXiv:hep-th/0305196.

[149] A. Liénard *L'Éclairage Électrique* **16** (1898) 5.

[150] C. L. Basham, L. S. Brown, S. D. Ellis, and S. T. Love, "Energy Correlations in electron-Positron Annihilation in Quantum Chromodynamics: Asymptotically Free Perturbation Theory," *Phys. Rev.* **D19** (1979) 2018.

[151] C. L. Basham, L. S. Brown, S. D. Ellis, and S. T. Love, "Energy Correlations in electron - Positron Annihilation: Testing QCD," *Phys. Rev. Lett.* **41** (1978) 1585.

[152] C. L. Basham, L. S. Brown, S. D. Ellis, and S. T. Love, "Electron - Positron Annihilation Energy Pattern in Quantum Chromodynamics: Asymptotically Free Perturbation Theory," *Phys. Rev.* **D17** (1978) 2298.

[153] P. M. Chesler, A. Gynther, and A. Vuorinen, "On the dispersion of fundamental particles in QCD and N=4 Super Yang-Mills theory," *JHEP* **09** (2009) 003, arXiv:0906.3052 [hep-ph].

[154] J. D. Brown and J. W. York, Jr., "Quasilocal energy and conserved charges derived from the gravitational action," *Phys. Rev.* **D47** (1993) 1407–1419, arXiv:gr-qc/9209012.

[155] S. de Haro, S. N. Solodukhin, and K. Skenderis, "Holographic reconstruction of spacetime and renormalization in the AdS/CFT correspondence," *Commun. Math. Phys.* **217** (2001) 595–622, arXiv:hep-th/0002230.

[156] E. Witten, "Anti-de Sitter space and holography," *Adv. Theor. Math. Phys.* **2** (1998) 253–291, arXiv:hep-th/9802150.

[157] K. B. Fadafan, H. Liu, K. Rajagopal, and U. A. Wiedemann, "Stirring Strongly Coupled Plasma," *Eur. Phys. J.* **C61** (2009) 553–567, arXiv:0809.2869 [hep-ph].

[158] S. S. Gubser, S. S. Pufu, and A. Yarom, "Energy disturbances due to a moving quark from gauge- string duality," *JHEP* **09** (2007) 108, arXiv:0706.0213 [hep-th].

[159] P. M. Chesler and L. G. Yaffe, "The wake of a quark moving through a strongly-coupled $\mathcal{N} = 4$ supersymmetric Yang-Mills plasma," *Phys. Rev. Lett.* **99** (2007) 152001, arXiv:0706.0368 [hep-th].

[160] S. S. Gubser, S. S. Pufu, and A. Yarom, "Sonic booms and diffusion wakes generated by a heavy quark in thermal AdS/CFT," *Phys. Rev. Lett.* **100** (2008) 012301, arXiv:0706.4307 [hep-th].

[161] P. M. Chesler and L. G. Yaffe, "The stress-energy tensor of a quark moving through a strongly-coupled N=4 supersymmetric Yang-Mills plasma: comparing hydrodynamics and AdS/CFT," *Phys. Rev.* **D78** (2008) 045013, arXiv:0712.0050 [hep-th].

[162] P. M. Chesler and A. Vuorinen, "Heavy flavor diffusion in weakly coupled N = 4 super Yang- Mills theory," *JHEP* **11** (2006) 037, arXiv:hep-ph/0607148.

[163] G. W. Gibbons and S. W. Hawking, "Action Integrals and Partition Functions in Quantum Gravity," *Phys. Rev.* **D15** (1977) 2752–2756.

[164] P. K. Kovtun and A. O. Starinets, "Quasinormal modes and holography," *Phys. Rev.* **D72** (2005) 086009, arXiv:hep-th/0506184.

[165] J. J. Friess, S. S. Gubser, G. Michalogiorgakis, and S. S. Pufu, "The stress tensor of a quark moving through N = 4 thermal plasma," *Phys. Rev.* **D75** (2007) 106003, arXiv:hep-th/0607022.

[166] B. Muller and A. Trayanov, "Deterministic chaos in nonAbelian lattice gauge theory," *Phys. Rev. Lett.* **68** (1992) 3387–3390.

[167] T. S. Biro, C. Gong, B. Muller, and A. Trayanov, "Hamiltonian dynamics of Yang-Mills fields on a lattice," *Int. J. Mod. Phys.* **C5** (1994) 113–149, arXiv:nucl-th/9306002.

[168] J. Bolte, B. Muller, and A. Schafer, "Ergodic properties of classical SU(2) lattice gauge theory," *Phys. Rev.* **D61** (2000) 054506, arXiv:hep-lat/9906037.